学位論文

An investigation of single-particle photoluminescence blinking in halide perovskite nanocrystals and quantum dots

(ハライドペロブスカイトナノ結晶と量子ドットにおける単一粒子発光の点滅についての研究)

Division of Environmental Materials Science,
Graduate School of Environmental Science,
Hokkaido University

Lata Chouhan

June 2021

Acknowledgment

I would like to express thanks to God almighty for blessing me with wisdom and strength for completing my doctoral thesis.

I would like to express my gratitude to my supervisor Prof. Vasudevan Pillai Biju. I am very thankful for his continuous motivation and support throughout my Ph.D. journey. This work would not have been at such an optimum version without his help and suggestions. He has guided me in planning the research, operating the instruments, analyzing the data, and constructing the manuscripts. I would also like to express my thanks to Profs. Yuta Takano and Ken-ichi Yuyama for their support during my research. Also, I want to state my sincere gratitude to Ms. Atsuko Fuji for helping me.

I am very thankful to Profs. Hiroshi Miyasaka and Syoji Ito, Graduate School of Engineering, Osaka University for antibunching experiments. I acknowledge the support of Profs. Takayoshi Nakamura and Kiyonori Takahashi, Graduate School of Environmental Science, Hokkaido University for XRD studies. I acknowledge a scholarship from Japan International Cooperation Agency (JICA) for my doctoral research under the Innovative Asia Program. Also, I acknowledge the Hokkaido University Nanotechnology PLATFORM for the STEM and SEM facilities.

I am thankful to all the members of the Laboratory of Molecular Photonics for creating a friendly and cooperative environment. I also express my deepest gratitude to all my family members, grandmother Ganga, father Babulal, mother Kamala, and siblings Deepika and Narendra for their constant encouragement and support. Their faith has helped me a lot in my research. I am also very grateful to my friends who have supported and encouraged me during my research, especially Gajendra, Nisha, Shwetali, Sushant, Elizabeth, Shahjahan, Okamoto, Jahidul, Devika, Bhagyalakshmi, Jeladhara, and Sachith.

Abstract

Lead halide perovskites are promising materials for next-generation optoelectronic devices and photovoltaics. This class of materials has high absorption cross-sections, long photoluminescence lifetimes, high charge carrier mobilities, and high photoluminescence quantum yields. However, there are certain limitations to be lifted for practical applications of these semiconductors. For example, these perovskites are susceptible to moisture, water, oxygen, or light. This thesis collects factors responsible for the degradation of lead halide perovskite nanocrystals and quantum dots and analyzes how to suppress these factors. The main focus is single-particle photoluminescence stability, blinking, and charge carrier dynamics of perovskite nanocrystals and quantum dots. I assign the factors responsible for the deterioration of perovskites to the nonradiative recombinations assisted by halide and cation vacancies. This thesis contains five chapters. In Chapter 1, I introduce the general properties of lead halide perovskites. I explain their chemical structure and various synthesis methods for nanocrystals, quantum dots, thin films, and microcrystals. I describe the band-edge states and the effect of spin-orbit coupling in these perovskites. Next, I introduce their charge carrier dynamics followed by absorption and photoluminescence properties. I review extrinsic and intrinsic factors responsible for degrading the photoluminescence and structure of perovskites. Furthermore, halide perovskites show blinking, which is the stochastic fluctuation of photoluminescence intensity between bright (ON) and dark (OFF) states. I summarize the photoluminescence blinking mechanisms in perovskite nanocrystals and quantum dots. Next, I briefly explain the emerging applications of halide perovskites to lasers, solar cells, and LEDs, followed by my motivation for the research conducted in this thesis. In Chapter 2, I give detailed information about the materials used and the synthesis of lead halide perovskites. I used ligand-mediated transport, ligand-assisted reprecipitation, and hot-injection methods to synthesize these nanocrystals and quantum dots. Also, I describe the working principles of the instruments used in analyzing the structure and optical properties of perovskites, such as absorption spectroscopy, fluorescence spectroscopy, transmission electron microscopy, and X-ray diffraction. Also, I explain the time-resolved fluorescence spectroscopy for analyzing the photoluminescence decay profiles and charge carrier recombination rates of perovskites. Next, I explain the single-particle microspectroscopy system for examining the photoluminescence intensity trajectories of nanocrystals and quantum dots. In Chapter 3, I

sketch the role of oxygen on the stability of methylammonium lead iodide perovskite nanocrystals at the ensemble and the single-particle levels. I show the photoluminescence behavior of the nanocrystals in air, argon, and polymer atmospheres. The photoluminescence intensity in the air continuously decreases, whereas argon or a polymer matrix stabilizes the emission. This photoluminescence behavior is similar at the ensemble and single-particle levels. In halide perovskites, the electron transfer from the perovskite to oxygen generates superoxide at the halide vacancies. Superoxide disintegrates the perovskite structure into lead iodide, methylamine, and water. In an argon or a polymer environment, the photoluminescence intensity is stable, suggesting the suppression of superoxide generation and oxidation of perovskites. Also, the photoluminescence intensity recovery after a long-OFF event shows the stability of the perovskites in the ionized state. Such a long-OFF event associated with a low electron transfer rate suggests that the perovskites do not produce or react with superoxide in the ionized state. In the last section, I explain the degradation mechanism by considering the role of the halide vacancies on superoxide generation. In Chapter 4, I focus on the suppression of the halide vacancies or charge carrier traps in methylammonium lead iodide or bromide perovskite quantum dots at the ensemble and single-particle levels. Halide vacancies are intrinsic defects that create deep traps in the bandgaps of perovskites. These vacancies are the prominent reason for nonradiative recombination or trapping of photogenerated charge carriers. These vacancies are filled by halide salts to reduce their effect on the degradation of the perovskites. At the single-particle level, the photoluminescence intensity trajectories of the vacancy-filled sample show blinking suppression. I assign the relationship between the vacancies and blinking by analyzing over 200 single perovskite quantum dots and construct the ON- and OFF-time probability distributions before and after the vacancy filling. The probability distributions suggest that the blinking behavior changes from type-A to type-B after the filling. That means the charging-discharging processes in the perovskite switch to the trapping-detrapping mechanism. Therefore, the halide salts fill the halide vacancies. Further, the photoluminescence quantum yields and lifetimes of the perovskite quantum dots increase after the halide salt treatment at the ensemble level. Apart from the vacancy filling, the halide-vacancy-assisted nonradiative recombination rate is estimated at 1×10^{8} s^{-1} for lead bromide perovskite and 1.9×10^{9} s^{-1} for lead iodide quantum dots. In Chapter 5, I show the role of A-and B-site cation vacancies on the photoluminescence of caesium lead bromide perovskite quantum dots at the ensemble and single-particle levels. The cation vacancies form shallow trap states in the energy levels of the lead halide perovskite.

Caesium oleate or lead oleate are applied to fill the Cs^+ or Pb^{2+} vacancies. At the ensemble level, the pristine perovskite quantum dot's photoluminescence intensity continuously decreases with time. Although caesium oleate slightly lowers the photodegradation rate of the quantum dots, lead oleate does not affect the photoluminescence. Also, no difference in the average photoluminescence lifetime is observed for the quantum dots before and after the addition of caesium or lead oleate. Similarly, the photoluminescence blinking of single quantum dots does not change before and after adding the caesium or lead oleate. Furthermore, I show the ON- and OFF-time probability distributions by analyzing >200 blinking perovskite quantum dots before and after the addition of caesium oleate. Although the perovskite quantum dots show type-A blinking regardless of the caesium oleate treatment, the overall ON-time increases after the treatment. Therefore, I assume that the caesium oleate treatment reduces the surface Cs^+ vacancies, whereas lead oleate has a negligible effect on the charge carrier dynamics. In summary, this thesis unveils the factors responsible for the degradation and blinking of lead halide perovskite nanocrystals. Further, it demonstrates photoluminescence blinking suppression and intensity enhancement of these nanocrystals by halide vacancy filling.

Abbreviations and Symbols

Å	Angstrom
A	Absorbance
A_0	Constant
A_i	Amplitude of i^{th} time
a, *b*, or *c*	Lattice constant
ASE	Amplified spontaneous emission
AVC	Antisolvent vapor-assisted crystallization
°C	Degree Celsius
c	Concentration
ca	Centered around
cm	Centimeter
cw	Continuous-wave
CB	Conduction band
CBM	Conduction band minimum
CsAc	Caesium acetate
CsOL	Caesium oleate
d_{hkl}	Interplanar spacing
$D_{n,p}$	Diffusion coefficient
DCM	Dichloromethane
DMF	*N*, *N*-dimethylformamide
DMSO	Dimethyl sulfoxide
E	Integrated area of the emission
e	Electronic charge
e^-	Electron
eV	Electronvolt
EMCCD	Electron multiplying charge-coupled device
ETM	Electron transport material
FA	Formamidinium
FABr	Formamidinium bromide
FAI	Formamidinium iodide
FLID	Fluorescence lifetime intensity distribution

fs	Femtosecond
FTO	Fluorine-doped tin oxide
g	Gram
GBL	γ-Butyrolactone
h	Hour
h^+	Hole
HDA	Hexadecyl amine
h, *k*, or *l*	Miller indices
HTM	Hole transport material
Hz	Hertz
ITC	Inverse temperature crystallization
ITO	Indium tin oxide
k_1	The rate constant of monomolecular recombination
k_2	The rate constant of bimolecular recombination
k_3	The rate constant of Auger recombination
k_A	The rate constant of additional nonradiative relaxation
k_B	Boltzmann constant
k_{et}	The rate constant of electron transfer
k_{nr}	The rate constant of nonradiative relaxation
k_r	The rate constant of radiative relaxation
L_D	Diffusion length
LARP	Ligand-assisted reprecipitation
LED	Light-emitting diode
LHP	Lead halide perovskite
LPF	Long-pass filter
m_{eff}	Effective masses
M	Molar
MA	Methylammonium
MABr	Methylammonium hydrobromide
MAI	Methylammonium hydroiodide
mg	Milligram
MHz	Megahertz

min	Minute
mL	Milliliter
mm	Millimeter
mmol	Millimole
ms	Millisecond
mW	Milliwatt
<N>	The average number of photons
N_i	Occurrence of i^{th} time
NA	Numerical aperture
NIR	Near-infrared
NREL	National renewable energy laboratory
nm	Nanometer
ns	Nanosecond
OA	Oleic acid
$P(\tau)$	Probability distribution
PbAc	Lead acetate
$Pb(OL)_2$	Lead oleate
PCE	Power conversion efficiency
PDOS	Projected density of states
PeLED	Perovskite light-emitting diode
PL	Photoluminescence
PMMA	Poly(methyl methacrylate)
PNC	Perovskite nanocrystal
PSC	Perovskite solar cell
PTFE	Polytetrafluoroethylene
PQD	Perovskite quantum dot
QD	Quantum dot
QY	Quantum yield
r_a	The radius of A-site cation
r_b	The radius of B-site cation
r_x	The radius of X-site cation
rpm	Rotation per minute
RT	Room temperature

s	Second
SEM-EDX	Scanning electron microscopy with energy dispersive X-ray spectroscopy
SOC	Spin-orbit coupling
STEM	Scanning transmission electron microscopy
T	Temperature
TiO_2	Titanium dioxide
XRD	X-ray diffraction
UV	Ultraviolet
VB	Valence band
VBM	Valence band maximum
W	Watt
WGM	Whispering Gallery Mode
μJ	Microjoule
μm	Micrometer
$\mu_{n,p}$	Charge carrier mobility
δ_o	Orthorhombic phase
δ_H	Hexagonal phase
σ*	Sigma antibonding orbitals
π*	Pi antibonding orbitals
τ or τ_{avg}	Photoluminescence lifetime or average photoluminescence lifetime
τ_c	Truncation time
ε	Molar extinction coefficient
λ	Wavelength
η	Refractive index

Table of Contents

Chapter 1

Introduction

Abstract

Lead halide perovskites are emerging into potentially low-cost and efficient optoelectronic devices. The interest in this class of materials is increasing due to their unique optical and electronic properties. In this chapter, I introduce the general properties of lead halide perovskite, such as the chemical composition and structure. Subsequently, I explain the various synthesis methods for preparing thin films and microcrystals of lead halide perovskites. Then, I introduce the energy states of the perovskites by discussing the factors affecting the bandgaps, such as the Rashba effect and spin-orbit coupling, which is followed by the charge carrier dynamics by considering monomolecular, bimolecular, and Auger recombination pathways. In the next section, I describe the most intriguing properties of lead halide perovskites, such as the tunable absorption and the photoluminescence from UV-visible to near-infrared region. Further, I summarize the intrinsic and extrinsic factors affecting the photoluminescence and the stability of lead halide perovskites. In the second section, I introduce lead halide perovskite nanocrystal and quantum dot synthesis methods through ligand-assisted reprecipitation or hot-injection, which are known for yielding narrow size distribution of particles. These nanocrystals and quantum dots show intense photoluminescence in the blue-green-red region. However, the photoluminescence intensity stochastically fluctuates among different energy levels, which is called blinking. This blinking is a significant limitation to furthering the application of the perovskites. For example, the blinking decreases the photoluminescence quantum yields and degrades the device efficiencies of lead halide perovskites due to random switching between the radiative and nonradiative recombinations. In the third section, I review the leading and emerging applications of lead halide perovskites. In the last section, I describe my motivation for the research presented in the subsequent chapters to view future uses of the lead halide perovskites.

1.1 General Introduction

Perovskites were first discovered in the early 1800s as calcium titanate oxide ($CaTiO_3$) by Gustav Rose in Russia and later named after the mineralogist Lev Perovski, which has the general formula ABX_3. After a while, Møller *et al.* showed the first crystallographic details of caesium lead halide ($CsPbX_3$, X= Cl, Br, I) perovskites in 1958.[1] However, the interest in this class of materials surged in the early 21st century. Lead halide perovskites (LHPs) gained popularity due to their cost-effective, straightforward synthesis and unique optical and electronic properties. They show high photoluminescence (PL) quantum yield (QY), and PL is tunable in the visible-to-near infrared region (NIR).[2–4] The LHPs also show long charge carrier diffusion lengths, long PL lifetimes, high charge carrier mobilities, and large absorption coefficients, making them suitable to engineer efficient real-world devices, such as solar cells, color-tunable light-emitting diodes (LEDs), and lasers, photodetectors, and single-photon devices.[5–12] The first report on perovskite solar cell (PSC) fabricated using methylammonium lead halide ($MAPbI_3$) perovskite film was published in 2009, which showed the power conversion efficiency (PCE) 3.8%.[13] Over a decade, the maximum PCE had increased up to 26% [National Renewable Energy Laboratory (NREL) efficiency chart] by modifying the charge-injection layers and improving the film quality.[14] LEDs with layered perovskite compounds were demonstrated even before the PSC, but the electroluminescence was observed only at very low temperatures.[15–17] Friend and coworkers fabricated brightly luminescent green and red perovskite LEDs (PeLED) at room temperature with the external quantum efficiencies of 0.1% and 0.76%, respectively.[18] Currently, the highest achieved external quantum efficiencies of blue, green, and red LEDs are 11%, 20.7%, and 21.6%, respectively.[19–21] Soon after the first fabrication of a PSC, the research broadened in defining the electronic states, exciton binding energies, phonons, and spin-orbit coupling in the lead and the lead-free halide perovskites.[22–24]

Halide perovskites have the general formula ABX_3 (X= Cl, Br, I). The insertion of bigger halide ions than oxygen stabilizes the octahedral geometry of perovskites by balancing the size with the B-site metal ions. The A-site cation is in the +1 oxidation state and surrounded by $[BX_6]^{4-}$ octahedrons. The B-site cation is in the +2 or +3 oxidation states and coordinated by six halide ions as shown in Figure 1.1.[25] The most common A-site cations are methylammonium (MA, $CH_3NH_3^+$), formamidinium (FA, $[CH(NH_2)_2]^+$), and caesium (Cs^+).[2–4] The most common B-site cations consist of 3d, 4d, or 5d post-transition

metals, such as lead (Pb^{2+}), tin (Sn^{2+}), germanium (Ge^{2+}), etc. Recently, interest in double perovskites ($A_2BB'X_6$) is increased for replacing the potentially toxic Pb^{2+} by silver (Ag^{+}), indium (In^{3+}), bismuth (Bi^{3+}), and antimony (Sb^{3+}), which form, Cs_2AgBiX_6, Cs_2AgInX_6, and $Cs_2AgBiInX_6$.[26–33]

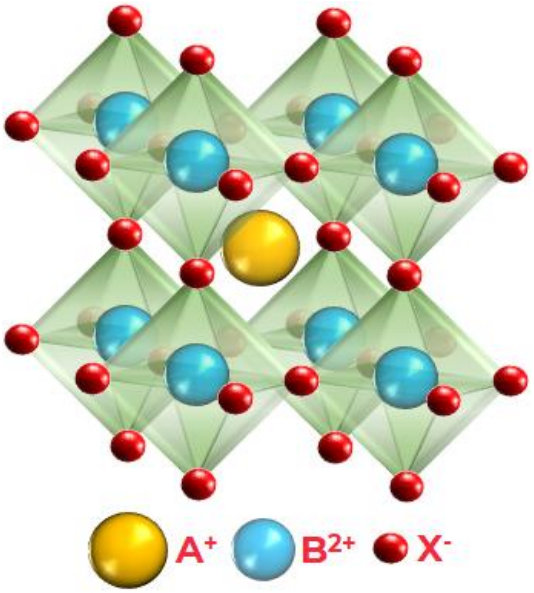

Figure 1.1. A schematic representation of the perovskite structure.

1.1.1 Synthesis of Halide Perovskites

The chemical composition of organic-inorganic halide perovskites can be varied by using different A-, B- and X-site ions. The Goldschmidt tolerance factor (*t*) is appropriate to predict the stability of the structure; *t* is given by

$$t = \frac{r_a + r_x}{\sqrt{2}\,(r_b + r_x)} \tag{1.1}$$

Here, r_a, r_b, and r_x, are the radii of A-site cation, B-site cation, and X-site anion, respectively.[25] The tolerance factor ranges from 0.81 to 1.00, and beyond this range, the perovskite structure is unstable. Another parameter in calculating the stability of the octahedral cavity of perovskite is the octahedral factor, $\mu = r_b/r_x$, which ranges from 0.44 to 0.9.[25] Figure 1.2 shows the common area covered by the tolerance and octahedral factors in determining the stabilities of lead and tin halide perovskites with Cs, MA, or FA cations. The non-spherical geometry of an A-site organic cation and its lattice's constant rotation makes it difficult to determine the exact ionic radius. Therefore, Kieslich *et al.* modified r_a

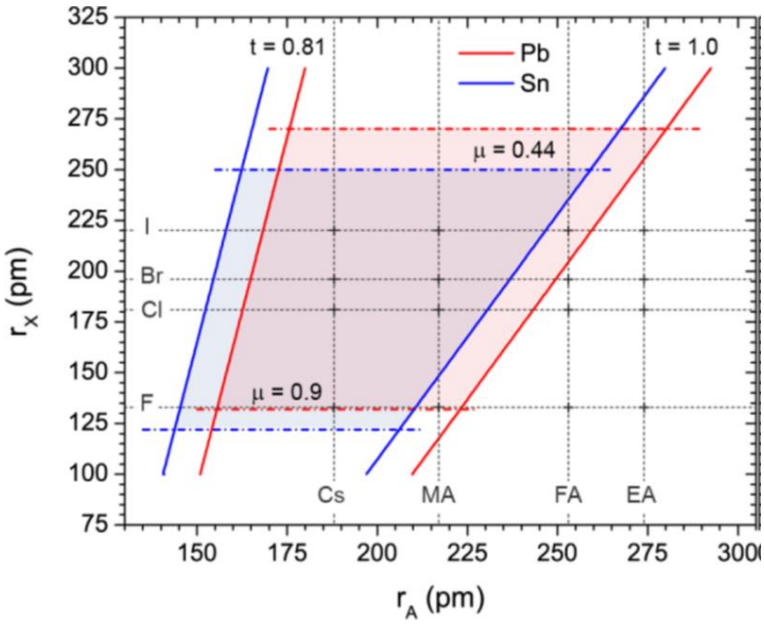

Figure 1.2. Estimation of the stability of LHPs from the radii of A-site cation and the radii of halide. The solid and dash lines represent the tolerance and octahedral factors, respectively. Reproduced from Manser *et al.*[25]

to $r_{Aeff,}$ which is equivalent to the radius of the atom and the distance between the center of masses.[34] For calculating the r_x, the anisotropy was considered in the estimation of the tolerance factor. Another example is that Li *et al.* tuned the tolerance factor by forming a cubic phase of α-$FA_xCs_{1-x}PbI_3$ by alloying two perovskites in the solid-state.[35] One is the orthorhombic phase δ_o-$CsPbI_3$, and the second is the hexagonal phase δ_H-$FAPbI_3$ having <0.8 and >1 tolerance factor, respectively. Based on the tolerance and octahedral factors, the halide perovskites are most stable when the A-site cation is Cs, MA, or FA.

LHP films and microcrystals are synthesized by various processes, as shown in Figure 1.3. LHP films are mostly used as light-harvesting layers in PSCs and are fabricated by a single or sequential (two) step process.[13,27,36–38] In such a fabrication, the precursor salts (CsX or FAX or MAX and PbX_2) are dissolved completely in a polar organic solvent, such as *N*, *N*-dimethylformamide (DMF), dimethyl sulfoxide (DMSO), or γ-butyrolactone (GBL) for crystallization. These solvents have low vapor pressures and high boiling temperatures, making the evaporation, nucleation, and crystal growth slow. Generally, in a one-step process, the precursor salts are mixed in a solvent and spin-coated on a substrate, as shown in Figure 1.3a. The deposition techniques also vary for uniform coating of the LHP films, such as antisolvent-assisted deposition, vacuum- or gas-pumping, and hot-casting.[39] For example, Xiao *et al*. used dichloromethane (DCM) as an antisolvent to

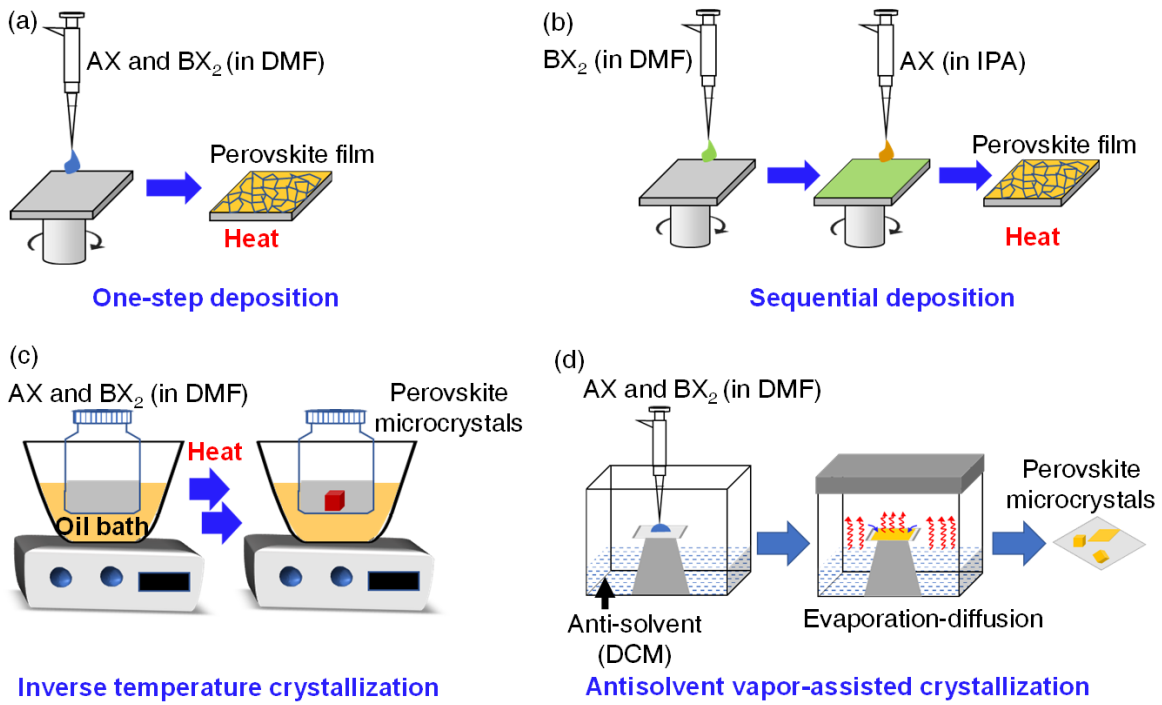

Figure 1.3. Schematic representations of the synthesis of thin films and microcrystals of LHPs. (a) One-step deposition of a precursor solution, (b) sequential deposition of precursors (IPA; isopropanol), (c) inverse temperature crystallization (ITC), and (d) antisolvent vapor-assisted crystallization (AVC).

fabricate uniform $MAPbI_3$ LHP films.[37] Here, $MAPbI_3$ precursors were dissolved in DMF and spin-coated on the TiO_2 substrate. This film was exposed to DCM to induce fast crystallization of the perovskite and form a grain-free film. In sequential deposition (Figure 1.3b), typically, each precursor salt is separately dissolved in a solvent and deposited on a substrate. For example, Im *et al.* dissolved PbI_2 and MAI in DMF separately.[38] Firstly, PbI_2 was spin-coated on a mesoporous TiO_2 substrate, and sequentially, MAI was spin-coated on the PbI_2 layer. A uniform film was obtained after annealing it at 100 °C for 20 s. Apart from spin-coating, other methods such as spray-coating, blade-coating, brush-painting, soft-cover deposition, screen-printing, inkjet-printing, and slot-die coating are used for fabricating uniform LHP films.[39]

For synthesizing LHP microcrystals, some simple methods have been used, such as ITC (Figure 1.3c), AVC (Figure 1.3d), and vapor-melt approaches. For example, Saidaminov *et al.* used ITC for synthesizing single crystals of $MAPbX_3$ and $FAPbX_3$.[40,41] The retrograde solubility of precursor salts is the main parameter to control in the ITC technique. The temperature of the precursor salt solution (FAI and PbI_2) in GBL was

maintained from 80 °C to 120 °C to synthesize $FAPbI_3$ single crystals. In AVC, an antisolvent such as DCM, ethyl acetate, or chlorobenzene slowly diffuses into the precursor solution for the formation of microcrystals.[42] Another technique to synthesize high-quality single microcrystals is the vapor-phase melt approach. This technique uses a quartz tube in a furnace kept at a very high temperature (500 °C to 600 °C). For example, to grow the $CsPbX_3$ crystals, CsX and PbX_2 powders were inserted in a quartz tube, where the temperature of the furnace was slowly increased to 600 °C.[43,44]

1.1.2 Band-Edge Structure

LHPs are direct bandgap semiconductors with strong band-edge optical absorption and tunable PL in visible to NIR region. The intriguing optical properties of perovskites emerge from their unique distribution of energy states at the band edge. Density functional theory calculations have shown that the electronic structures of halide perovskites are governed by the bonding and antibonding atomic orbitals of $[BX_6]^{4-}$ octahedra.[25] The electronic structure of an LHP is shown in Figure 1.4a. In LHPs, the valence band maximum (VBM) is mainly contributed by the halogen *p*- atomic orbital and by the Pb 6*s*-X (3*p*, 4*p*, 5*p*) s*, Pb 6*p*-X (3*s*, 4*s*, 5*s*) s^b (bonding), Pb 6*p*-X (3*p*, 4*p*, 5*p*) p^b (bonding), and Pb 6*s*-X (3*p*, 4*p*,

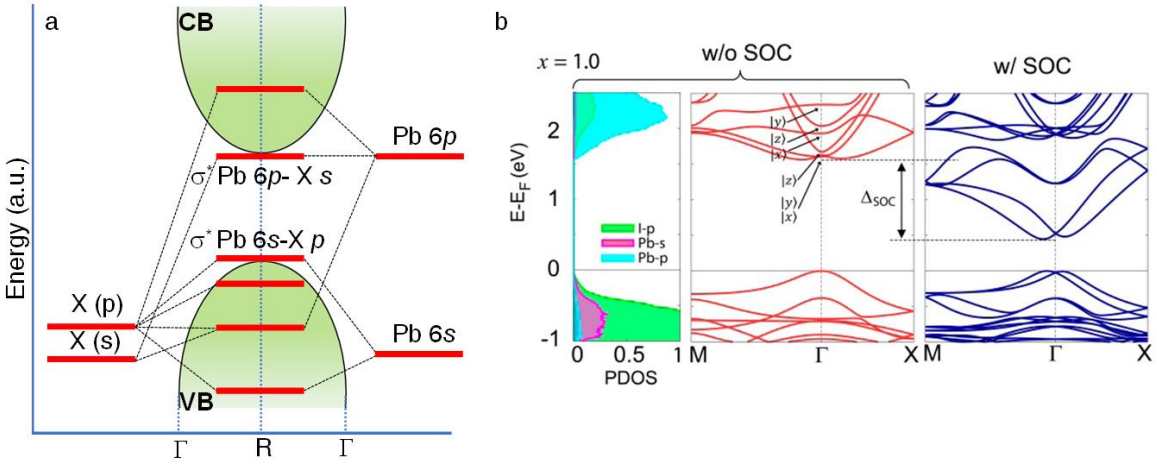

Figure 1.4. (a) Band-edge states of LHPs without considering spin-orbit coupling (SOC). (b) Comparison of electronic band structures of $MAPbI_3$ LHPs (right panel) with and without the SOC and (left panel) the projected density of states. (b) is Reproduced from Im *et al.*[45]

5*p*) s^b orbitals. And, the conduction band minimum (CBM) is constituted by the sigma (σ^*) and pie (π^*) antibonding orbitals. These orbitals in the CBM are formed by the hybridization of the Pb 6*p* and halogen *s*- and *p*- atomic orbitals. The comparison of electronic band structures with and without the SOC and the projected density of states is shown in Figure 1.4b. When the SOC is absent, the VBM is nondegenerate while the CBM is three-fold degenerate. In the presence of SOC, the degeneracy of CBM at the highly symmetric R-point and M-point (of Brillouin zone) splits into the doublet spin-orbit split-off states and the quadruplet states. This splitting increases the dispersion of the conduction band, lowers the bandgap, and affects the optical properties of perovskites by shifting PL spectra to the red. This situation is the opposite in most conventional semiconductors, where the splitting of bands is encountered in the valence band. Therefore, such band structures in perovskites are called the inverted band structure. Also, such splitting in the CBM induces the Rashba effect due to the breaking of the inversion symmetry. Here, the singlet state (highest lying) is optically inactive, whereas the nondegenerate triplet states are optically active.[45,46]

1.1.3 Charge Carrier Dynamics

In LHPs, the charge carrier dynamics play a significant role in their devices, such as solar cells, LEDs, lasers, etc. This class of materials shows a long carrier lifetime, carrier diffusion lengths, and high charge carrier mobility. According to the exciton binding energy, the photogenerated charge carriers in LHPs can freely diffuse or excitonically bind. The mobility for the free charge carriers can be calculated by Einstein's equation

$$\mu_{n,p} = \frac{eD_{n,p}}{k_B T} \tag{1.2}$$

Here, $\mu_{n,p}$ is the charge carrier mobility, e is the electronic charge, $D_{n,p}$ is the diffusion coefficient, k_B is the Boltzmann constant, and T is the temperature. The parameters e, k_B, and T depend on the effective masses (m_{eff}) of the charge carriers. In LHPs, the m_{eff} of electrons and holes are comparable, resulting in balanced diffusion lengths of electrons and holes. This diffusion length (L_D) is related to the charge carrier mobility and the PL lifetime (τ), and it can be calculated as

$$L_D = \sqrt{\frac{k_B T \mu_{n,p} \tau}{e}} = \sqrt{D_{n,p}\tau} \tag{1.3}$$

$MAPbI_3$ single crystals have reported long electron-hole diffusion length (>175 μm) and high charge carrier mobility >100 $cm^2\ V^{-1}\ s^{-1}$.[5] Another point to consider when the thermal energy overcomes the exciton binding energy is the dissociation of free charge carriers. The high charge carrier mobility and long diffusion length also result in a long PL lifetime. The PL lifetime of LHPs varies from sub-nanoseconds- to a few tens of nanoseconds in nanocrystals and up to a few hundred microseconds in films and bulk single crystals. For example, a $MAPbI_{3-x}Cl_3$ LHP film shows carrier lifetime as long as 734 ns,[43] whereas $CsPbX_3$ (X=Cl, Br, I) perovskite nanocrystals (PNC) shows carrier lifetime in the 1-29 ns range.[4] Unlike bulk single crystals and films, the very short carrier lifetime in perovskite nanocrystals is the consequence of an increase in the overlapping of electron and hole wave functions with a decrease in the crystal size. Further, as the LHP crystals' size decreases to the nanoscale regime, the surface trap states are likely to increase due to an increase in the surface-to-volume ratio, which induces additional nonradiative relaxation of charge carriers. Even transient absorption spectroscopic studies at low and high energy excitonic states have confirmed the presence of hot exciton relaxation in $CsPbI_3$ PNCs, including the Auger recombination and intrinsic decay paths.[47] The PL lifetime of LHPs is divided into short-lived and long-lived components determined through their exciton recombination rates.

The rate of recombination of charge carriers in the LHPs can be expressed as

$$-\frac{dn}{dt} = k_1 n + k_2 n^2 + k_3 n^3 \tag{1.4}$$

Here, n is the total carrier concentration, and k_1, k_2, and k_3 are monomolecular (trap-state assisted), bimolecular (free carrier), and Auger recombination rate constants. The trap-assisted recombination (Figure 1.5a) of excitons is a geminate type that depends on the density and distribution of traps. Traps in LHPs are formed from elemental vacancy, interstitials, and antisites. Trap states in LHPs are shallow and low in concentrations. Therefore, a lower rate of monomolecular recombination, which usually dominates in a low charge carrier density, is the characteristic of LHPs. For instance, Wehrenfennig *et al.* reported a low monomolecular recombination rate of $4.9\times10^6\ s^{-1}$ in mixed $MAPbI_{3-x}Cl_x$ and $15\times10^6\ s^{-1}$ in $MAPbI_3$ films.[48] Similarly, many other reports show the trap-assisted recombination rate in the order of $10^6\ s^{-1}$ for lead trihalide and mixed halide perovskites.[49]

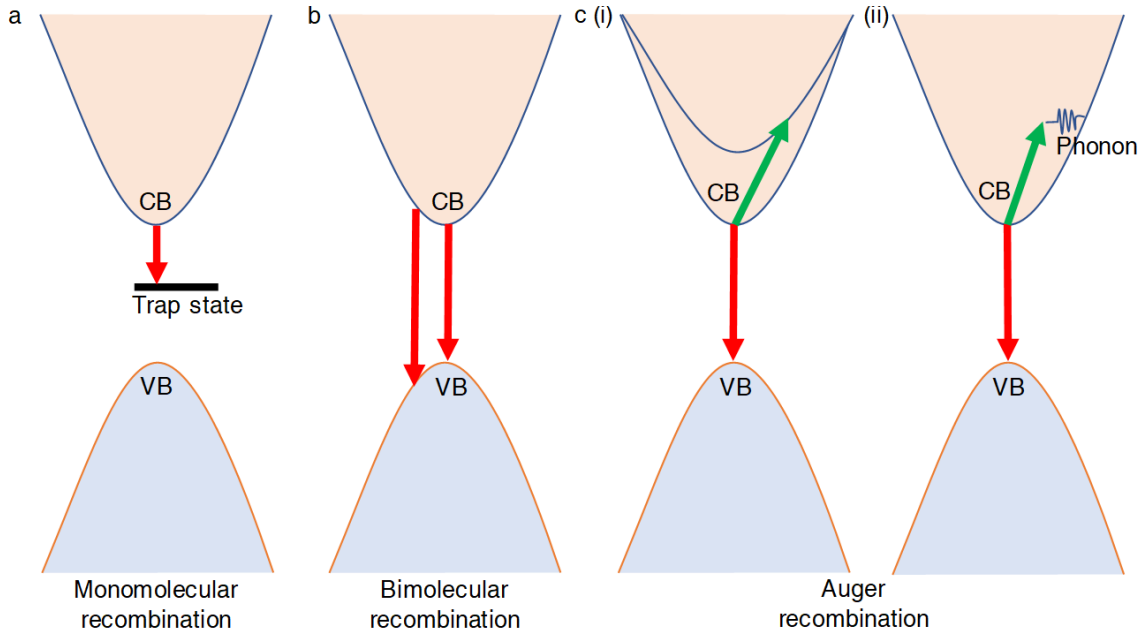

Figure 1.5. A scheme of the charge carrier recombination pathways in LHPs. (a) Monomolecular or trap-assisted recombination, (b) bimolecular recombination, and (c) Auger recombination.

The bimolecular recombination (Figure 1.5b) is non-geminate type recombination, which depends on the composition and band structure of LHPs. In some reports, the bimolecular recombination rate has been explained from the Langevin recombination model's viewpoint when the free charge carriers have low mobility.[48,50] The Langevin recombination takes place when the electrons and holes are inside their joint Coulombic radius. In non-Langevin recombination, the overlapping of the Coulombic radius is less, leading to low charge carrier mobility and a low bimolecular recombination rate. Therefore, the Langevin recombination limit is defined between 1 to 10 $cm^2\ V^{-1}\ s^{-1}$ for charge carrier mobilities, similarly to LHP photovoltaics. In LHPs, the bimolecular recombination varies significantly due to their band structure and chemical composition.

While the monomolecular and bimolecular recombinations dominate at low-charge carrier density, the Auger recombination dominates at higher charge carrier density. Auger recombination occurs when the energy and momentum transfer to third carriers or phonons (Figure 1.5c). The Auger recombination rate constant (k_3) varies from 10^{-27} to ~10^{-28} $cm^6\ s^{-1}$ in pure and mixed halide perovskite films.[49] It shows strong phase specificity, where it decreases in the low-temperature orthorhombic phase, increases in the room temperature tetragonal phase, and decreases in the high-temperature cubic phase. This phase-specific variation of the Auger recombination rate in LHPs is associated with the change in the

electronic band structure due to varying SOC degrees and hydrogen bonding in different crystalline structures.

1.1.4 Absorption and Photoluminescence Properties

The absorption and PL of LHPs are tunable from the visible to the NIR region by varying the halide composition. The PL of the chloride LHPs lies in the blue region, bromide in the green region, and iodide in the red and NIR regions.[3,4,51,52] The absorption and PL spectra of $FAPbX_3$ PNCs in the 415-740 nm range are shown in Figure 1.6.[51] The corresponding images of the colloidal solution of PNCs are shown in Figure 1.6b. With the increase in the concentration of Cl^- content in $FAPbCl_{3-x}Br_x$, the PL blue shifts, and with the increase in the I^- content in $FAPbBr_{3-x}I_x$ PNCs, the PL is redshifted. The linear relationship between the halide composition and the PL peak positions is shown in Figure 1.6c. Since the contribution by the halide *p*-orbitals to the VBM of LHPs is high, the SOC increases and the bandgap decreases from Cl^- to Br^- and from Br^- to I^-. For instance, in the case of $MAPbX_3$ single crystal, the bandgap varies in the order 2.88 eV (cubic $MAPbCl_3$)[53] > 2.21 eV (cubic $MAPbBr_3$)[54] > 1.51 eV (tetragonal $MAPbI_3$).[54]

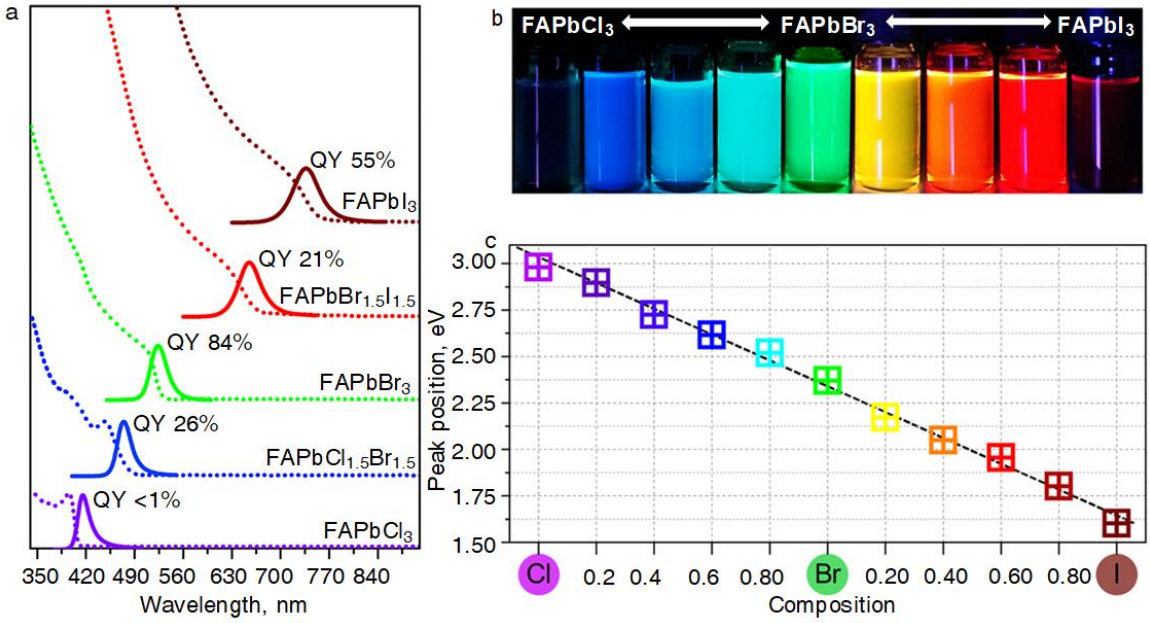

Figure 1.6. Characteristics of $FAPbX_3$ colloidal PNC solutions. (a) Absorption and PL spectra. (b) The corresponding images of the colloidal solutions under photoexcitation. (c) The shift in PL peak with the bromine composition in $FAPbCl_{3-x}Br_x$, and $FAPbBr_{3-x}I_x$ PNCs. Reproduced [(a), (b), and (c)] from Levchuk *et al.*[51]

Furthermore, the bandgap of LHPs is modified by the octahedral tilt, crystal phase, pressure, temperature, and crystal size. The octahedral tilt is noticeable when the Pb-X-Pb dihedral angle increases, which is with an increase in the A-site cation size. For example, the Pb-I-Pb angle increases from 153.2 to 179.9° when Cs^+ is replaced by FA^+.[55] The octahedral tilt is also responsible for the weakening of the SOC because of the less orbital overlapping, thereby increasing the bandgap. Another reason for the octahedral tilt is the change of the crystal structure from tetragonal to orthorhombic and cubic (or other phases). The stable phase for LHPs is the cubic in most cases, where the octahedral tilt is minimized because of the strong SOC.

The temperature during the synthesis and processing also affects the steady-state properties of LHPs. The temperature difference induces different structural phases and affects the exciton-phonon interactions. For instance, the phase of methylammonium lead iodide perovskites at higher temperatures is cubic. At room temperature, it is tetragonal, and at low temperatures, it is orthorhombic.[49] Another temperature effect is exciton-phonon interactions, which are appreciable at a high temperature, broadening the absorption band of LHPs. Similar to temperature, pressure affects the absorption and PL properties of LHPs. Pressure modifies the Pb-X-Pb angle, compresses the Pb-X bond, changes the structural phase, or enhances the octahedral tilt. For instance, by applying certain hydrostatic pressure to $FAPbBr_3$, the structure varies from the cubic to the orthorhombic.[56]

Another factor that controls the absorption and PL properties of LHPs is the crystal size. The absorption and emission maxima blue-shift with decreasing size and vice-versa.[51,57–60] As the size decreases below the exciton Bohr radius, the quantum confinement increases in LHPs, which results in sharp excitonic absorption bands and narrow PL bands. The sizes of an A-site cation and a halogen ion play an important role in determining the Bohr radius. For example, the Bohr radii are *ca* 2, 2.2, 2.5, 3.5, and 6 nm for $MAPbBr_3$, $MAPbI_3$,[61] $CsPbCl_3$, $CsPbBr_3$, and $CsPbI_3$,[4] respectively. Malgras *et al.* deduced the bandgap of $MAPbI_3$ PNC with the crystal size.[59] According to their experimental and theoretical analyses, the bandgap increased from 1.6 to 2.0 eV by decreasing the crystal size from 7 to 3 nm.

1.1.5 Stability

Despite the numerous advantages of LHPs in the optoelectronic field, the stability of this class of materials significantly affects their properties. LHPs are susceptible to light, humidity, oxygen, and temperature.[62–66] However, exposure of LHPs to moisture and light enhances the performance of LHP devices,[67,68] but long-term exposure has detrimental effects.[63,64,69–72] For example, Solanki *et al.* showed a decrease in the rates of monomolecular and bimolecular recombination after treating a $MAPbI_3$ perovskite film with 1% H_2O. In contrast, Aristidou *et al.* showed a decrease in the absorption intensity of $MAPbI_3$ perovskite films when photoirradiated in dry air, which disintegrated the perovskite lattice (Figure 1.7 a-d). As shown in Figure 1.7a-d, the perovskite reacts with oxygen and generates superoxide when photoirradiated. This superoxide deprotonates the methylammonium cation and gradually disintegrates the perovskite into MA, PbI_2, and H_2O. Such a reaction with oxygen and light can impact device performance and photostability of LHPs.[64] Furthermore, Zhang *et al.* described that the reaction with superoxide results in Pb-O formation at the surface of an LHP.[62]

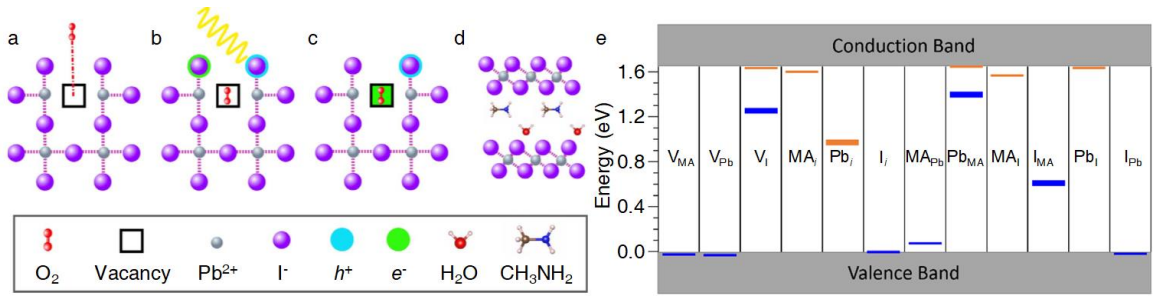

Figure 1.7. (a-d) Deterioration of $MAPbI_3$ perovskite induced by reaction with oxygen and light (a) the diffusion of oxygen into the lattice, (b) photoexcitation of the lattice and the formation of electrons and holes, (c) the generation of superoxide at iodide vacancy, and (d) disintegration of the perovskite. Reproduced (a-d) from Aristidou *et al.*[64] (e) Theoretical charge-state transition levels of intrinsic defects in $MAPbI_3$ perovskite. The blue states represent the transition 0/-, the orange states represent the transition 0/+, and the thick lines represent the deep defects. Reproduced from Agiorgousis *et al.*[73]

Another factor that determines the stability of LHPs is the density and the diffusion of intrinsic defects. The density of defects varies by different synthetic approaches and the local atmosphere. Although LHPs are termed defect-tolerant,[74,75] they have several intrinsic defects, such as cationic and anionic vacancies (V_{MA}, V_{Pb}, V_X), interstitial sites (MA_i, Pb_i,

X_i), and antisites (MA_{Pb}, Pb_{MA}, Pb_X, X_{Pb}, X_{MA}, MA_X).[66,73,76] Among these defects, halide vacancy and interstitials form deep level defects, as shown in Figure 1.7e. Agiorgousis *et al.* showed that in $MAPbI_3$ perovskite, Pb-dimers and I-trimers are formed because of the strong covalency between two Pb^{2+} and 3 I^- ions.[73] Furthermore, they calculated the deep defect transition levels $\varepsilon(0/-)$ and $\varepsilon(0/+)$ for each intrinsic defect; the energies of the defect levels are shown in Figure 1.7e. According to their evaluation, iodine vacancy, Pb_i interstitial, and antisites of Pb_{MA} and I_{MA} form deep defects. Among these defects, the halide vacancies and antisites contribute to nonradiative recombination and trigger fluctuations in the PL intensity. Therefore, the PLQY and device performance of LHPs can be improved by suppressing the transition of deep defects and controlling the relative humidity.

1.1.6 X-ray Diffraction (XRD)

XRD patterns help to identify different phases and dimensionality of perovskites by analyzing the unit cells, space groups, and Miller indices. LHPs have various crystal structures and phases, such as the cubic, orthorhombic, trigonal, monoclinic, pseudocubic, hexagonal, and tetragonal. The phases change with temperature, pressure, chemical composition, and crystal size. As shown in Figure 1.8, the microcrystal of $MAPbBr_3$ shows the diffraction pattern of the cubic phase, whereas the microcrystal of $MAPbI_3$ shows the diffraction pattern of the tetragonal phase.[40] Each diffraction pattern has specific Miller

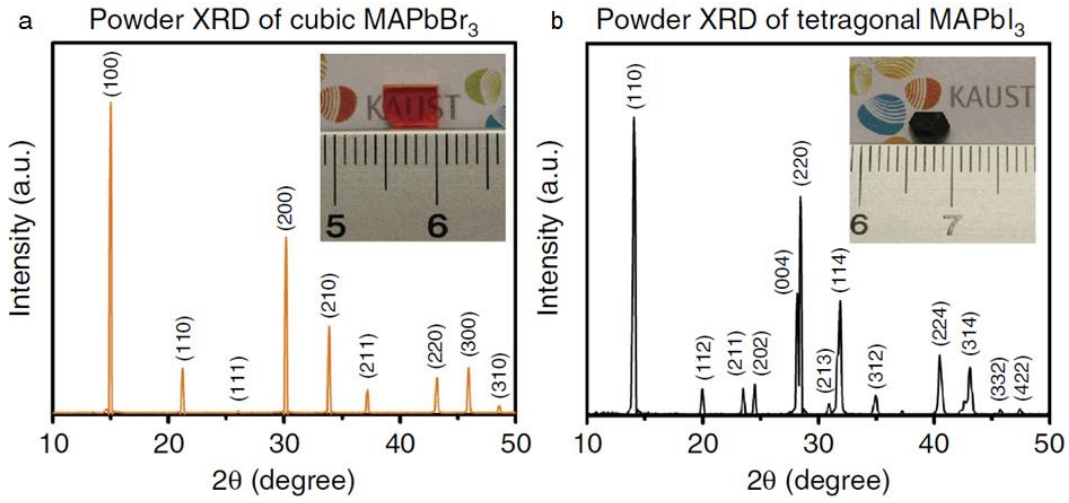

Figure 1.8. The XRD patterns of LHP microcrystals. (a) $MAPbBr_3$, and (b) $MAPbI_3$. Reproduced from Saidaminov *et al.*[40]

indices. The main Miller indices for the cubic phase are (100), (110), (200), and (210), which lie around 15, 22, 30, and 34 (2θ) degrees. The diffraction peaks are similar to the cubic in the orthorhombic phase, but it splits into two around 30°. The major Miller indices for the tetragonal phase are (110), (220), (114), and (224).[40,42] In LHPs, the space group for the cubic phase is *Pm3m*,[4,42] for the tetragonal phase it is *I4/mcm or I4/m*,[42,77] for the pseudocubic phase it is *P4mm*,[77] and for the orthorhombic phase it is *Pnma*.[4]

LHPs are synthesized in various structures, such as single crystal, thin-film, nanocrystal, nanocubes, nanoplatelets, nanowire, quantum dots, quantum cubes, platelets, or sheets. A significant difference between the bulk and nanoparticle structures is that the XRD peaks shift toward smaller angles for nanoparticles. The XRD peaks shift from large angles to small angles when going from chlorine to bromine and from bromine to iodine due to an increased lattice contraction and an increase in the halide ion radius.[4,51]

1.2 Perovskite Nanocrystals and Quantum Dots

1.2.1 Synthesis

PNCs can be synthesized by the hot injection (Figure 1.9a) or ligand-assisted reprecipitation (LARP, Figure 1.9b) method. These methods use long-chain organic ligands composed of carboxylic acids and amines for controlling the growth of PNCs by surface capping (Figure 1.9c). In general, PNCs are prepared from the mixture of precursor solutions of AX and PbX_2, and ligands such as oleic acid, hexadecyl amine, octadecene, and octylamine. PNCs are precipitated out at the end of the reaction and separated by the addition of a poor solvent such as acetone, toluene, or hexane. The first synthesis of $MAPbBr_3$ PNCs was carried out by a simple hot-injection method. In this method, a solution of $PbBr_2$ was injected into the mixture of octyl ammonium bromide or octadecyl ammonium bromide. Furthermore, MABr solutions with different concentrations were added to the above solution, which was along with oleic acid and octadecene, and the reaction mixture was heated at 80 °C. The resulting solution was washed with acetone, and $MAPbBr_3$ PNCs were dispersed in toluene. The size of the PNCs was 6 nm, the shape was cubic with the *Pm-3m* space group, and the emission maxima was *ca* 527 nm.[78] By varying the amount of alkylammonium salt, lead salt, and the temperature, the size, and shape of the PNCs were varied. Similarly, Vybornyi *et al.* synthesized $MAPbI_3$ PNCs by the hot-injection method. Octadecene and PbI_2 were loaded in a round bottom flask and heated at

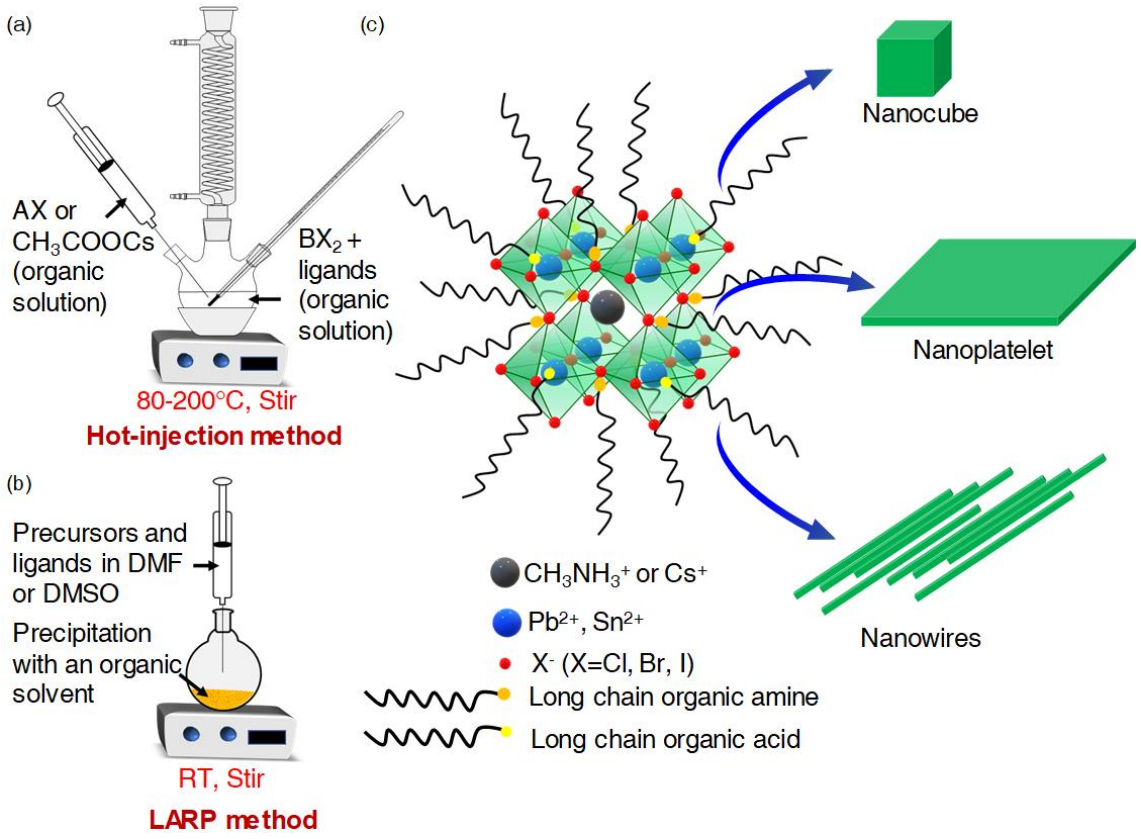

Figure 1.9. A schematic representation of the synthesis of LHP nanocrystals by the (a) hot-injection and (b) LARP methods. (c) Attachment of ligands to the PNCs and different PNCs morphologies synthesized through the above methods.

120 °C. Oleylamine and oleic acid were added to the above reaction mixture under the nitrogen atmosphere and the temperature was decreased to 50-60 °C. In parallel, a methylamine solution was prepared by dissolving methylamine in tetrahydrofuran and oleic acid. The methylamine solution was quickly injected into the reaction mixture and the solution was centrifuged. The residue was dispersed in toluene or hexane. Here, by varying the amount of the ligands, differently shaped $MAPbI_3$ PNCs were formed, such as nanowires, nanocubes, nanoplatelets, and quantum dots. The edge size of $MAPbI_3$ PNCs was ~10 nm, the shape was tetragonal, and the emission maxima was *ca* 750 nm.[79] Also, $CsPbX_3$ PNCs can be prepared by the hot-injection method.[4,80,81] For synthesizing $CsPbX_3$ (X= Br, I) perovskite quantum dots (PQDs), first caesium oleate was prepared by dissolving caesium carbonate and oleic acid in octadecene at 200 °C. After completely dissolving, the solution was kept under vacuum at 130 °C. Parallelly, PbI_2 (or $PbBr_2$) was dissolved in the mixture of oleic acid and oleyl amine in octadecene and at 120 °C. Next, the temperature was raised to 180 °C and caesium oleate was injected into the PbX_2 mixture. The reaction

was arrested quickly after the injection and the reaction mixture was cooled down in an ice bath. The PQDs were collected by centrifugation. The sizes of $CsPbBr_3$, $CsPbBr_{1.5}I_{1.5}$, and $CsPbI_3$ PQDs were 9.3, 10.7, and 11.2 nm, respectively. The emission maxima of $CsPbBr_3$, $CsPbBr_{1.5}I_{1.5}$, and $CsPbI_3$ PQDs were *ca* 510, 585, and 683 nm, respectively.[81]

The LARP method is routinely used to synthesize PNCs at room temperature. For example, $MAPbBr_3$ PNCs were prepared by completely dissolving MABr and $PbBr_2$ in DMF supplemented with a mixture of *n*-octylamine and oleic acid. This precursor solution was added dropwise into toluene under vigorous stirring. The color of the solution changes into yellow-green, indicating the precipitation of PNCs. The precipitate was washed with toluene and centrifuged. The residue was discarded and the PNCs were collected in the supernatant. The size of $MAPbBr_3$ PNCs was 3.3 nm, and the emission maximum was *ca* 515 nm.[3] Similarly, Hassan *et al.* synthesized $MAPbI_3$ PNCs by the LARP method. The precursor mixture was prepared by dissolving the equimolar ratio of MAI and PbI_2 in acetonitrile. This mixture formed a black precipitate, into which methylamine gas was bubbled. It led to the formation of a translucent pale yellow colored solution of the perovskite-MAI complex. In parallel, oleic acid and oleylamine were mixed in anhydrous toluene at room temperature to 60 ℃. The precursor solution was rapidly injected into the ligand mixture under vigorous stirring for 30-120 s. The solution was centrifuged and the residue was discarded. The supernatant was filtered through a PTFE filter (200 nm-size). The size of the $MAPbI_3$ PNCs synthesized at 60 ℃ for 30 s was ~10 nm with the tetragonal shape (space group of *I4/mcm*), for which the emission maxima was *ca* 698 nm. Whereas the size of the $MAPbI_3$ PNCs synthesized over a long time varied from 17-20 nm. It showed a redshifted PL (between 698 and 715 nm).[82] Also, Sun *et al.* synthesized $CsPbX_3$ PQDs by the LARP method. $PbBr_2$ was dissolved in a mixture of DMF, hexanoic acid, and octylamine at room temperature in a flask. After this, Cs-oleate dissolved in octadecene was added to the above mixture. 0.05 mL of this precursor-ligand mixture was added to 2 mL toluene to obtain $CsPbBr_3$ PQDs. The average size of the PQD was 4.3 nm and the shape was orthorhombic with a space group of *Pbnm*. The emission maxima of the PQD was *ca* 505 nm.[83]

1.2.2 Photoluminescence Blinking

PL properties and charge carrier dynamics of LHPs have been studied using steady-state and time-resolved spectroscopic techniques. Such studies reveal the ensemble-averaged properties of LHPs. Thus, single-molecule microspectroscopy has been widely applied to obtaining insight into the properties at the single-particle level. The signature of single-molecule microspectroscopy is evident in the field of cadmium- and lead- chalcogenide-based single quantum dots (QDs),[84–88] where it helped revealing the PL intermittency or blinking. PL blinking is the stochastic fluctuation of emission intensity observed at the single-particle level, characterized by a sequence of bright 'ON' and dark 'OFF' events. An example of such a PL blinking of a $CsPbI_3$ PQD is shown in Figure 1.10a. As shown in Figure 1.10, an ON-state is dominated by radiative recombination of photogenerated charge carriers, whereas an OFF-state is dominated by nonradiative recombination. The characterization of such single QDs can be carried out by examining their photon antibunching behavior and the second-order correlation function $\{g^2(0)\}$ at zero-time. For example, as shown in Figure 1.11a, a QD with single-photon emission shows near-zero $\{g^2(0)\}$ value at zero-time.

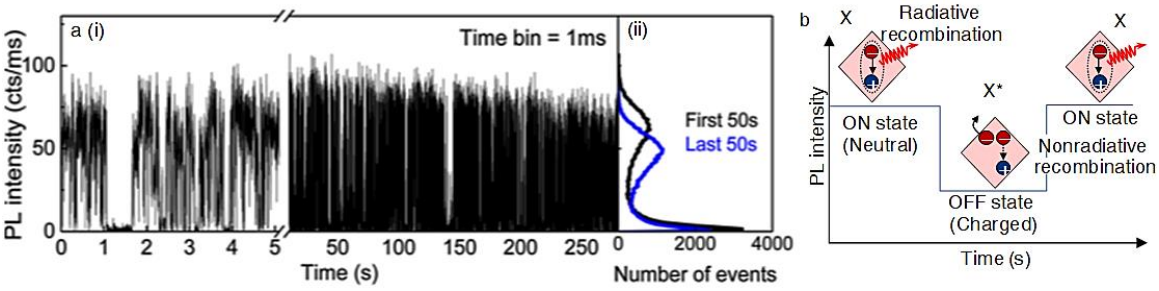

Figure 1.10. (a) Single $CsPbI_3$ PQD. (i) PL blinking and (ii) the corresponding occurrences. Reproduced from Park *et al.*[81] (b) A model of two-state blinking induced by photogenerated charge carriers.

In a PQD, the band-edge states are nondegenerate, which is explained in section 1.1.2. The nondegeneracy is due to the splitting of states and the Rashba effect. To conserve the total exciton momentum, the momentum of electrons and holes combine during the exchange interactions of excitons. In a PQD, this process leads to the breaking of the inversion symmetry of the crystals, making the highest lying singlet state optically inactive. In contrast, the nondegenerate triplet states are optically active and show multiphoton emissions, enhancing the $\{g^2(0)\}$. The threefold band-edge triplet state (Ψ_x, Ψ_y, and Ψ_z)

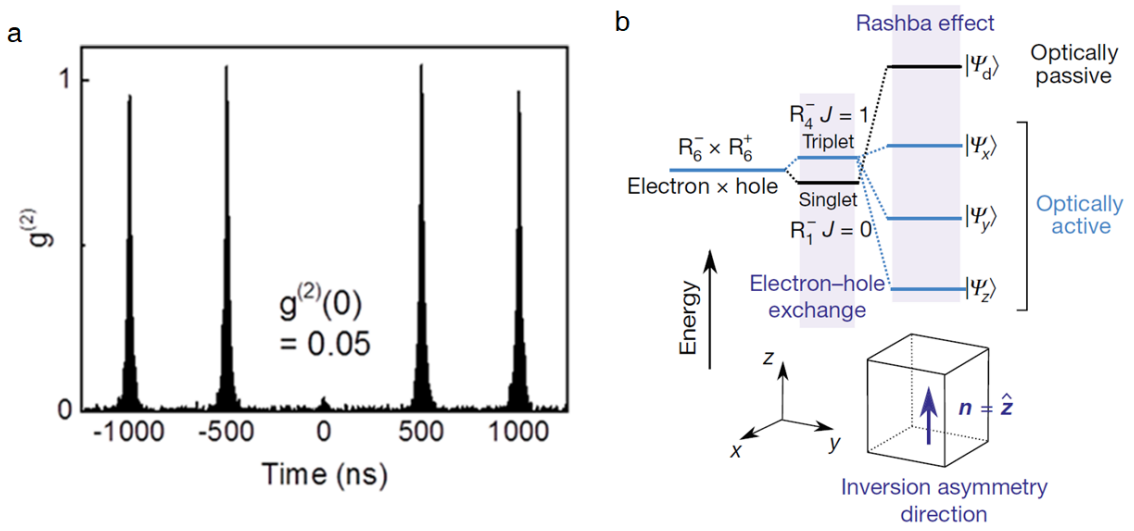

Figure 1.11. (a) Photon antibunching from the second-order correlation function of $CsPbI_3$ PQD. Reproduced from Park *et al.*[81] (b) Schematic representation of electronic states of LHP with SOC and Rashba effect. Reproduced from Becker *et al.*[46]

increases the $\{g^2(0)\}$. The entangled photons from these states should be separated to maintain a very low $\{g^2(0)\}$ or coherent single-photon emission. This separation is achieved by temporally filtering the entangled photons and spectrally selecting the exciton zero-phonon line using the interferometric method.[89] Temperature also plays a role in determining the degeneracy of the band-edge states. With an increase in temperature, the degeneracy of states increases. For example, at low temperatures (~3 K), the photons of single PQDs show strong antibunching, suggesting emission from single-state.[46,89] Similarly, an increase in the excitation light intensity increases the $\{g^2(0)\}$ value due to the formation of bright biexcitons or multiexcitons.

The Mechanism of PL Blinking in Nanocrystals

The nature of PL blinking in LHPs differs with respect to the chemical composition, shape, size, excitation intensity, density, and type of defects.[71,81,90–92] For example, multi-state blinking with large amplitudes has been observed in the first report of PL blinking in $MAPbI_3$ PNCs and microcrystals.[90] In chalcogenide QDs, the blinking enhances with an increase in the excitation intensity, whereas, unlike QDs, the blinking in LHPs enhances at lower excitation intensities. To identify such a PL behavior, a super-resolution microscopy technique was used. It revealed that multi-state blinking occurs due to the difference in

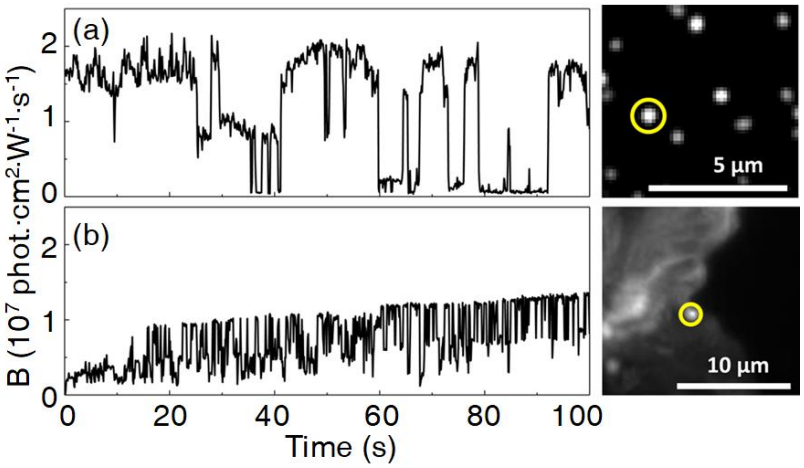

Figure 1.12. Types of PL blinking of (a) $MAPbI_3$ PNC and (b) a $MAPbI_3$ film. Reproduced from Tian *et al.*[90]

emission localization positions in the crystal, or quenching sites (Figure 1.12). The quenching sites are analogous to charge traps, or crystal defects. In PNCs, the blinking is explained with two models: the quenching-site and the emitting-site models, which are shown in Figure 1.13. In the quenching-site model, under the ON-state, the whole PNC is emissive, and the emission localization position lies at the center of the crystal. The

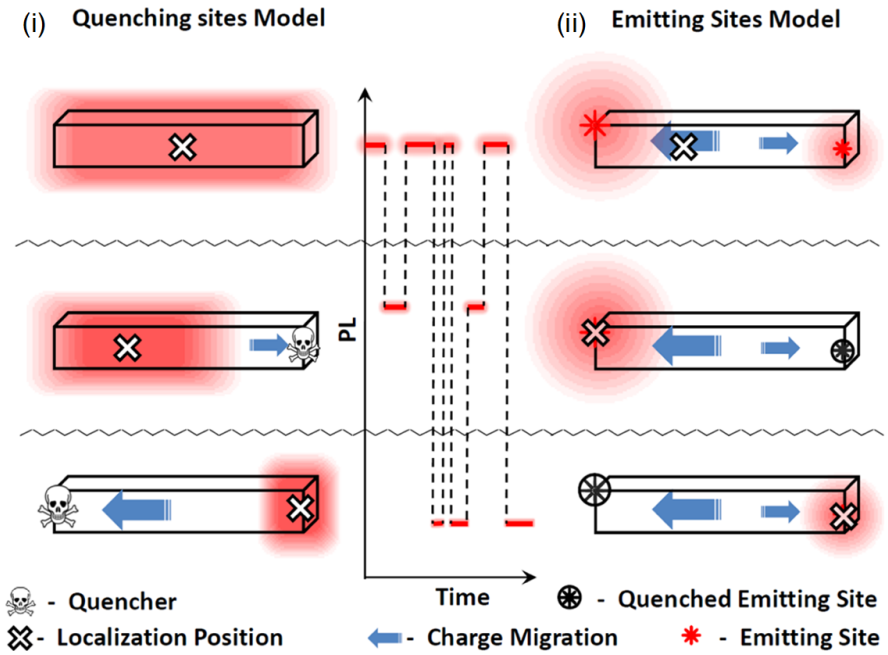

Figure 1.13. A mechanism of the PL blinking in PNCs. (i) The quenching-site model, and (ii) the emitting-site model. Reproduced from Tian *et al.*[90]

emission localization position shifts when the photogenerated quencher is present, resulting in a decrease of PL intensity or switching from the ON- to the OFF-state. These quenchers are charge traps that form at either end of the crystal. On the other hand, in the emitting-site model, several emitting sites form in the crystal at various positions. During the ON-state, the photogenerated charge carriers at various emitting sites diffuse efficiently and recombine radiatively. Here, traps and defects quench one or more emitting sites and decrease the PL intensity, resulting in either an intermediate-state or the OFF-states. In PNCs, the amplitude of blinking decreases with an increase in the PL intensity, which can be attributed to the filling of traps and defects. Under a high excitation intensity, the concentration of charge carriers increases, and the PL intensity averages over the emitting sites.

The characteristics of PL blinking in PNCs were also examined by temperature-dependent studies. Gerhard *et al.* showed that the PL blinking could be suppressed, and the overall PL intensity could be increased by cooling.[92] This behavior is similar in different $MAPbI_3$ PNCs during the cooling-heating cycles. When the emitting-site quenchers overcome the thermal barrier, the emitting-site switches between an active and a passive states. This thermal barrier of the activation of quenchers matches with the energy barrier for halide ion migration in LHPs. So, the PL blinking also results from the diffusion of ions in a PNC, which is responsible for switching nonradiative centers between passive and active states.

The Mechanism of PL Blinking in Quantum Dots

The mechanism of PL blinking in PQDs is assigned to type-A and type-B. Type-A blinking occurs due to the random charging and discharging of charge carriers and the generation of trions. Type-B blinking occurs due to the trapping and de-trapping of photogenerated charge carriers. These mechanisms are rooted in the random switching among the nonradiative Auger recombination, neutralization of charges, and radiative recombination. These models are precisely considered in several blinking studies of single QDs. These mechanisms can be confirmed by correlating the PL lifetime with the PL intensity of a PQD through the fluorescence lifetime intensity distribution (FLID) technique and the ON-and OFF-times probability distribution. In type-A blinking, the PL intensity exponentially decreases with the decrease in PL lifetime [Figure 1.14a(i)], and the ON- and OFF-time

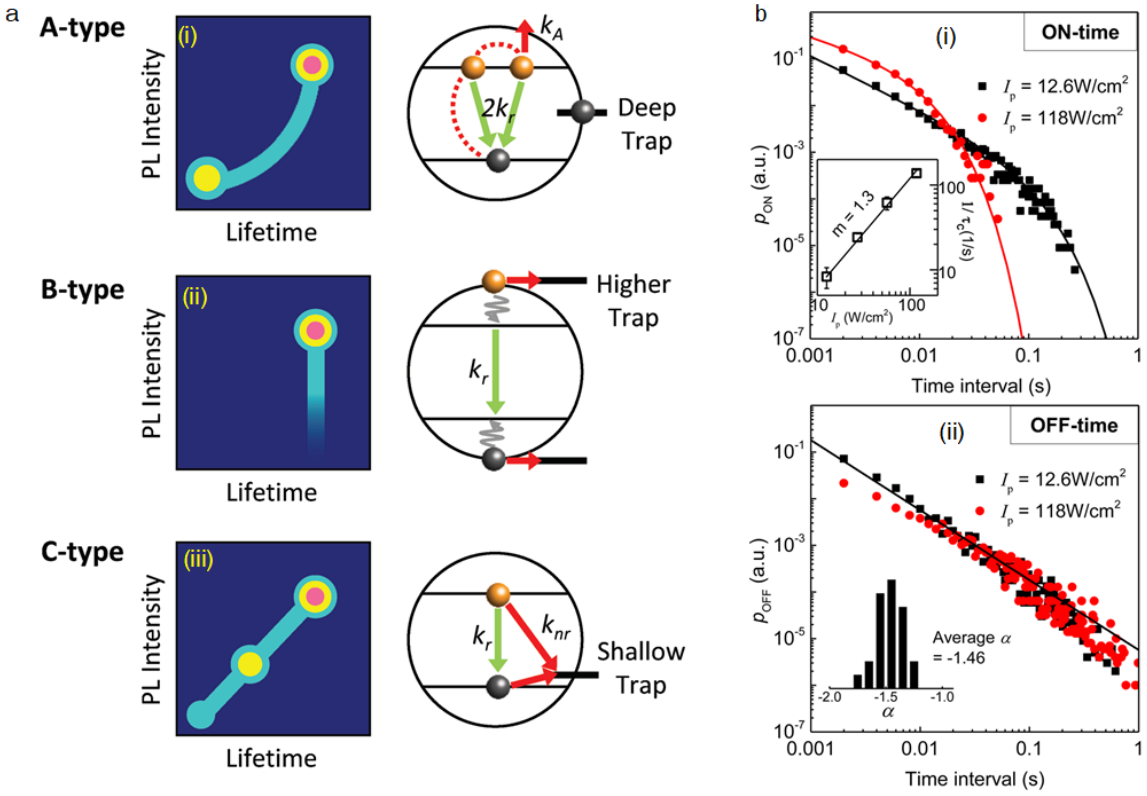

Figure 1.14. (a) Schemes of PL blinking mechanisms in PQDs along with their FLID characteristics and charge carrier recombination pathways: (i) type-A, (b) type-B, and (c) type-C. Reproduced from Kim *et al.*[94] (b) Power-law fittings for $CsPbI_3$ PQDs through (i) the truncated power-law, and (ii) the linear power-law. Reproduced from Park *et al.*[81]

probability distributions follow the truncated power-law behavior (eq. 1.5). In type-B blinking, there is no correlation between the PL intensity and the PL lifetime [Figure 1.14a(ii)], and the ON- and OFF-time probability distributions follow the linear power-law behavior (eq. 1.6).

$$P(\tau) = A_0 \tau^{-\alpha} e^{-\frac{\tau}{\tau_c}} \tag{1.5}$$

$$P(\tau) = A_0 \tau^{-\alpha} \tag{1.6}$$

Here, A_0 is a constant, α is the power-law coefficient, τ_c is the truncation time, and the probability distribution [$P(\tau)$] is calculated using eq. 1.7.

$$P(\tau) = \frac{2N_i}{(\tau_{i+1} + \tau_i) - (\tau_i + \tau_{i-1})} \tag{1.7}$$

Here, N_i is the occurrence of i^{th} time, and τ refers to the time. PQDs tend to show both the mechanisms tandemly.[71,93] For example, the power-law fitting for $CsPbI_3$ PQD shown in

Figure 1.14b, follows the truncated power-law behavior for the ON-time probability distribution, whereas the OFF-time probability distribution follows the linear power-law behavior, suggesting both the mechanisms.[81] Also, Trinh *et al.* verified that during the ON- and OFF-time, $FAPbBr_3$ PQDs show both the type-A and type-B behavior by analyzing the PL intensity trajectories. Here, initially, for 50 ms, the PQDs showed a truncated power-law behavior, and after 50 ms, the PQDs showed the linear power-law behavior. The type-B mechanism has recently been subcategorized into type-B-BC and type-B-HC, which correspond to the trapping-detrapping of the band-edge charge carriers, and hot charge carriers, respectively (Figure 1.14a).[94,95]

In PQDs, the generation of the trion, biexciton, or multiexciton states is expected when photoexcited with a high-intensity light source, which induces PL blinking and modifies the PL quantum yield. Generally, two mechanisms can create biexcitons in a QD. The first is when two photons are simultaneously absorbed with equal or higher energy than the bandgap energy. The second is when the photon energy becomes equal to or greater than the bandgap energy. Therefore, the relaxation of biexcitons occurs through two steps, it emits from a higher excitonic state to the singlet excitonic state and then from the singlet excitonic state to the ground state. On the contrary, under a low excitation intensity, only single excitons emit, which show low $\{g^2(0)\}$ or strong photon antibunching.

The activation and deactivation of multiple recombination centers (MRC) are also responsible for nonradiative recombination in a PQD. When the number of activated MRCs increases, the rate of nonradiative recombination increases, decreasing the PL intensity and lifetime of a PQD. The MRCs cause blinking at multiple intensity levels. Li *et al.* showed the PL behavior of a PQD at different excitation intensities for $\langle N \rangle$ = 0.02, 0.2, and 2.[96] They correlated the PL blinking behavior with the PL lifetime values. At high intensities, $\langle N \rangle$ = 0.2, frequent blinking with more OFF-states were observed as compared to a low intensity, $\langle N \rangle$ =2. The PQD showed multiple state blinking or flickering at $\langle N \rangle$ = 2. At high intensities, the PL blinking of a PQD was caused by both type-A and type-B mechanisms and the activation and deactivation of MRCs.

The crystal size is another crucial factor that affects the nonradiative Auger recombination and PL blinking. Kim *et al.* showed the changes in PL blinking with respect to the PQD size.[94] With the increase in the $MAPbBr_3$ PQD size from ~2 nm to ~10 nm, the fraction of ON-events was increased with a decreased trapping rate and an increased de-

trapping rate. These rates depended on three factors- photoionization of a PQD, the electron and hole trapping-time, and charge tunneling from a PQD to a trap state. During photoionization of a PQD, trions are generated and annihilated by fast Auger nonradiative recombination. The trapping-detrapping time can be analyzed from the ON- and OFF- time probability distributions to explain a difference in the rates of nonradiative recombination. For example, if a hole is trapped in a short-lived state, it increases the rate of nonradiative recombination, which affects the PLQY of the PQD.

PL Blinking Suppression

As stated above, the PL blinking of LHPs varies with the chemical composition, such as the difference in the A, B, or X-site ions, and defect density. For example, Yoshimura *et al.* showed an increase in the ON-time after halide exchange of $CsPbBr_3$ to $CsPbI_3$ PQD.[97] Apart from the halide exchange, filling the halide vacancies can also increase the ON-time. Similarly, blinking suppression in PQDs is achieved by the passivation of surface defects.[98–102] Tang *et al.* encapsulated $CsPbBr_3$ PQDs with CdS shells, and the PL blinking was suppressed by the passivation of deep electron and hole traps (Figure 1.15).[99] Ahmed *et al.* showed that treatment of PNCs with $NaBF_4^-$ reduces the trap states near band-edge states, and hot-carrier states, contributing to the nonradiative recombination.[100] This increased both the ON-time and the brightness of $CsPbBr_3$ PNCs.

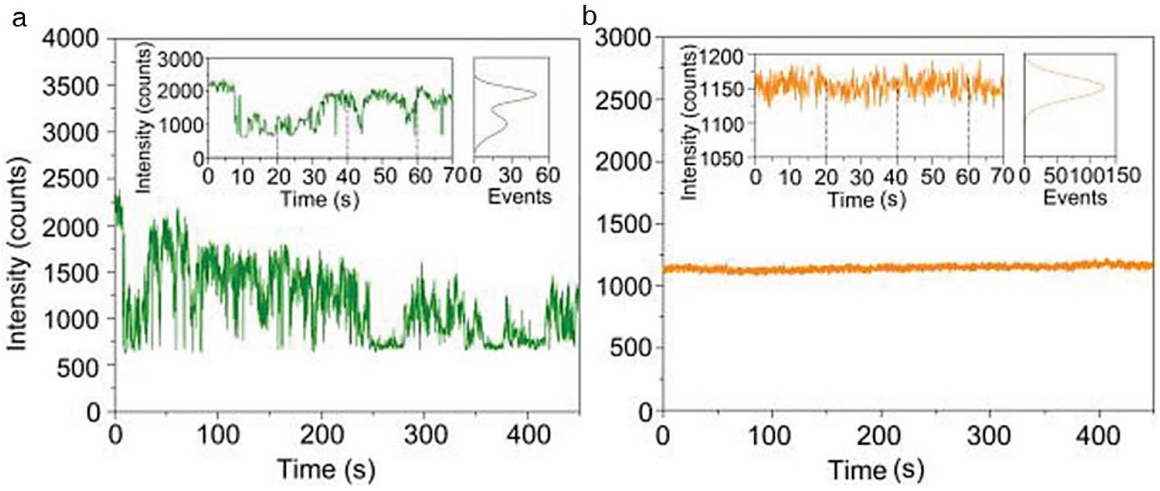

Figure 1.15. PL blinking suppression in $CsPbBr_3$ PQDs (a) before and (b) after encapsulation in a CdS shell. Reproduced from Tang *et al.*[99]

The PL blinking studies of PQDs with various chemical compositions have been carried out by systematic single-particle microspectroscopic experiments. Although surface passivation and halide exchange are consistent with the theories of PL blinking mechanisms, the roles of A-site and B-site cations on blinking are yet to be understood. Nonetheless, the A-site doesn't contribute to the band-edge states, but the size and the dipole moment of an A-site cation affect the bandgaps. The most common A-site inorganic cation, Cs^+, is unipolar, whereas the A-site organic cations, $MA^{+,}$ and FA^+ are dipolar. Among them, MA^+ has a higher dipole moment and is more susceptible to external charges and local current fluctuations. Within a lattice, the rapid motion of MA^+ causes a polaronic screening of charge carriers, which results in the suppression of exciton-exciton interactions in MA-based LHPs. Despite the above clarification of the PL blinking mechanism and efforts to suppress blinking, nonblinking perovskite is an open challenge. It is necessary to suppress blinking and develop nonblinking PQDs and PNCs.

1.3 Applications

Owing to the intriguing properties such as high PLQY, large absorption cross-section, long PL lifetime, and long-range diffusion of carriers, LHPs find their way into potential applications such as lasers, solar cells, and LEDs. After the first demonstration of ultralow threshold (12 $\mu J\ cm^{-2}$) amplified spontaneous emission (ASE) from solution-processed polycrystalline $MAPbX_3$ thin films,[103] studies have been carried out in different perovskite films,[104] and micro-/nanostructures[105] to explore their potentials for optical gain media. In LHPs, when the excitation intensity increases, the broad spontaneous emission redshifts with the appearance of higher energy ASE. Furthermore, LHPs show single and multimode lasing having ultra-narrow emission band and high-quality factor tunable in the entire visible to the NIR region (Figure 1.16a). ASE or lasing in all-inorganic, organic-inorganic, and mixed-halide LHPs has been demonstrated by arranging different types of cavities such as the vertical microcavity, spherical Whispering Gallery Mode (WGM) cavity, planer WGM cavity, random lasing cavity, or Fabry-Pérot cavity.

Apart from ASE and lasing, perovskites are promising for PCE. LHPs have low defect density and ambipolar carrier migration, which enable efficient injection and transport of charges across interfaces. Miyasaka and coworkers verified the PCE of a

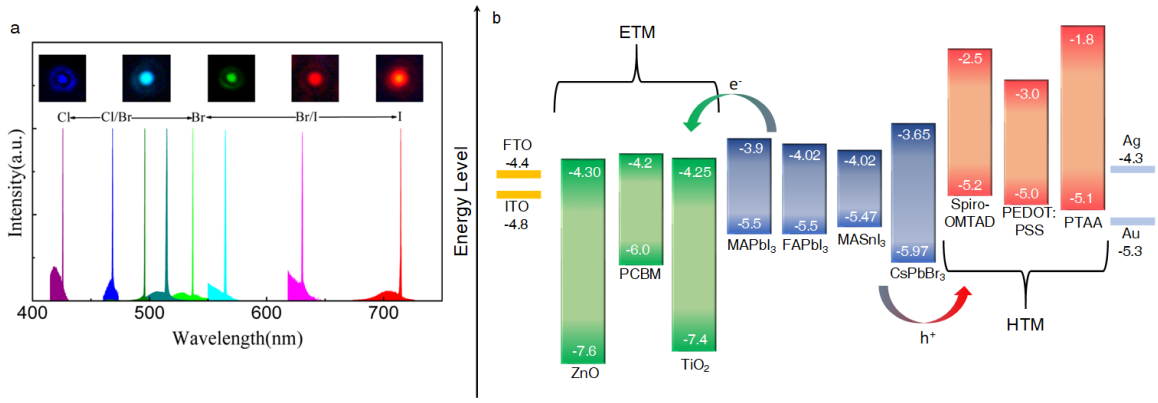

Figure 1.16. (a) Single-mode lasing in $CsPbX_3$ microspheres and the corresponding photographs of the laser spots. Reproduced from Tang *et al.*[12] (b) The energy levels of several electron transport material (ETM) and hole transport material (HTM) layers for fabricating PSC and PeLEDs.

$MAPbI_3$ PSC at 3.8%.[13] In 2018, Seo and coworkers reported the 23.3 % PCE by the fabrication of a solar cell with an HTM.[36] According to the recent NREL chart of solar cell efficiency, PSCs show >26% PCE.[14] For making efficient PSCs, high-quality perovskite layers are essential. Various techniques of device fabrication to form uniform and grain boundary-free perovskite layers have been established. The fabrication of thin layers of perovskites in a PSC the single- and two-step deposition techniques is explained in section 1.1.1. Furthermore, by optimizing ETMs and HTMs, PSCs are at the forefront of next-generation solar cells. Yet another emerging and promising application of perovskites is PeLEDs. By tuning the bandgap by halide exchange and using PNCs with different halides, multicolor PeLEDs were developed. The external quantum efficiencies of PeLEDs have become as high as 20.3% (green PeLED),[20] and 20.1 % (red PeLED).[21]

Typical PSC and PeLED architectures include perovskite as the intrinsic semiconductor sandwiched between an ETM and an HTM. Figure 1.16b shows the energy levels of the conduction and valence bands of several ETMs and HTMs with respect to LHPs. In a PSC, the perovskite layer absorbs the light and generates electrons and holes. The electrons in the perovskite conduction band are transported to the ETM and then to the fluorine-doped tin oxide (FTO) or indium tin oxide (ITO) electrode. On the other hand, holes in the valence band move to the HTM and then to the counter electrode.[106] In a PeLED under an external bias, the electrons and holes from the ETM and HTM layer confine into the perovskite layer. For achieving a high external quantum yield of a green

electroluminescent PeLED, a device was fabricated by using a polymer matrix as an insulator between the perovskite and ETM layers.

Despite the above promising advantages and applications of perovskites, nonradiative carrier/exciton recombination continues to be a significant challenge for the advancement of perovskite technology. For example, PL blinking involving traps and ionization of particles diminishes the PLQY. Thus, single-particle blinking studies are expected to provide a deep understanding of the carrier/exciton relaxation processes and distinguish between different emissive and non-emissive states.

1.4 Motivation

Lead halide perovskites have shown excellent optical and electronic properties and are promising materials for next-generation optical and photovoltaic technologies. Despite their unique properties, LHPs face degradation under photoirradiation and in humid environments due to superoxide generation, which reacts with perovskites and deteriorates their structure and properties. Also, this reduces the PLQY and the PCE. The main view of this thesis is to understand the degradation mechanism of lead halide PNCs and PQDs by analyzing the PL properties at the ensemble and single-particle levels. This thesis will guide the understanding of the PL blinking mechanism and the exciton/carrier recombination pathways in LHPs, which will help in the efficient engineering of perovskite devices.

I used nanocrystals and quantum dots of bromide and iodide perovskites. In **chapter 2**, I give detailed information about the synthesis of $MAPbBr_3$, $MAPbI_3$, and $CsPbBr_3$ PNCs or PQDs. I characterized these LHPs by using absorption and UV-vis fluorescence spectroscopy, transmission electron microscopy, and X-ray diffraction. I examined the PL blinking by using single-particle microspectroscopy and PL decays by using time-resolved PL spectroscopy. The working principles of all the instruments are briefly explained in this chapter.

In **chapter 3**, I examined the PL behavior of $MAPbI_3$ PNCs at different environmental conditions such as in air, argon, or a polymer, which was for determining the LHP degradation mechanism under light and oxygen. $MAPbI_3$ PNCs were found to react with oxygen and generate superoxide. The latter occupies the iodide vacancies in a PNC, deprotonates MA^+, and deteriorates the PNC. I correlated the ensemble-level and

single-particle level PL properties under the above atmospheres of these PNCs. I observed the PL blinking of $MAPbI_3$ PNCs and analyzed the ON and OFF-time probabilities. By examining PL lifetimes, I calculated the rate of electron transfer to oxygen and the rate of nonradiative recombination. PL blinking, PL lifetimes, and the rate of electron transfer helped me understand and suppress the undesired oxidation and degradation of PNCs.

In **chapter 4**, I examined the role of halide vacancies in the blinking and degradation of $MAPbBr_3$ and $MAPbI_3$ PQDs. Halide vacancies play a significant role in degrading LHPs, as they form deep traps in the energy levels of LHPs. I filled the halide vacancies in $MAPbBr_3$ and $MAPbI_3$ PQDs post-synthetically by treating them with MABr and MAI solutions, respectively. Also, I examined the real-time differences in the PL blinking before and after the treatment. I observed PL blinking suppression and PL intensity enhancement by halide vacancy filling. I analyzed the probability distributions of the ON- and OFF-times before and after the vacancy filling and identified that the PL blinking mechanism changes from type-A to type-B after halide vacancies were filled. Then, by evaluating PL decay profiles, I found that the blinking suppression is correlated with the halide vacancy-assisted nonradiative recombination rate.

In **chapter 5**, I examined the role of A- and B-site cations on the stability and blinking of PL in $CsPbBr_3$ PQDs. While the B-site cation (Pb^{2+}) also forms trap-levels in LHPs, which affects the long-term stability of these materials, an A-site cation changes the energy by affecting the octahedral tilt in the perovskite lattice. Thus, the A- and B-site vacancies can also affect the stability and properties of LHPs. I filled the A-site cation vacancies by treating $CsPbBr_3$ PQDs with caesium oleate (CsOL). I observed an increase in the PL intensity after the filling but without changing the blinking behavior. As there isn't any direct contribution of the A-site cation to the VBM or CBM, I assumed that the effect of an A-site cation vacancy on the PL of LHPs is negligibly small. On the other hand, I added lead oleate to $CsPbBr_3$ PQDs, which resulted in a decrease in the PL intensity. This decrease is attributed to an increase in the effective halide ion vacancy by coordinating the excess Pb to the surface halide ions.

Finally, I summarize the results and present my perspectives about the significance of single-particle studies and nonblinking perovskites for applications to quantum optical switches and single-photon light sources.

1.5 References

(1) Møller, C. K. Crystal Structure and Photoconductivity of Cæsium Plumbohalides. *Nature* **1958**, *182* , 1436.

(2) Eperon, G. E.; Stranks, S. D.; Menelaou, C.; Johnston, M. B.; Herz, L. M.; Snaith, H. J. Formamidinium Lead Trihalide: A Broadly Tunable Perovskite for Efficient Planar Heterojunction Solar Cells. *Energy Environ. Sci.* **2014**, *7*, 982–988.

(3) Zhang, F.; Zhong, H.; Chen, C.; Wu, X. G.; Hu, X.; Huang, H.; Han, J.; Zou, B.; Dong, Y. Brightly Luminescent and Color-Tunable Colloidal $CH_3NH_3PbX_3$ (X = Br, I, Cl) Quantum Dots: Potential Alternatives for Display Technology. *ACS Nano* **2015**, *9*, 4533–4542.

(4) Protesescu, L.; Yakunin, S.; Bodnarchuk, M. I.; Krieg, F.; Caputo, R.; Hendon, C. H.; Yang, R. X.; Walsh, A.; Kovalenko, M. V. Nanocrystals of Cesium Lead Halide Perovskites ($CsPbX_3$, X = Cl, Br, and I): Novel Optoelectronic Materials Showing Bright Emission with Wide Color Gamut. *Nano Lett.* **2015**, *15*, 3692–3696.

(5) Dong, Q.; Fang, Y.; Shao, Y.; Mulligan, P.; Qiu, J.; Cao, L.; Huang, J. Electron-Hole Diffusion Lengths >175 μm in Solution-Grown $CH_3NH_3PbI_3$ Single Crystals. *Science* **2015**, *347*, 967–970.

(6) Ning, W.; Wang, F.; Wu, B.; Lu, J.; Yan, Z.; Liu, X.; Tao, Y.; Liu, J.-M.; Huang, W.; Fahlman, M.; Hultman, L.; Sum, T. C.; Gao, F. Long Electron-Hole Diffusion Length in High-Quality Lead-Free Double Perovskite Films. *Adv. Mater.* **2018**, *30*, 1706246.

(7) Cho, H.; Jeong, S.-H.; Park, M.-H.; Kim, Y.-H.; Wolf, C.; Lee, C.-L.; Heo, J. H.; Sadhanala, A.; Myoung, N.; Yoo, S.; Im, S. H.; Friend, R. H.; Lee, T.-W. Overcoming the Electroluminescence Efficiency Limitations of Perovskite Light-Emitting Diodes. *Science* **2015**, *350*, 1222–1225.

(8) Burschka, J.; Pellet, N.; Moon, S. J.; Humphry-Baker, R.; Gao, P.; Nazeeruddin, M. K.; Grätzel, M. Sequential Deposition as a Route to High-Performance Perovskite-Sensitized Solar Cells. *Nature* **2013**, *499*, 316–319.

(9) Daus, A.; Roldán-Carmona, C.; Domanski, K.; Knobelspies, S.; Cantarella, G.; Vogt, C.; Grätzel, M.; Nazeeruddin, M. K.; Tröster, G. Metal-Halide Perovskites for Gate

Dielectrics in Field-Effect Transistors and Photodetectors Enabled by PMMA Lift-Off Process. *Adv. Mater.* **2018**, *30*, 1707412.

(10) Matsushima, T.; Qin, C.; Goushi, K.; Bencheikh, F.; Komino, T.; Leyden, M.; Sandanayaka, A. S. D.; Adachi, C. Enhanced Electroluminescence from Organic Light-Emitting Diodes with an Organic-Inorganic Perovskite Host Layer. *Adv. Mater.* **2018**, *30*, 1802662.

(11) Liu, Z.; Yang, J.; Du, J.; Hu, Z.; Shi, T.; Zhang, Z.; Liu, Y.; Tang, X.; Leng, Y.; Li, R. Robust Subwavelength Single-Mode Perovskite Nanocuboid Laser. *ACS Nano* **2018**, *12*, 5923–5931.

(12) Tang, B.; Dong, H.; Sun, L.; Zheng, W.; Wang, Q.; Sun, F.; Jiang, X.; Pan, A.; Zhang, L. Single-Mode Lasers Based on Cesium Lead Halide Perovskite Submicron Spheres. *ACS Nano* **2017**, *11*, 10681–10688.

(13) Kojima, A.; Teshima, K.; Shirai, Y.; Miyasaka, T. Organometal Halide Perovskites as Visible-Light Sensitizers for Photovoltaic Cells. *J. Am. Chem. Soc.* **2009**, *131*, 6050–6051.

(14) National Renewable Energy Laboratory, Best Research-Cell Efficiency Chart; *www.nrel.gov/pv/cell-efficiency.html.*

(15) Era, M.; Morimoto, S.; Tsutsui, T.; Saito, S. Organic-inorganic Heterostructure Electroluminescent Device Using a Layered Perovskite Semiconductor $(C_6H_5C_2H_4NH_3)_2PbI_4$. *Appl. Phys. Lett.* **1994**, *65*, 676–678.

(16) Hattori, T.; Taira, T.; Era, M.; Tsutsui, T.; Saito, S. Highly Efficient Electroluminescence from a Heterostructure Device Combined with Emissive Layered-Perovskite and an Electron-Transporting Organic Compound. *Chem. Phys. Lett.* **1996**, *254*, 103–108.

(17) Chondroudis, K.; Mitzi, D. B. Electroluminescence from an Organic−Inorganic Perovskite Incorporating a Quaterthiophene Dye within Lead Halide Perovskite Layers. *Chem. Mater.* **1999**, *11*, 3028–3030.

(18) Tan, Z.-K.; Moghaddam, R. S.; Lai, M. L.; Docampo, P.; Higler, R.; Deschler, F.; Price, M.; Sadhanala, A.; Pazos, L. M.; Credgington, D.; Hanusch, F.; Bein, T.; Snaith, H. J.; Friend, R. H. Bright Light-Emitting Diodes Based on Organometal

Halide Perovskite. *Nat. Nanotechnol.* **2014**, *9*, 687–692.

(19) Wang, Q.; Wang, X.; Yang, Z.; Zhou, N.; Deng, Y.; Zhao, J.; Xiao, X.; Rudd, P.; Moran, A.; Yan, Y.; Huang, J. Efficient Sky-Blue Perovskite Light-Emitting Diodes *via* Photoluminescence Enhancement. *Nat. Commun.* **2019**, *10*, 5633.

(20) Lin, K.; Xing, J.; Quan, L. N.; de Arquer, F. P. G.; Gong, X.; Lu, J.; Xie, L.; Zhao, W.; Zhang, D.; Yan, C.; Li, W.; Liu, X.; Lu, Y.; Kirman, J.; Sargent, E. H.; Xiong, Q.; Wei, Z. Perovskite Light-Emitting Diodes with External Quantum Efficiency Exceeding 20 per Cent. *Nature* **2018**, *562*, 245–248.

(21) Xu, W.; Hu, Q.; Bai, S.; Bao, C.; Miao, Y.; Yuan, Z.; Borzda, T.; Barker, A. J.; Tyukalova, E.; Hu, Z.; Kawecki, M.; Wang, H.; Yan, Z.; Liu, X.; Shi, X.; Uvdal, K.; Fahlman, M.; Zhang, W.; Duchamp, M.; Liu, J.-M.; Petrozza, A.; Wang, J.; Liu, L.-M.; Huang, W.; Gao, F. Rational Molecular Passivation for High-Performance Perovskite Light-Emitting Diodes. *Nat. Photonics* **2019**, *13*, 418–424.

(22) Even, J.; Pedesseau, L.; Dupertuis, M.-A.; Jancu, J.-M.; Katan, C. Electronic Model for Self-Assembled Hybrid Organic/Perovskite Semiconductors: Reverse Band Edge Electronic States Ordering and Spin-Orbit Coupling. *Phys. Rev. B* **2012**, *86*, 205301.

(23) Huang, L.; Lambrecht, W. R. L. Electronic Band Structure, Phonons, and Exciton Binding Energies of Halide Perovskites $CsSnCl_3$, $CsSnBr_3$, and $CsSnI_3$. *Phys. Rev. B* **2013**, *88*, 165203.

(24) Even, J.; Pedesseau, L.; Jancu, J. M.; Katan, C. Importance of Spin-Orbit Coupling in Hybrid Organic/Inorganic Perovskites for Photovoltaic Applications. *J. Phys. Chem. Lett.* **2013**, *4*, 2999–3005.

(25) Manser, J. S.; Christians, J. A.; Kamat, P. V. Intriguing Optoelectronic Properties of Metal Halide Perovskites. *Chem. Rev.* **2016**, *116*, 12956–13008.

(26) Jellicoe, T. C.; Richter, J. M.; Glass, H. F. J.; Tabachnyk, M.; Brady, R.; Dutton, S. E.; Rao, A.; Friend, R. H.; Credgington, D.; Greenham, N. C.; Böhm, M. L. Synthesis and Optical Properties of Lead-Free Cesium Tin Halide Perovskite Nanocrystals. *J. Am. Chem. Soc.* **2016**, *138*, 2941–2944.

(27) Noel, N. K.; Stranks, S. D.; Abate, A.; Wehrenfennig, C.; Guarnera, S.; Haghighirad,

A. A.; Sadhanala, A.; Eperon, G. E.; Pathak, S. K.; Johnston, M. B.; Petrozza, A.; Herz, L. M.; Snaith, H. J. Lead-Free Organic-Inorganic Tin Halide Perovskites for Photovoltaic Applications. *Energy Environ. Sci.* **2014**, *7*, 3061–3068.

(28) Saparov, B.; Hong, F.; Sun, J. P.; Duan, H. S.; Meng, W.; Cameron, S.; Hill, I. G.; Yan, Y.; Mitzi, D. B. Thin-Film Preparation and Characterization of $Cs_3Sb_2I_9$: A Lead-Free Layered Perovskite Semiconductor. *Chem. Mater.* **2015**, *27*, 5622–5632.

(29) Wang, A.; Yan, X.; Zhang, M.; Sun, S.; Yang, M.; Shen, W.; Pan, X.; Wang, P.; Deng, Z. Controlled Synthesis of Lead-Free and Stable Perovskite Derivative Cs_2SnI_6 Nanocrystals *via* a Facile Hot-Injection Process. *Chem. Mater.* **2016**, *28*, 8132–8140.

(30) Zhang, J.; Yang, Y.; Deng, H.; Farooq, U.; Yang, X.; Khan, J.; Tang, J.; Song, H. High Quantum Yield Blue Emission from Lead-Free Inorganic Antimony Halide Perovskite Colloidal Quantum Dots. *ACS Nano* **2017**, *11*, 9294–9302.

(31) Xing, G.; Kumar, M. H.; Chong, W. K.; Liu, X.; Cai, Y.; Ding, H.; Asta, M.; Grätzel, M.; Mhaisalkar, S.; Mathews, N.; Sum, T. C. Solution-Processed Tin-Based Perovskite for Near-Infrared Lasing. *Adv. Mater.* **2016**, *28*, 8191–8196.

(32) Volonakis, G.; Haghighirad, A. A.; Milot, R. L.; Sio, W. H.; Filip, M. R.; Wenger, B.; Johnston, M. B.; Herz, L. M.; Snaith, H. J.; Giustino, F. $Cs_2InAgCl_6$: A New Lead-Free Halide Double Perovskite with Direct Band Gap. *J. Phys. Chem. Lett.* **2017**, *8*, 772–778.

(33) McClure, E. T.; Ball, M. R.; Windl, W.; Woodward, P. M. Cs_2AgBiX_6 (X = Br, Cl): New Visible Light Absorbing, Lead-Free Halide Perovskite Semiconductors. *Chem. Mater.* **2016**, *28*, 1348–1354.

(34) Kieslich, G.; Sun, S.; Cheetham, A. K. Solid-State Principles Applied to Organic–Inorganic Perovskites: New Tricks for an Old Dog. *Chem. Sci.* **2014**, *5*, 4712–4715.

(35) Li, Z.; Yang, M.; Park, J. S.; Wei, S. H.; Berry, J. J.; Zhu, K. Stabilizing Perovskite Structures by Tuning Tolerance Factor: Formation of Formamidinium and Cesium Lead Iodide Solid-State Alloys. *Chem. Mater.* **2016**, *28*, 284–292.

(36) Jeon, N. J.; Na, H.; Jung, E. H.; Yang, T. Y.; Lee, Y. G.; Kim, G.; Shin, H. W.; Il Seok, S.; Lee, J.; Seo, J. A Fluorene-Terminated Hole-Transporting Material for

Highly Efficient and Stable Perovskite Solar Cells. *Nat. Energy* **2018**, *3*, 682–689.

(37) Xiao, M.; Huang, F.; Huang, W.; Dkhissi, Y.; Zhu, Y.; Etheridge, J.; Gray-Weale, A.; Bach, U.; Cheng, Y.-B.; Spiccia, L. A Fast Deposition-Crystallization Procedure for Highly Efficient Lead Iodide Perovskite Thin-Film Solar Cells. *Angew. Chem. Int. Ed.* **2014**, *53*, 9898–9903.

(38) Im, J. H.; Jang, I. H.; Pellet, N.; Grätzel, M.; Park, N. G. Growth of $CH_3NH_3PbI_3$ Cuboids with Controlled Size for High-Efficiency Perovskite Solar Cells. *Nat. Nanotechnol.* **2014**, *9*, 927–932.

(39) Dunlap-Shohl, W. A.; Zhou, Y.; Padture, N. P.; Mitzi, D. B. Synthetic Approaches for Halide Perovskite Thin Films. *Chem. Rev.* **2019**, *119*, 3193–3295.

(40) Saidaminov, M. I.; Abdelhady, A. L.; Murali, B.; Alarousu, E.; Burlakov, V. M.; Peng, W.; Dursun, I.; Wang, L.; He, Y.; MacUlan, G.; Goriely, A.; Wu, T.; Mohammed, O. F.; Bakr, O. M. High-Quality Bulk Hybrid Perovskite Single Crystals within Minutes by Inverse Temperature Crystallization. *Nat. Commun.* **2015**, *6*, 7586.

(41) Saidaminov, M. I.; Abdelhady, A. L.; Maculan, G.; Bakr, O. M. Retrograde Solubility of Formamidinium and Methylammonium Lead Halide Perovskites Enabling Rapid Single Crystal Growth. *Chem. Commun.* **2015**, *51*, 17658–17661.

(42) Shi, D.; Adinolfi, V.; Comin, R.; Yuan, M.; Alarousu, E.; Buin, A.; Chen, Y.; Hoogland, S.; Rothenberger, A.; Katsiev, K.; Losovyj, Y.; Zhang, X.; Dowben, P. A.; Mohammed, O. F.; Sargent, E. H.; Bakr, O. M. Low Trap-State Density and Long Carrier Diffusion in Organolead Trihalide Perovskite Single Crystals. *Science* **2015**, *347*, 519–522.

(43) Zhou, H.; Chen, Q.; Li, G.; Luo, S.; Song, T. B.; Duan, H. S.; Hong, Z.; You, J.; Liu, Y.; Yang, Y. Interface Engineering of Highly Efficient Perovskite Solar Cells. *Science* **2014**, *345*, 542–546.

(44) Hu, X.; Zhou, H.; Jiang, Z.; Wang, X.; Yuan, S.; Lan, J.; Fu, Y.; Zhang, X.; Zheng, W.; Wang, X.; Zhu, X.; Liao, L.; Xu, G.; Jin, S.; Pan, A. Direct Vapor Growth of Perovskite $CsPbBr_3$ Nanoplate Electroluminescence Devices. *ACS Nano* **2017**, *11*, 9869–9876.

(45) Im, J.; Stoumpos, C. C.; Jin, H.; Freeman, A. J.; Kanatzidis, M. G. Antagonism between Spin-Orbit Coupling and Steric Effects Causes Anomalous Band Gap Evolution in the Perovskite Photovoltaic Materials $CH_3NH_3Sn_{1-x}Pb_xI_3$. *J. Phys. Chem. Lett.* **2015**, *6*, 3503–3509.

(46) Becker, M. A.; Vaxenburg, R.; Nedelcu, G.; Sercel, P. C.; Shabaev, A.; Mehl, M. J.; Michopoulos, J. G.; Lambrakos, S. G.; Bernstein, N.; Lyons, J. L.; Stöferle, T.; Mahrt, R. F.; Kovalenko, M. V.; Norris, D. J.; Rainò, G.; Efros, A. L. Bright Triplet Excitons in Caesium Lead Halide Perovskites. *Nature* **2018**, *553*, 189–193.

(47) Liu, Q.; Wang, Y.; Sui, N.; Wang, Y.; Chi, X.; Wang, Q.; Chen, Y.; Ji, W.; Zou, L.; Zhang, H. Exciton Relaxation Dynamics in Photo-Excited $CsPbI_3$ Perovskite Nanocrystals. *Sci. Rep.* **2016**, *6*, 29442.

(48) Wehrenfennig, C.; Eperon, G. E.; Johnston, M. B.; Snaith, H. J.; Herz, L. M. High Charge Carrier Mobilities and Lifetimes in Organolead Trihalide Perovskites. *Adv. Mater.* **2014**, *26*, 1584–1589.

(49) Milot, R. L.; Eperon, G. E.; Snaith, H. J.; Johnston, M. B.; Herz, L. M. Temperature-Dependent Charge-Carrier Dynamics in $CH_3NH_3PbI_3$ Perovskite Thin Films. *Adv. Funct. Mater.* **2015**, *25*, 6218–6227.

(50) Herz, L. M. Charge-Carrier Dynamics in Organic-Inorganic Metal Halide Perovskites. *Annu. Rev. Phys. Chem.* **2016**, *67*, 65–89.

(51) Levchuk, I.; Osvet, A.; Tang, X.; Brandl, M.; Perea, J. D.; Hoegl, F.; Matt, G. J.; Hock, R.; Batentschuk, M.; Brabec, C. J. Brightly Luminescent and Color-Tunable Formamidinium Lead Halide Perovskite $FAPbX_3$ (X = Cl, Br, I) Colloidal Nanocrystals. *Nano Lett.* **2017**, *17*, 2765–2770.

(52) Zhou, H.; Yuan, S.; Wang, X.; Xu, T.; Wang, X.; Li, H.; Zheng, W.; Fan, P.; Li, Y.; Sun, L.; Pan, A. Vapor Growth and Tunable Lasing of Band Gap Engineered Cesium Lead Halide Perovskite Micro/Nanorods with Triangular Cross Section. *ACS Nano* **2017**, *11*, 1189–1195.

(53) Maculan, G.; Sheikh, A. D.; Abdelhady, A. L.; Saidaminov, M. I.; Haque, M. A.; Murali, B.; Alarousu, E.; Mohammed, O. F.; Wu, T.; Bakr, O. M. $CH_3NH_3PbCl_3$ Single Crystals: Inverse Temperature Crystallization and Visible-Blind UV-

Photodetector. *J. Phys. Chem. Lett.* **2015**, *6*, 3781–3786.

(54) Pan, J.; Sarmah, S. P.; Murali, B.; Dursun, I.; Peng, W.; Parida, M. R.; Liu, J.; Sinatra, L.; Alyami, N.; Zhao, C.; Alarousu, E.; Ng, T. K.; Ooi, B. S.; Bakr, O. M.; Mohammed, O. F. Air-Stable Surface-Passivated Perovskite Quantum Dots for Ultra-Robust, Single- and Two-Photon-Induced Amplified Spontaneous Emission. *J. Phys. Chem. Lett.* **2015**, *6*, 5027–5033.

(55) Stoumpos, C. C.; Kanatzidis, M. G. The Renaissance of Halide Perovskites and Their Evolution as Emerging Semiconductors. *Acc. Chem. Res.* **2015**, *48*, 2791–2802.

(56) Wang, L.; Wang, K.; Zou, B. Pressure-Induced Structural and Optical Properties of Organometal Halide Perovskite-Based Formamidinium Lead Bromide. *J. Phys. Chem. Lett.* **2016**, *7*, 2556–2562.

(57) Akkerman, Q. A.; Motti, S. G.; Srimath Kandada, A. R.; Mosconi, E.; D'Innocenzo, V.; Bertoni, G.; Marras, S.; Kamino, B. A.; Miranda, L.; De Angelis, F.; Petrozza, A.; Prato, M.; Manna, L. Solution Synthesis Approach to Colloidal Cesium Lead Halide Perovskite Nanoplatelets with Monolayer-Level Thickness Control. *J. Am. Chem. Soc.* **2016**, *138*, 1010–1016.

(58) Dong, Y.; Qiao, T.; Kim, D.; Parobek, D.; Rossi, D.; Son, D. H. Precise Control of Quantum Confinement in Cesium Lead Halide Perovskite Quantum Dots *via* Thermodynamic Equilibrium. *Nano Lett.* **2018**, *18*, 3716–3722.

(59) Malgras, V.; Tominaka, S.; Ryan, J. W.; Henzie, J.; Takei, T.; Ohara, K.; Yamauchi, Y. Observation of Quantum Confinement in Monodisperse Methylammonium Lead Halide Perovskite Nanocrystals Embedded in Mesoporous Silica. *J. Am. Chem. Soc.* **2016**, *138*, 13874–13881.

(60) Zhang, D.; Yu, Y.; Bekenstein, Y.; Wong, A. B.; Alivisatos, A. P.; Yang, P. Ultrathin Colloidal Cesium Lead Halide Perovskite Nanowires. *J. Am. Chem. Soc.* **2016**, *138*, 13155–13158.

(61) Tanaka, K.; Takahashi, T.; Ban, T.; Kondo, T.; Uchida, K.; Miura, N. Comparative Study on the Excitons in Lead-Halide-Based Perovskite-Type Crystals $CH_3NH_3PbBr_3$ $CH_3NH_3PbI_3$. *Solid State Commun.* **2003**, *127*, 619–623.

(62) Zhang, L.; Sit, P. H. L. *Ab Initio* Study of the Role of Oxygen and Excess Electrons in the Degradation of $CH_3NH_3PbI_3$. *J. Mater. Chem. A* **2017**, *5*, 9042–9049.

(63) Aristidou, N.; Sanchez-Molina, I.; Chotchuangchutchaval, T.; Brown, M.; Martinez, L.; Rath, T.; Haque, S. A. The Role of Oxygen in the Degradation of Methylammonium Lead Trihalide Perovskite Photoactive Layers. *Angew. Chem.* **2015**, *127*, 8326–8330.

(64) Aristidou, N.; Eames, C.; Sanchez-Molina, I.; Bu, X.; Kosco, J.; Islam, M. S.; Haque, S. A. Fast Oxygen Diffusion and Iodide Defects Mediate Oxygen-Induced Degradation of Perovskite Solar Cells. *Nat. Commun.* **2017**, *8*, 15218.

(65) Lorenzon, M.; Sortino, L.; Akkerman, Q.; Accornero, S.; Pedrini, J.; Prato, M.; Pinchetti, V.; Meinardi, F.; Manna, L.; Brovelli, S. Role of Nonradiative Defects and Environmental Oxygen on Exciton Recombination Processes in $CsPbBr_3$ Perovskite Nanocrystals. *Nano Lett.* **2017**, *17*, 3844–3853.

(66) Kim, J.; Lee, S. H.; Lee, J. H.; Hong, K. H. The Role of Intrinsic Defects in Methylammonium Lead Iodide Perovskite. *J. Phys. Chem. Lett.* **2014**, *5*, 1312–1317.

(67) Solanki, A.; Lim, S. S.; Mhaisalkar, S.; Sum, T. C. Role of Water in Suppressing Recombination Pathways in $CH_3NH_3PbI_3$ Perovskite Solar Cells. *ACS Appl. Mater. Interfaces* **2019**, *11*, 25474–25482.

(68) Gao, H.; Bao, C.; Li, F.; Yu, T.; Yang, J.; Zhu, W.; Zhou, X.; Fu, G.; Zou, Z. Nucleation and Crystal Growth of Organic–Inorganic Lead Halide Perovskites under Different Relative Humidity. *ACS Appl. Mater. Interfaces* **2015**, *7*, 9110–9117.

(69) Christians, J. A.; Miranda Herrera, P. A.; Kamat, P. V. Transformation of the Excited State and Photovoltaic Efficiency of $CH_3NH_3PbI_3$ Perovskite upon Controlled Exposure to Humidified Air. *J. Am. Chem. Soc.* **2015**, *137*, 1530–1538.

(70) Yang, J.; Siempelkamp, B. D.; Liu, D.; Kelly, T. L. Investigation of $CH_3NH_3PbI_3$ Degradation Rates and Mechanisms in Controlled Humidity Environments Using *in Situ* Techniques. *ACS Nano* **2015**, *9*, 1955–1963.

(71) Yuan, G.; Ritchie, C.; Ritter, M.; Murphy, S.; Gómez, D. E.; Mulvaney, P. The Degradation and Blinking of Single $CsPbI_3$ Perovskite Quantum Dots. *J. Phys. Chem. C* **2018**, *122*, 13407–13415.

(72) Boyd, C. C.; Cheacharoen, R.; Leijtens, T.; McGehee, M. D. Understanding Degradation Mechanisms and Improving Stability of Perovskite Photovoltaics. *Chem. Rev.* **2019**, *119*, 3418–3451.

(73) Agiorgousis, M. L.; Sun, Y.-Y.; Zeng, H.; Zhang, S. Strong Covalency-Induced Recombination Centers in Perovskite Solar Cell Material $CH_3NH_3PbI_3$. *J. Am. Chem. Soc.* **2014**, *136*, 14570–14575.

(74) He, Y.; Matei, L.; Jung, H. J.; McCall, K. M.; Chen, M.; Stoumpos, C. C.; Liu, Z.; Peters, J. A.; Chung, D. Y.; Wessels, B. W.; Wasielewski, M. R.; Dravid, V. P.; Burger, A.; Kanatzidis, M. G. High Spectral Resolution of Gamma-Rays at Room Temperature by Perovskite $CsPbBr_3$ Single Crystals. *Nat. Commun.* **2018**, *9*, 1609.

(75) Huang, H.; Bodnarchuk, M. I.; Kershaw, S. V.; Kovalenko, M. V.; Rogach, A. L. Lead Halide Perovskite Nanocrystals in the Research Spotlight: Stability and Defect Tolerance. *ACS Energy Lett.* **2017**, *2*, 2071–2083.

(76) Buin, A.; Comin, R.; Xu, J.; Ip, A. H.; Sargent, E. H. Halide-Dependent Electronic Structure of Organolead Perovskite Materials. *Chem. Mater.* **2015**, *27*, 4405–4412.

(77) Wang, L.; Williams, N. E.; Malachosky, E. W.; Otto, J. P.; Hayes, D.; Wood, R. E.; Guyot-Sionnest, P.; Engel, G. S. Scalable Ligand-Mediated Transport Synthesis of Organic-Inorganic Hybrid Perovskite Nanocrystals with Resolved Electronic Structure and Ultrafast Dynamics. *ACS Nano* **2017**, *11*, 2689–2696.

(78) Schmidt, L. C.; Pertegás, A.; González-Carrero, S.; Malinkiewicz, O.; Agouram, S.; Mínguez Espallargas, G.; Bolink, H. J.; Galian, R. E.; Pérez-Prieto, J. Nontemplate Synthesis of $CH_3NH_3PbBr_3$ Perovskite Nanoparticles. *J. Am. Chem. Soc.* **2014**, *136*, 850–853.

(79) Vybornyi, O.; Yakunin, S.; Kovalenko, M. V. Polar-Solvent-Free Colloidal Synthesis of Highly Luminescent Alkylammonium Lead Halide Perovskite Nanocrystals. *Nanoscale* **2016**, *8*, 6278–6283.

(80) Ghimire, S.; Chouhan, L.; Takano, Y.; Takahashi, K.; Nakamura, T.; Yuyama, K.; Biju, V. Amplified and Multicolor Emission from Films and Interfacial Layers of Lead Halide Perovskite Nanocrystals. *ACS Energy Lett.* **2019**, *4*, 133–141.

(81) Park, Y. S.; Guo, S.; Makarov, N. S.; Klimov, V. I. Room Temperature Single-

Photon Emission from Individual Perovskite Quantum Dots. *ACS Nano* **2015**, *9*, 10386–10393.

(82) Hassan, Y.; Ashton, O. J.; Park, J. H.; Li, G.; Sakai, N.; Wenger, B.; Haghighirad, A. A.; Noel, N. K.; Song, M. H.; Lee, B. R.; Friend, R. H.; Snaith, H. J. Facile Synthesis of Stable and Highly Luminescent Methylammonium Lead Halide Nanocrystals for Efficient Light Emitting Devices. *J. Am. Chem. Soc.* **2019**, *141*, 1269–1279.

(83) Sun, S.; Yuan, D.; Xu, Y.; Wang, A.; Deng, Z. Ligand-Mediated Synthesis of Shape-Controlled Cesium Lead Halide Perovskite Nanocrystals *via* Reprecipitation Process at Room Temperature. *ACS Nano* **2016**, *10*, 3648–3657.

(84) Galland, C.; Ghosh, Y.; Steinbrück, A.; Sykora, M.; Hollingsworth, J. A.; Klimov, V. I.; Htoon, H. Two Types of Luminescence Blinking Revealed by Spectroelectrochemistry of Single Quantum Dots. *Nature* **2011**, *479*, 203–207.

(85) Ghimire, S.; Biju, V. Relations of Exciton Dynamics in Quantum Dots to Photoluminescence, Lasing, and Energy Harvesting. *J. Photochem. Photobiol. C Photochem. Rev.* **2018**, *34*, 137–151.

(86) Hamada, M.; Nakanishi, S.; Itoh, T.; Ishikawa, M.; Biju, V. Blinking Suppression in CdSe/ZnS Single Quantum Dots by TiO_2 Nanoparticles. *ACS Nano* **2010**, *4*, 4445–4454.

(87) Hohng, S.; Ha, T. Near-Complete Suppression of Quantum Dot Blinking in Ambient Conditions. *J. Am. Chem. Soc.* **2004**, *126*, 1324–1325.

(88) Thomas, E. M.; Ghimire, S.; Kohara, R.; Anil, A. N.; Yuyama, K.; Takano, Y.; Thomas, K. G.; Biju, V. Blinking Suppression in Highly Excited CdSe/ZnS Quantum Dots by Electron Transfer under Large Positive Gibbs (Free) Energy Change. *ACS Nano* **2018**, *12*, 9060–9069.

(89) Utzat, H.; Sun, W.; Kaplan, A. E. K.; Krieg, F.; Ginterseder, M.; Spokoyny, B.; Klein, N. D.; Shulenberger, K. E.; Perkinson, C. F.; Kovalenko, M. V.; Bawendi, M. G. Coherent Single-Photon Emission from Colloidal Lead Halide Perovskite Quantum Dots. *Science* **2019**, *363*, 1068–1072.

(90) Tian, Y.; Merdasa, A.; Peter, M.; Abdellah, M.; Zheng, K.; Ponseca, C. S.; Pullerits,

T.; Yartsev, A.; Sundström, V.; Scheblykin, I. G. Giant Photoluminescence Blinking of Perovskite Nanocrystals Reveals Single-Trap Control of Luminescence. *Nano Lett.* **2015**, *15*, 1603–1608.

(91) Li, C.; Zhong, Y.; Luna, C.; Unger, T.; Deichsel, K.; Gräser, A.; Köhler, J.; Köhler, A.; Hildner, R.; Huettner, S. Emission Enhancement and Intermittency in Polycrystalline Organolead Halide Perovskite Films. *Molecules* **2016**, *21*, 1081.

(92) Gerhard, M.; Louis, B.; Camacho, R.; Merdasa, A.; Li, J.; Kiligaridis, A.; Dobrovolsky, A.; Hofkens, J.; Scheblykin, I. G. Microscopic Insight into Non-Radiative Decay in Perovskite Semiconductors from Temperature-Dependent Luminescence Blinking. *Nat. Commun.* **2019**, *10*, 1698.

(93) Trinh, C. T.; Minh, D. N.; Ahn, K. J.; Kang, Y.; Lee, K. G. Organic-Inorganic $FAPbBr_3$ Perovskite Quantum Dots as a Quantum Light Source: Single-Photon Emission and Blinking Behaviors. *ACS Photonics* **2018**, *5*, 4937–4943.

(94) Kim, T.; Jung, S. Il; Ham, S.; Chung, H.; Kim, D. Elucidation of Photoluminescence Blinking Mechanism and Multiexciton Dynamics in Hybrid Organic-Inorganic Perovskite Quantum Dots. *Small* **2019**, *15*, 1900355.

(95) Trinh, C. T.; Minh, D. N.; Ahn, K. J.; Kang, Y.; Lee, K.-G. Verification of Type-A and Type-B-HC Blinking Mechanisms of Organic–Inorganic Formamidinium Lead Halide Perovskite Quantum Dots by FLID Measurements. *Sci. Rep.* **2020**, *10*, 2172.

(96) Li, B.; Huang, H.; Zhang, G.; Yang, C.; Guo, W.; Chen, R.; Qin, C.; Gao, Y.; Biju, V. P.; Rogach, A. L.; Xiao, L.; Jia, S. Excitons and Biexciton Dynamics in Single $CsPbBr_3$ Perovskite Quantum Dots. *J. Phys. Chem. Lett.* **2018**, *9*, 6934–6940.

(97) Yoshimura, H.; Yamauchi, M.; Masuo, S. *In Situ* Observation of Emission Behavior during Anion-Exchange Reaction of a Cesium Lead Halide Perovskite Nanocrystal at the Single-Nanocrystal Level. *J. Phys. Chem. Lett.* **2020**, *11*, 530–535.

(98) Hu, Z.; Liu, Z.; Bian, Y.; Li, S.; Tang, X.; Du, J.; Zang, Z.; Zhou, M.; Hu, W.; Tian, Y.; Leng, Y. Enhanced Two-Photon-Pumped Emission from *in Situ* Synthesized Nonblinking $CsPbBr_3/SiO_2$ Nanocrystals with Excellent Stability. *Adv. Opt. Mater.* **2018**, *6*, 1700997.

(99) Tang, X.; Yang, J.; Li, S.; Liu, Z.; Hu, Z.; Hao, J.; Du, J.; Leng, Y.; Qin, H.; Lin, X.;

Lin, Y.; Tian, Y.; Zhou, M.; Xiong, Q. Single Halide Perovskite/Semiconductor Core/Shell Quantum Dots with Ultrastability and Nonblinking Properties. *Adv. Sci.* **2019**, *6*, 1900412.

(100) Ahmed, T.; Seth, S.; Samanta, A. Mechanistic Investigation of the Defect Activity Contributing to the Photoluminescence Blinking of $CsPbBr_3$ Perovskite Nanocrystals. *ACS Nano* **2019**, *13*, 13537–13544.

(101) Boote, B. W.; Andaraarachchi, H. P.; Rosales, B. A.; Blome-Fernández, R.; Zhu, F.; Reichert, M. D.; Santra, K.; Li, J.; Petrich, J. W.; Vela, J.; Smith, E. A. Unveiling the Photo- and Thermal-Stability of Cesium Lead Halide Perovskite Nanocrystals. *ChemPhysChem* **2019**, *20*, 2647–2656.

(102) Li, H.; Qian, Y.; Xing, X.; Zhu, J.; Huang, X.; Jing, Q.; Zhang, W.; Zhang, C.; Lu, Z. Enhancing Luminescence and Photostability of $CsPbBr_3$ Nanocrystals *via* Surface Passivation with Silver Complex. *J. Phys. Chem. C* **2018**, *122*, 12994–13000.

(103) Xing, G.; Mathews, N.; Lim, S. S.; Yantara, N.; Liu, X.; Sabba, D.; Grätzel, M.; Mhaisalkar, S.; Sum, T. C. Low-Temperature Solution-Processed Wavelength-Tunable Perovskites for Lasing. *Nat. Mater.* **2014**, *13*, 476–480.

(104) Deschler, F.; Price, M.; Pathak, S.; Klintberg, L. E.; Jarausch, D. D.; Higler, R.; Hüttner, S.; Leijtens, T.; Stranks, S. D.; Snaith, H. J.; Atatüre, M.; Phillips, R. T.; Friend, R. H. High Photoluminescence Efficiency and Optically Pumped Lasing in Solution-Processed Mixed Halide Perovskite Semiconductors. *J. Phys. Chem. Lett.* **2014**, *5*, 1421–1426.

(105) Yakunin, S.; Protesescu, L.; Krieg, F.; Bodnarchuk, M. I.; Nedelcu, G.; Humer, M.; De Luca, G.; Fiebig, M.; Heiss, W.; Kovalenko, M. V. Low-Threshold Amplified Spontaneous Emission and Lasing from Colloidal Nanocrystals of Caesium Lead Halide Perovskites. *Nat. Commun.* **2015**, *6*, 8056.

(106) Jena, A. K.; Kulkarni, A.; Miyasaka, T. Halide Perovskite Photovoltaics: Background, Status, and Future Prospects. *Chem. Rev.* **2019**, *119*, 3036–3103.

Chapter 2

Experiments

Abstract

This chapter introduces the experimental and characterization techniques in the study. Here, I listed the materials and samples used throughout my work. Next, I explained the methods to synthesize lead halide perovskite nanocrystals and quantum dots by the ligand-mediated transport, ligand-assisted reprecipitation, and hot-injection methods. These methods yielded a narrow and uniform size distribution of the perovskite nanocrystals and quantum dots. The X-ray diffraction data helped me understand the structural phases of lead halide perovskites. Also, the sizes of perovskite nanocrystals were calculated from the images collected by transient electron microscopy. I estimated the elemental composition of the halide vacancies in perovskite quantum dots by using the scanning electron microscopy with the energy dispersive X-ray spectroscopy. The band-edge absorption and the emission maxima of these perovskite nanocrystals and quantum dots were determined using UV-vis absorption spectrophotometry and steady-state fluorescence spectroscopy. For analyzing the photoluminescence intensity trajectories of isolated single particles, I used single-particle microspectroscopy equipped with an electron multiplying charge-coupled device. Single-photon coincidence measurement was carried out to confirm the emission from isolated single particles. The time-resolved fluorescence spectroscopy was used to detect the photoluminescence decay profiles. The photoluminescence intensity trajectories and average lifetimes helped understand the recombination pathways of photogenerated charge carriers in perovskite nanocrystals and quantum dots.

2.1. Materials

Chemicals used in synthesizing and preparing the samples for experimental studies: methylammonium hydroiodide [CH_3NH_3I (MAI), >98%, Tokyo Chemicals Industry (TCI)], methylammonium hydrobromide [CH_3NH_3Br (MABr), >98%, TCI], caesium acetate [$C_2H_3CsO_2$ (CsAc), 99.9%, Sigma-Aldrich], lead iodide (PbI_2, >99%, Aldrich), lead bromide ($PbBr_2$, >98%, Aldrich), lead acetate trihydrate [$Pb(CH_3CO_2)_2.3(H_2O)$ (PbAc), ≥99%, Sigma-Aldrich], hexadecyl amine [$C_{16}H_{35}N$, >95%, TCI], oleic acid [$C_{18}H_{34}O_2$ (OA), >85 %, TCI], 1-hexadecene ($C_{16}H_{32}$, Fujifilm Wako), 1-octadecene ($C_{18}H_{36}$, >90%, TCI), dehydrated *N*,*N*-dimethylformamide [C_3H_7NO (DMF), Fujifilm Wako], γ-butyrolactone [$C_4H_6O_2$ (GBL), >99.0%, TCI], dehydrated toluene ($C_6H_5CH_3$, Fujifilm Wako), dehydrated hexane (C_6H_{14}, Fujifilm Wako), *n*-butanol ($C_4H_{10}O$, >99%, Fujifilm Wako), dichloromethane [CH_2Cl_2 (DCM), Fujifilm Wako], poly(methyl methacrylate) [$(C_5O_2H_8)_n$ (PMMA), Aldrich], indium tin oxide glass (ITO) substrates-pixelated anode [6 pixel, thickness 1.1 mm, Ossila], coverglass (24×50 mm^2, and 25×50 mm^2, thickness 0.13-0.17 mm, Matsunami Neo Cover Glass), and micro coverglass (76×26 mm^2, thickness 0.8-1.0 mm, Matsunami Neo Pre-cleaned).

2.2. Methods

2.2.1 Synthesis of Perovskite Nanocrystals and Quantum Dots

Ligand-Mediated Transport Method

Synthesis of $MAPbI_3$ Perovskite Nanocrystals (PNC)

I used the modified ligand-mediated transport method (Figure 2.1) from the literature to synthesize $MAPbI_3$ PNC.[1] In the literature, PbI_2 and MAI were mixed in a mixture of hexane, octylamine, and OA and vigorously stirred for 1 h. This solution was centrifuged at 6000 rpm for 5 min, and the $MAPbI_3$ PNCs were collected in the supernatant.[1] In this study, I modified the reported procedure by using HDA instead of octylamine and changing the purification method. In a glass vial, MAI (0.12 mmol, 19 mg) and PbI_2 (0.15 mmol, 69 mg) were weighed together and dried under vacuum for 15 min. Parallelly, I completely dissolved HDA (0.12 mmol, 29 mg) and OA (0.13 mmol, 40 μL) in hexane (1 mL). The ligand solution was added to the precursor mixture containing MAI and PbI_2. The reaction was carried out under vigorous stirring at room temperature. On the top of the glass vial,

an orangish-red layer was formed, which was decanted, and discarded. At the bottom of the glass vial, a brown precipitate was formed. I added 1.5 mL toluene to this precipitate and the mixture was sonicated for 5 min. The sample was centrifuged for 10 min at 10000 rpm and the residue was discarded. The supernatant was centrifuged again for 45 min at 14000 rpm. The $MAPbI_3$ PNCs were collected in the residue and the supernatant was discarded. The residue, when dissolved in toluene, formed a clear brownish-red solution. Photoluminescence (PL) properties of the $MAPbI_3$ PNCs are discussed in Chapter 3.

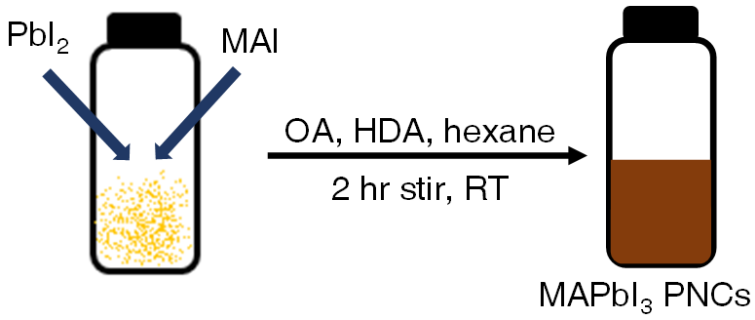

Figure 2.1. A schematic of the synthesis of $MAPbI_3$ PNCs.

Ligand-Assisted Reprecipitation Method

Synthesis of $MAPbI_3$ Perovskite Quantum Dots (PQDs)

The synthesis of $MAPbI_3$ PQD was carried out by the ligand-assisted reprecipitation (LARP) method.[2–4] In the reported method, Dong and co-workers[2] dissolved MAI and PbI_2 in DMF, octylamine, and OA. This precursor solution was added to toluene under vigorous stirring at room temperature. The solution was centrifuged at 7000 rpm for 10 min, and the residue was discarded. The $MAPbI_3$ PQDs were collected in the supernatant. In my studies, I slightly modified the LARP method by using GBL instead of DMF, set the temperature at 80 °C, and changed the purification method. The scheme of $MAPbI_3$ PQD synthesis is shown in Figure 2.2. PbI_2 (0.72 mmol, 346 mg) and MAI (0.72 mmol, 114 mg) were dissolved in 1 mL GBL. In a round bottom flask, I dissolved OA (3.6 mmol, 1.14 mL) and HDA (0.72 mmol, 174 mg) in 25 mL dehydrated toluene under an argon atmosphere with vigorous stirring. When the temperature of the ligand mixture reached 80 °C, the precursor solution was quickly injected. The color of the reaction mixture was changed from yellow to brown, and a precipitate was formed. After 15 min, the reaction mixture was cooled down to room temperature. The residue was suspended in toluene and separated by centrifugation at 7000 rpm for 5 min. The residue was discarded, and the supernatant was

centrifuged again at 12000 rpm for 10 min. The PQDs were collected in the residue, and the supernatant was discarded. The PL properties of this $MAPbI_3$ PQD sample are reported in Chapter 4.

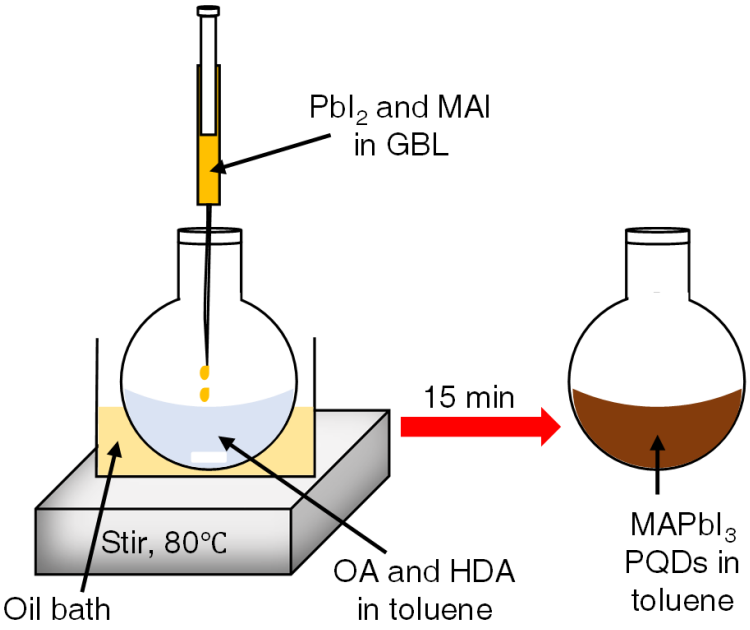

Figure 2.2. A scheme of the synthesis of $MAPbI_3$ PQDs.

Synthesis of $MAPbBr_3$ PQDs

I synthesized $MAPbBr_3$ PQD by following the LARP method.[2,5,6] In the literature method, MABr and $PbBr_2$ were dissolved in a mixture of DMF, octylamine, and OA. This precursor solution was added to toluene under vigorous stirring at room temperature. The solution was centrifuged at 7000 rpm for 10 min, and the residue was discarded. The supernatant was bright yellow, which contained the $MAPbBr_3$ PQDs. In my studies, I slightly modified the LARP method by changing octylamine to HDA and changing the purification method. The scheme of $MAPbBr_3$ PQDs synthesis is shown in Figure 2.3. The precursors $PbBr_2$ (0.27 mmol, 100 mg) and MABr (0.25 mmol, 28 mg), and the ligands OA (0.25 mmol, 80 µL) and HDA (0.19 mmol, 46 mg) were dissolved in DMF (1 mL). This mixture was warmed in a water bath at 60 °C to obtain a clear solution. This precursor-ligand mixed solution was injected into a round bottom flask containing dehydrated toluene (50 mL) and kept on vigorously stirring at room temperature. After 15 min, the stirring was stopped and the reaction mixture was centrifuged at 10000 rpm for 5 min. The supernatant was discarded, and the residue was suspended in toluene and centrifuged at 5000 rpm for 5 min. The $MAPbBr_3$ PQDs were collected in the centrifugate. The PL properties of this $MAPbBr_3$ PQD sample are reported in Chapter 4.

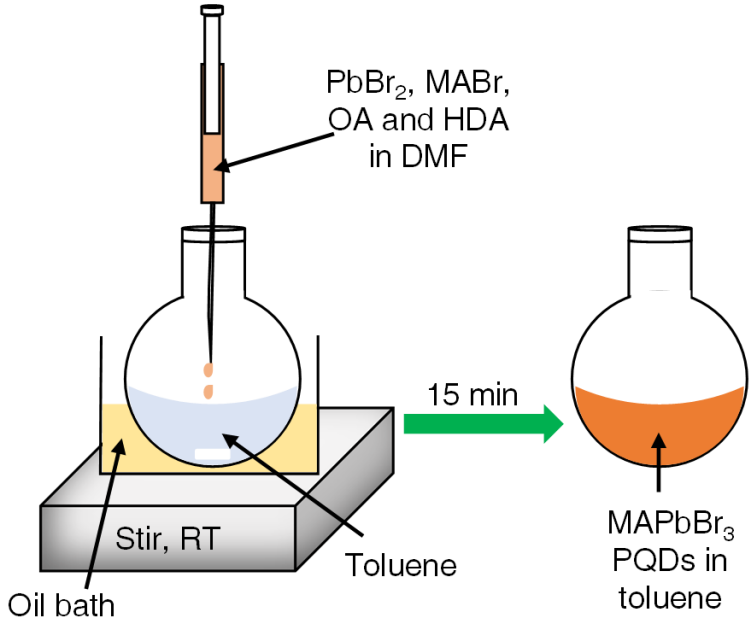

Figure 2.3. Schematic representation of the synthesis of $MAPbBr_3$ PQDs.

Hot-Injection

Synthesis of $CsPbBr_3$ PQDs

I synthesized $CsPbBr_3$ PQDs by following a reported hot-injection method,[5,7,8] and the synthesis scheme is shown in Figure 2.4. In a 500 mL round bottom flask, $PbBr_2$ (1.88 mmol, 690 mg), OA (12.6 mmol, 4 mL), HDA (15.2 mmol, 3.67 g), and 1-hexadecene

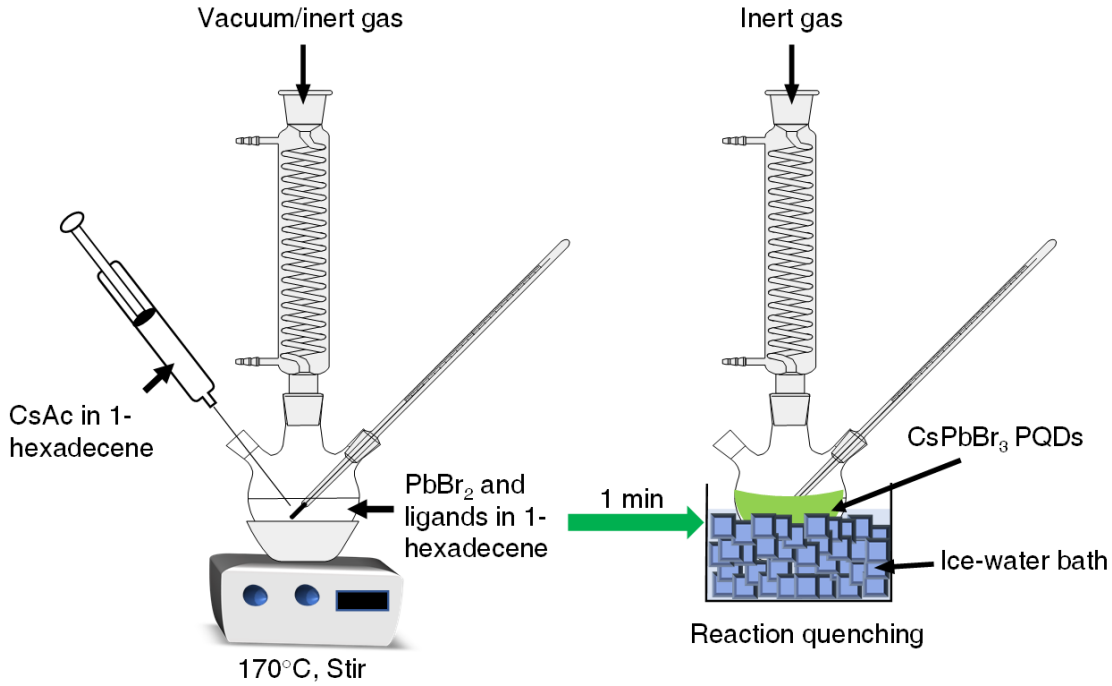

Figure 2.4. A scheme of the synthesis of $CsPbBr_3$ PQDs.

(90 mL) were mixed by stirring for 1 h under vacuum at 120 ℃. Parallelly, in another round bottom flask, CsAc (0.5 mmol, 9 mg) was solubilized in OA (3.15 mmol, 1 mL) and 1-hexadecene (10 mL) and kept stirring under vacuum at 120 ℃. After every 20 min, argon and vacuum were switched alternatively in the reaction mixture. When $PbBr_2$ was completely dissolved, the temperature was increased to 170 ℃ and kept under an inert atmosphere. The hot CsAc-ligand solution was injected into the $PbBr_2$-ligand solution. The color of the reaction mixture was changed to green. The reaction was arrested within 1 min by placing the reaction mixture in an ice-water bath. The mixture was centrifuged at 6000 rpm for 25 min, and the supernatant was discarded. The residue was suspended in a hexane-*n*-butanol mixture and further centrifuged. The remaining residue was dispersed in toluene for further studies. The PL properties of this $CsPbBr_3$ PQD are reported in Chapter 5.

Synthesis of Caesium Oleate (CsOL)

The synthesis was carried out similarly to a literature report.[9] In a round bottom flask, CsAc (1 mmol, 0.192 g) and OA(1 mmol, 0.32 mL) were dissolved in 1-octadecene (4.68 mL) by stirring at 110 ℃ under an argon atmosphere. After 30 min, the vacuum was applied at 110 ℃ for 3 h until all the bubbles subsided. The vacuum was applied very slowly to avoid vigorous bubble formation and the removal of acetic acid. After 3 h, argon was flushed again in the reaction mixture, and while cooling down to room temperature, the solution became like white-jelly. This synthesis yielded 0.2 M of CsOL in 1-octadecene. The studies related to CsOL are reported in Chapter 5.

Synthesis of Lead Oleate [$Pb(OL)_2$]

The synthesis was carried out similarly to a literature report.[10] In a round bottom flask, PbAc (12 mmol, 4.6 g) and OA (24 mmol, 7.6 mL) were dissolved in 1-octadecene (16.4 mL) at room temperature and under vacuum. After the gas evolution, the temperature was slowly increased to 120 °C (only after the bubbles subsides at each increase). The heating and stirring of the reaction mixture were stopped after 1 h, and the solution was stored in a glass vial. This reaction yielded 0.5 M of $Pb(OL)_2$ in octadecene. The $Pb(OL)_2$ was stored under argon and melted before use. The studies related to $Pb(OL)_2$ are reported in Chapter 5.

2.2.2 Sample Preparation for Single-Particle Imaging and Photoluminescence Lifetime Studies

For single-particle studies, a dilute suspension of PNCs (or PQDs) in toluene was dropped onto a glass coverslip and dragged using Whatman lens-cleaning paper. The amounts of PNCs or PQDs were selected to isolate 10-15 particles in a 50×50 μm^2 single-particle image frame. The samples were photoirradiated with 460 or 532 nm laser and observed on a fluorescence microscope. A PNC (or PQD) solution was drop-casted on a glass coverslip and photoirradiated with a 400 or 465 nm laser for lifetime studies.

In Chapter 3, a silicon chamber was prepared for studying the effect of argon environment on PNCs, as shown in Figure 2.5. First, a PNC suspension was dropped and dried inside the chamber. Then, another glass coverslip was attached with silicone glue on top of the chamber, and argon was flushed into the chamber from an argon-filled balloon.

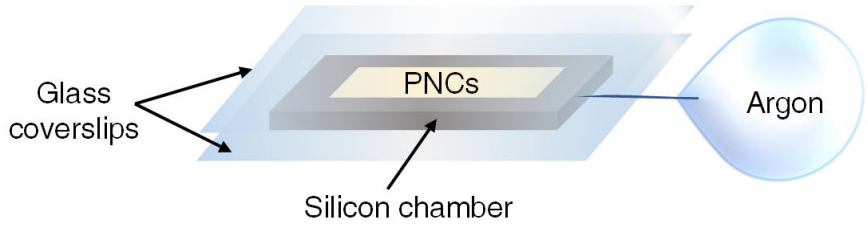

Figure 2.5. A silicon chamber for argon atmosphere-related studies.

In Chapter 4, for understanding the role of MAX on the PL properties of PQDs, first, the PL intensity trajectories and decay profiles of PQDs were recorded. Later, the MAX solution was carefully spread on the PQDs without disturbing the glass coverslip, as shown in Figure 2.6. Then, the PL intensity trajectories and decay profiles of MAX-treated PQDs were re-recorded. Through this approach, I observed the PL behavior of the same PQDs before and after the argon treatment. In chapter 5, I followed a similar procedure to understand the role of CsOL or $Pb(OL)_2$ on $CsPbBr_3$ PQDs. I recorded the PL intensity trajectories of the same $CsPbBr_3$ PQD before and after the treatment with CsOL [or $Pb(OL)_2$].

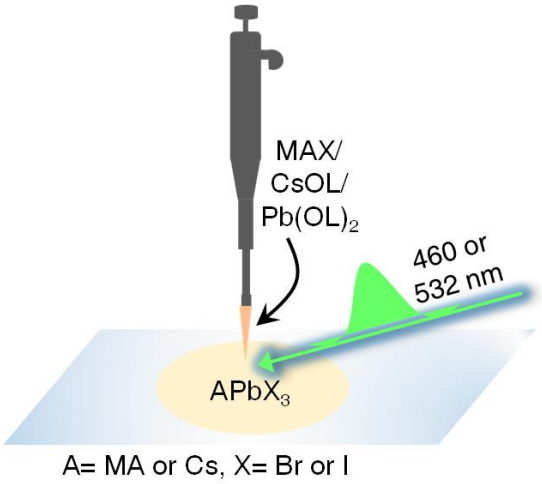

Figure 2.6. A scheme of sample preparation for analyzing the role of A-, B-, or X-site ions on PQDs.

2.2.3 UV-*vis* Absorption Spectroscopy

I used absorption spectroscopy to examine the optical excitation properties of the PNCs or PQDs. The PNC (or PQDs) were suspended in toluene, and the absorption spectra of the suspension were recorded by using a UV-*vis* spectrophotometer (Evolution 220, Thermo Fischer Scientific). The scheme for detecting the optical absorption of samples is shown in Figure 2.8. The absorption spectrophotometer works on the Beer-Lambert-Bouguer law. According to this law, the absorbance (A) of the solution is proportional to the concentration (c) and the path length (l), $A=\varepsilon cl$, where ε is the molar extinction coefficient (M^{-1} cm^{-1}). Typically, for absorbance, an excitation source with a wavelength in the 190-900 nm region is used. The excitation from the source passes through a monochromator and the sample solution. The solution absorbs a definite number of photons of a particular energy and the

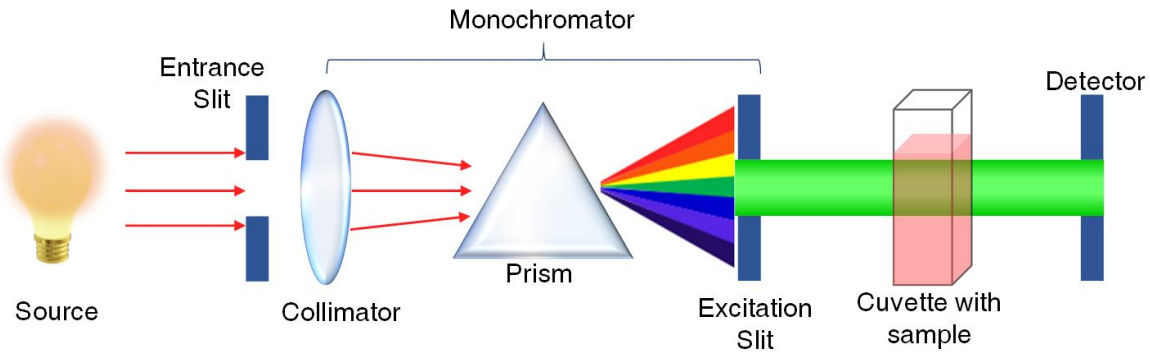

Figure 2.8. Schematic representation of the monochromator and the absorption detection.

nanocrystals/quantum dots get excited from the ground to the excited states. The detector records the transmitted light from the solution. In this thesis, I recorded the absorption spectra of the PNCs or PQDs from 400 to 900 nm wavelength range.

2.2.4 Steady-State Fluorescence Spectroscopy

I used a fluorescence spectrometer to examine the emission properties of the PNCs or PQDs. The spectrometer was used to understand the relaxation of excitons from the excited to the ground states. The fluorescence of PNC or PQD solutions, and PQD films were examined using the Fluorescence Spectrometer (F-4500, Hitachi) equipped with a Xe-lamp as the excitation source. The method of collecting the emitted light from the samples is shown in Figure 2.7. The Xe-lamp emits bright white light, which covers the UV to visible region. The desired excitation wavelength focused on the sample was selected by the excitation monochromator. The monochromator uses an assembly of diffraction gratings and slits, by which it selectively passes the desired wavelength. The sample was excited and emited photons were passed the emission monochromator. The emission starts at a longer wavelength than the excitation, so the emission monochromator efficiently filters the excitation light. The 90° angle between the excitation and emission paths limits the excitation light reaching the emission monochromator. Finally, the emission was detected by the photomultiplier tube. In this study, the PNC or PQDs solutions were prepared by suspending the samples in toluene, and the PQD films were prepared by drop-casting a suspension of PQDs on a micro slide glass (cut into 3.8 ×1.3 mm). A PQD film was kept

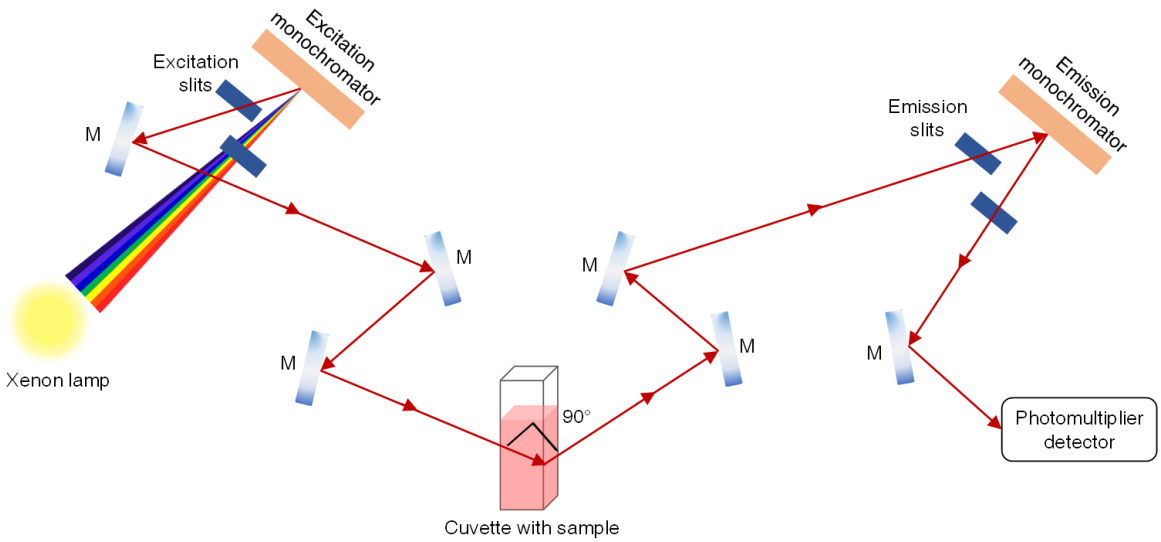

Figure 2.7. A scheme of a steady-state fluorescence spectroscopy system.

inside an empty cuvette at a 45° angle to maintain the maximum emission from the sample. The emission intensities from the samples were scanned as a function of the detection wavelength. The excitation wavelength was set at 500 nm for $MAPbI_3$ PNCs or PQDs, and 450 nm for $MAPbBr_3$ PQDs, and $CsPbBr_3$ PQDs.

2.2.5 Time-Resolved Fluorescence Spectroscopy

I used time-resolved fluorescence spectroscopy to analyze the average PL lifetime (τ_{avg}) of PNCs or PQDs. The τ_{avg} refers to the average time a photon excited sample spends in the excited state before relaxing to the ground state. The PL lifetime is inversely proportional to the sum of radiative and nonradiative recombination rates. Therefore, it can help in calculating the rates of trap-assisted nonradiative recombination of PNCs and PQDs. So, calculating PL lifetime assists in understanding the excitonic properties of PNCs or PQDs. The optical setup of time-resolved spectroscopy is shown in Figure 2.9.

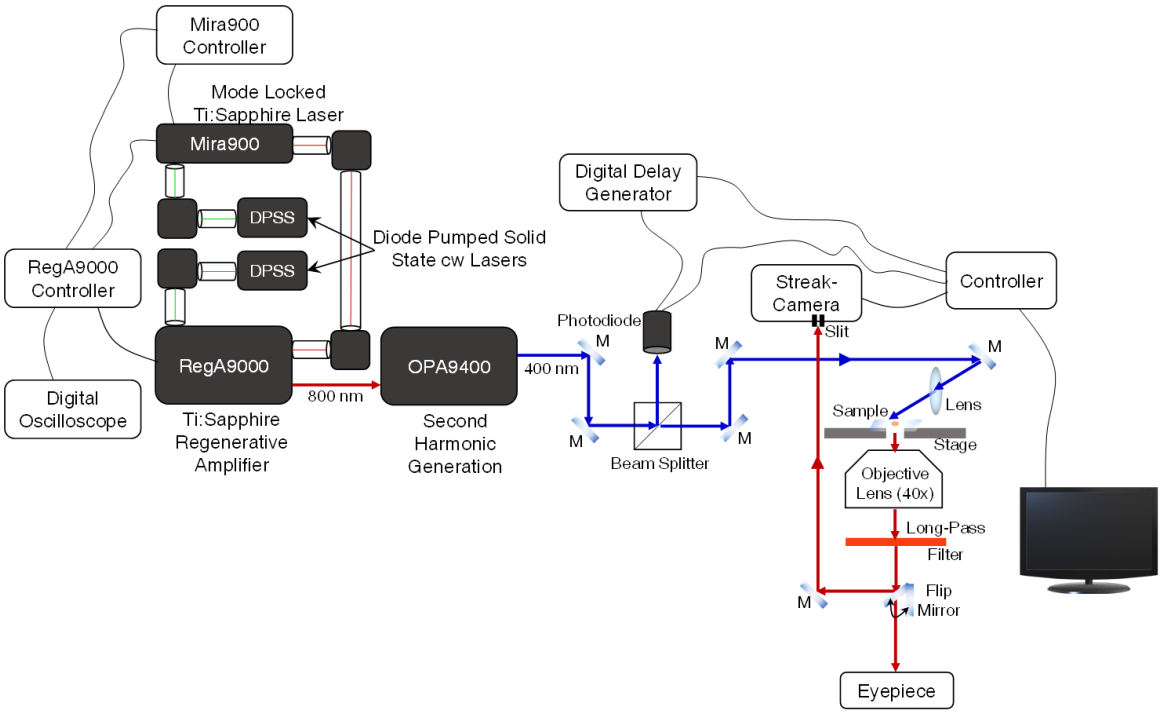

Figure 2.9. A scheme of the optical setup for collecting fluorescence decays.

The diode pump lasers were used as the excitation source for oscillator (Mira900, Coherent) with the repetition rate of 76 MHz. The mode-locked pulses from Mira900 were amplified to microjoules by the regenerative amplifier (RegA9000, Coherent). The 800 nm output from RegA frequency doubled in an OPA (optical parametric amplifier). The 405 nm

output from the OPA was used as the excitation light source in PL lifetime studies. The PL decay profiles of PNCs (or PQDs) were recorded using an assembly of a polychromator (model 250IS, Chromex) and a photon-counting Streak-camera (C4334, Hamamatsu Photonics).

I placed the PNC- (or PQD-) coated glass coverslip on an XY stage attached to an inverted optical microscope (IX70, Olympus). The emission signals from the samples passed through an objective lens (40x, 0.60 NA, Olympus) and filtered using a long-pass filter (LPF). The objective lens with a high numerical aperture was used for a higher spatial resolution, which can diminish the backscattering and collect the maximum emission. Further, the emission was focused at the polychromator entrance slit and detected with the Streak-camera. I used 580 nm LPF for $MAPbI_3$ PNCs (or PQDs), and 500 nm LPF for $MAPbBr_3$ PQDs. I also used neutral density filters for controlling the excitation power intensity.

The PL decays were fitted with the following third-exponential fitting equation,

$$y = y_0 + A_1 e^{-\frac{t-t_0}{\tau_1}} + A_2 e^{-\frac{t-t_0}{\tau_2}} + A_3 e^{-\frac{t-t_0}{\tau_3}} \quad (2.1)$$

and or the fourth-exponential fitting equation,

$$y = y_0 + A_1 e^{-\frac{t-t_0}{\tau_1}} + A_2 e^{-\frac{t-t_0}{\tau_2}} + A_3 e^{-\frac{t-t_0}{\tau_3}} + A_4 e^{-\frac{t-t_0}{\tau_4}} \quad (2.2)$$

Here, t is time, A_1, A_2, A_3, and A_4 are amplitudes, and τ_1, τ_2, τ_3, and τ_4 are the corresponding lifetime components. The intensity-averaged lifetime (τ_{avg}) was calculated by using the,

$$\tau_{avg} = \sum \frac{A_i \tau_i}{A_i} \quad (2.3)$$

Time-Correlated Single-Photon Counting System (TCSPC)

I used a TCSPC system attached with a 465 nm picosecond laser (Advanced Laser Diode Systems, 1 MHz) for detecting the PL decays of PQDs. Figure 2.10 shows the optical setup used for recording PL decay profiles on a confocal fluorescence microscope (IX71, Olympus). This setup uses an avalanche photodiode (SPCM-AQR, PerkinElmer) and a single-photon counting module (SPC-830, Becker & Hickl GmBH). The suspension of PQDs in toluene was drop-cast on a glass coverslip, and the sample was placed on the

microscopr-XY movable stage. The laser reflected on a dichroic mirror (transmission >90% in 460-700 nm, and >15% at 750-950 nm) before irradiating the PQDs. The emission from the PQDs was collected by an objective lens (40x, 0.75 NA, UPLanFL N), passed the dichroic mirror, and filtered through a 500 nm LPF. Further, the emission was detected through the TCSPC system. The PL decays were fitted with eq. 2.2, and the τ_{avg} of the PQDs was estimated with eq. 2.3.

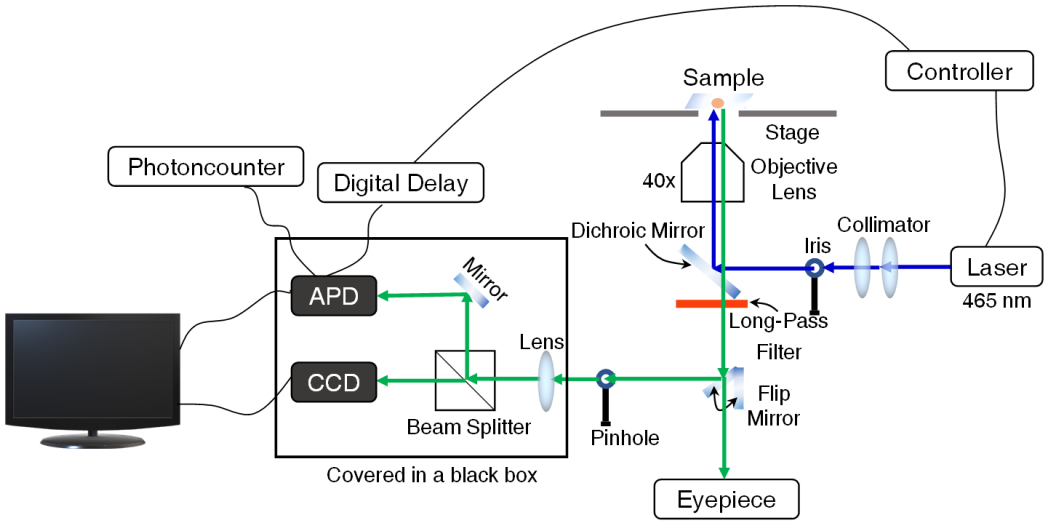

Figure 2.10. A schematic of the optical setup for recording time-resolved fluorescence decays.

I also used a Qunataurus-tau (Hamamatsu, C11367-21) system for recording PL decay profiles of $CsPbBr_3$ PQDs. The Qunataurus-tau system consists of several LEDs at different wavelengths as excitation sources. I recorded the PL decays of PQDs for 3 min by exciting with the 470 nm LED. The τ_{avg} of the PQDs was estimated with eq. 2.3.

2.2.6 Single-Particle Microspectroscopy

I used single-particle microspectroscopy with a wide-field illumination optical setup to examine the PL from single PNCs (or PQDs). Wide-field fluorescence spectroscopy yields a more prominent focal spot than confocal fluorescence spectroscopy, which helps obtain collective fluorescence from all the PNCs (or PQDs) in the field of view. I placed the PNC- or PQD- coated glass coverslip on an XY stage attached to an inverted optical microscope (IX70, Olympus), and photoexcited the samples with a cw laser (450 nm, Figure 2.11a). The microscope was equipped with an electron-multiplying charge-coupled device (EMCCD, iXON, Andor Technology), and an objective lens (40x, 0.60 NA, Olympus). The

focal spot in this optical setup was greater than the Abbe diffraction limit. The binning time of the EMCCD was set at 32 ms for collecting the PL signals from the samples. In other words, the PL signals were averaged every 32 ms. An EMCCD camera amplifies the emission signal before it reaches the detector and limits the noise signals. The inside structure of the EMCCD is shown in Figure 2.11b.

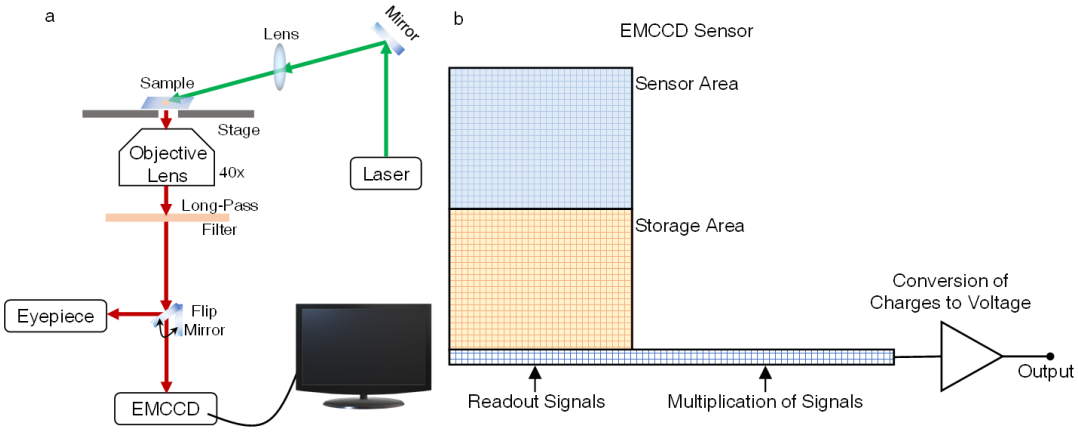

Figure 2.11. (a) The optical setup for single-particle imaging. (b) The inside structure of an EMCCD sensor.

An EMCCD collects and multiplies the signals at high speed. I used the operation of frame transfer for acquiring data from the EMCCD. The frame transfer feature is divided into two portions, (i) sensor and (ii) storage area. In the sensor area, the image is captured when exposed to light during the measurements. This image is transferred to the storage area. The storage area is shielded with an opaque mask, which acts as an electronic shutter. In the storage area, the image is already saved before reading the signals. While reading the signals, another image will be captured by the sensor and transferred to the storage, as the sample is continuously exposed to light. After reading out the signals from frame transfer areas, they will shift towards the multiplication chip to amplify before reaching the output. I set the EM gain at 100, where the signal-to-noise ratio is at the optimum for my studies. This way, from a single frame, complete PL blinking statistics of many isolated PNCs or PQDs were collected rapidly with high precision. The PL intensities were recorded as a function of time to distinguish between the high (ON) and low (OFF) intensity durations.

The excitation sources for $MAPbI_3$ PNCs (or PQDs) was a 532 nm cw laser (Millenia IIs, Spectra Physics), $MAPbBr_3$ PQDs were a 404 nm LED laser (ThorLabs) or a 460 nm cw laser (ACAN, A12), and $CsPbBr_3$ PQDs was the 460 nm cw laser. The LPF used in the

experiment for $MAPbI_3$ PNCs (or PQDs) was 580 nm, and for $MAPbBr_3$ and $CsPbBr_3$ PQDs was 500 nm. The ON- and OFF-time probability distributions of single-particle PL intensity trajectories were fitted by the truncated and linear power-laws described in Chapter 1 (Section 1.2.2, eq. 1.5-1.7).

Single-Photon Correlation Measurements

I used the photon correlation function for estimating the single-emitting particles. Photon antibunching is the process of determining the correlation between equally spaced photons. The emission was collected by using a confocal fluorescence microscope. Here, the laser diverges from a beam splitter and passes through an objective lens to the sample. A sample placed on the microscope stage is excited and emits photons. The emitted photons were collected by an objective lens and passed a LPF and a lens. In the end, the photons were detected by two APDs. In this study, the PQDs were photoexcited with a 450 nm pulsed laser (125 fs pulse width, 8 MHz repetition rate). Two APDs detected the coincidence counts of the photons, and the correlation of photons was scanned as a function of time. The photon coincidence counts of $MAPbI_3$ PQDs are shown in chapter 4.

2.2.7 Scanning Transmission Electron Microscopy (STEM)

I used the STEM Hitachi HD-2000 Ultra-thin Film instrument, operating at 200 kV for analyzing the shape and size of the PNCs or PQDs. In the STEM, an image of the sample is obtained after an electron beam is transmitted through the particles in the observation area. I used carbon-coated STEM Cu100P grids as the sample holder. I prepared suspensions of PNCs or PQDs in toluene and dropped the suspension on the Cu-grid. The Cu-grids were dried under vacuum overnight before the examination. The collected images were analyzed by ImageJ software for calculating the mean size of the PNCs or PQDs.

2.2.8 Powder X-ray Diffraction

I used XRD for analyzing the phase and shape of the PNCs. I used an X-ray diffractometer (RINT 2200, Rigaku), which uses $Cu\ K\alpha_1$ excitation at λ=1.5406 Å. The XRD spectroscopy consists mainly of three components, (i) a cathode ray tube, (ii) a sample holder, and (iii) a detector. The cathode ray tube generates an X-ray beam when electrons from the inner shell

($K\alpha_1$) are knocked out using an electron beam. The X-ray beam is directed towards the sample, which is rotating continuously with the detector. The reflected X-ray is collected by the detector. Here, the sample rotates at an angle θ, whereas the detector rotates at an angle 2θ. The rotation of the sample provides the XRD from all the possible lattices scanned by the detector. The XRD peaks can be designated by miller indices, and the miller indices (*hkl*) are calculated by using Bragg's Law,

$$d_{hkl} = \frac{\lambda}{2\,sin\theta} \tag{2.4}$$

where λ is the X-ray wavelength, and d_{hkl} is the interplanar spacing. For a tetragonal unit cell, d_{hkl} is calculated as,

$$\frac{1}{d_{hkl}^2} = \frac{h^2 + k^2}{a^2} + \frac{l^2}{c^2} \tag{2.5}$$

Here, *a* and *c* are the lattice constants.

For collecting the XRD pattern of $MAPbI_3$ PNCs, I dried the PNCs under vacuum and crushed the powder with a hand mortar. This way, I prepared a fine powder of the PNCs. From that, *ca* 30 mg of the $MAPbI_3$ PNC powder was examined under an XRD. The obtained XRD pattern was compared with the reference data for confirming the phase of the PNCs. I calculated the miller indices for $MAPbI_3$ PNCs by using the lattice constants for $MAPbI_3$ (*a*=8.83 Å, *c*=12.69 Å) from the literature.[11]

2.2.9 Scanning Electron Microscopy with Energy Dispersive X-ray Spectroscopy (SEM-EDX)

I used SEM (Hitachi SU8230) attached with an EDX (Bruker QUANTEX EDS) system, which operates at 15 kV, for analyzing the elemental composition in PQDs. In SEM, an image of the sample is obtained after an electron beam hits the sample and the energy transports to the atom. This energy excites an electron from a shell, which leaves a hole behind. A characteristic X-ray is released when the electron from a higher shell recombines with the hole in the lower shell. The energies of the X-rays are analyzed through EDX. I prepared a suspension of PQDs in toluene and drop-cast on an ITO glass. The sample was dried under vacuum for 2 h before the experiment. The PQDs coated on the ITO glass were analyzed using the SEM-EDX.

2.3 References

(1) Wang, L.; Williams, N. E.; Malachosky, E. W.; Otto, J. P.; Hayes, D.; Wood, R. E.; Guyot-Sionnest, P.; Engel, G. S. Scalable Ligand-Mediated Transport Synthesis of Organic-Inorganic Hybrid Perovskite Nanocrystals with Resolved Electronic Structure and Ultrafast Dynamics. *ACS Nano* **2017**, *11*, 2689–2696.

(2) Zhang, F.; Zhong, H.; Chen, C.; Wu, X. G.; Hu, X.; Huang, H.; Han, J.; Zou, B.; Dong, Y. Brightly Luminescent and Color-Tunable Colloidal $CH_3NH_3PbX_3$ (X = Br, I, Cl) Quantum Dots: Potential Alternatives for Display Technology. *ACS Nano* **2015**, *9*, 4533–4542.

(3) Hassan, Y.; Ashton, O. J.; Park, J. H.; Li, G.; Sakai, N.; Wenger, B.; Haghighirad, A. A.; Noel, N. K.; Song, M. H.; Lee, B. R.; Friend, R. H.; Snaith, H. J. Facile Synthesis of Stable and Highly Luminescent Methylammonium Lead Halide Nanocrystals for Efficient Light Emitting Devices. *J. Am. Chem. Soc.* **2019**, *141*, 1269–1279.

(4) Zhang, F.; Huang, S.; Wang, P.; Chen, X.; Zhao, S.; Dong, Y.; Zhong, H. Colloidal Synthesis of Air-Stable $CH_3NH_3PbI_3$ Quantum Dots by Gaining Chemical Insight into the Solvent Effects. *Chem. Mater.* **2017**, *29*, 3793–3799.

(5) Ghimire, S.; Chouhan, L.; Takano, Y.; Takahashi, K.; Nakamura, T.; Yuyama, K.; Biju, V. Amplified and Multicolor Emission from Films and Interfacial Layers of Lead Halide Perovskite Nanocrystals. *ACS Energy Lett.* **2019**, *4*, 133–141.

(6) Veldhuis, S. A.; Tay, Y. K. E.; Bruno, A.; Dintakurti, S. S. H.; Bhaumik, S.; Muduli, S. K.; Li, M.; Mathews, N.; Sum, T. C.; Mhaisalkar, S. G. Benzyl Alcohol-Treated $CH_3NH_3PbBr_3$ Nanocrystals Exhibiting High Luminescence, Stability, and Ultralow Amplified Spontaneous Emission Thresholds. *Nano Lett.* **2017**, *17*, 7424–7432.

(7) Protesescu, L.; Yakunin, S.; Bodnarchuk, M. I.; Krieg, F.; Caputo, R.; Hendon, C. H.; Yang, R. X.; Walsh, A.; Kovalenko, M. V. Nanocrystals of Cesium Lead Halide Perovskites ($CsPbX_3$, X = Cl, Br, and I): Novel Optoelectronic Materials Showing Bright Emission with Wide Color Gamut. *Nano Lett.* **2015**, *15*, 3692–3696.

(8) Hu, Z.; Liu, Z.; Bian, Y.; Li, S.; Tang, X.; Du, J.; Zang, Z.; Zhou, M.; Hu, W.; Tian, Y.; Leng, Y. Enhanced Two-Photon-Pumped Emission from *in Situ* Synthesized

Nonblinking $CsPbBr_3/SiO_2$ Nanocrystals with Excellent Stability. *Adv. Opt. Mater.* **2018**, *6*, 1700997.

(9) Lu, C.; Wright, M. W.; Ma, X.; Li, H.; Itanze, D. S.; Carter, J. A.; Hewitt, C. A.; Donati, G. L.; Carroll, D. L.; Lundin, P. M.; Geyer, S. M. Cesium Oleate Precursor Preparation for Lead Halide Perovskite Nanocrystal Synthesis: The Influence of Excess Oleic Acid on Achieving Solubility, Conversion, and Reproducibility. *Chem. Mater.* **2019**, *31*, 62–67.

(10) Utzat, H.; Sun, W.; Kaplan, A. E. K.; Krieg, F.; Ginterseder, M.; Spokoyny, B.; Klein, N. D.; Shulenberger, K. E.; Perkinson, C. F.; Kovalenko, M. V.; Bawendi, M. G. Coherent Single-Photon Emission from Colloidal Lead Halide Perovskite Quantum Dots. *Science* **2019**, *363*, 1068–1072.

(11) Saidaminov, M. I.; Abdelhady, A. L.; Murali, B.; Alarousu, E.; Burlakov, V. M.; Peng, W.; Dursun, I.; Wang, L.; He, Y.; MacUlan, G.; Goriely, A.; Wu, T.; Mohammed, O. F.; Bakr, O. M. High-Quality Bulk Hybrid Perovskite Single Crystals within Minutes by Inverse Temperature Crystallization. *Nat. Commun.* **2015**, *6*, 7586.

Chapter 3

Photostability of Perovskite Nanocrystals

Abstract

In this chapter, I studied the role of oxygen on the methylammonium lead halide perovskite nanocrystals at the ensemble and the single-particle level. The perovskite nanocrystals are prone to degradation under moisture, oxygen, and light. Therefore, to overcome this issue, I analyzed the mechanism of electron transfer and charge carrier recombination to understood the degradation process of perovskite nanocrystals. Under the photoexcited state of perovskite nanocrystals, the electron transfers from perovskite to molecular oxygen and forms superoxide, which occupies the halide vacancy in the perovskite nanocrystal and deteriorate the PNCs. Therefore, the photoluminescence intensity of the methylammonium lead halide perovskite nanocrystals continuously decreases in air. For suppressing oxygen reactivity, I introduced argon to PNCs or coated the PNCs with polymer-matrix to enhance the photoluminescence of perovskite nanocrystals. I also found single-particle photoluminescence intensity trajectories with a long-living OFF-state in air, which showed complete photoluminescence recovery to the original level. Such photoluminescence behavior and the lower rate of electron transfer than that of the rate of nonradiative relaxation during an OFF-state suggest that the perovskite nanocrystals don't undergo degradation and generate superoxide during the ionized state. The neutral excited state of perovskite is vulnerable to oxygen reactivity, which degrades the perovskite nanocrystals, whereas the ionized state prevents the oxidation of perovskite. I distinguished between charge carrier recombination and electron transfer mechanisms in methylammonium lead iodide perovskite nanocrystals by considering the photoluminescence behavior in ON- and OFF-states.

3.1 Introduction

The emerging semiconductor class of halide perovskites are promising for low-cost optical, electronic, and photovoltaic devices such as solar cells, LEDs, lasers, batteries, and photodetectors.[1–14] In the last decade, the power conversion efficiency of perovskite solar cells has increased from 3.8% to >26%, and the external quantum efficiency of perovskite LEDs also boosted from 0.76 to >20%.[1,15–17] However, the stability of these devices is a challenge for commercialization. The responsible factors for long-term stability are the intrinsic defects present in the crystal lattice. In an ideal case, all the atoms occupy specific positions in the lattice, such as MA^+ locates inside the $[PbX_6]_4^-$ octahedrons. Any variation in the localization of the atoms can be term as defects. Such as structural defects, which consist of atom vacancies, antisites, and interstitial sites. The structural defects can restrict the movement of free charge carriers and trap them at the defect sites. The energy levels of these defects are at a different level (deep or shallow) as that of the valence and conduction bands, where photogenerated charge carriers get trap. The shallow defects, close to the valence and conduction bands, are less harmful than those of the deep defects. These shallow defects mainly contribute to the loses of internal energy of the perovskite. A small amount of additional energy (thermal or activation) can help trap charge carriers to escape from the shallow defects.[18,19] On the other hand, deep defects form within the material bandgap contribute to trapping the charge carriers and fast nonradiative recombination.[20]

In lead halide perovskites, the local atmosphere plays a significant role in forming shallow and deep traps in the energy levels of perovskite, such as moisture, water, oxygen, temperature, pressure, and light.[21–24] Furthermore, the oxygen-induced degradation of lead halide perovskite is one of the main unresolved issues.[23,25–34] The role of oxygen in decreasing photoluminescence (PL) efficiency has been reported by Haque and coworkers.[23,25] They demonstrated superoxide generation by the electron transfer from the methylammonium lead iodide ($MAPbI_3$) perovskite to molecular oxygen. The generated superoxide occupies the halide vacancy and deprotonates methylammonium cation, which leads to the structural disintegration of the perovskite film into methylamine (CH_3NH_2), I_2, lead iodide (PbI_2), and H_2O.[25] To control the electron transfer to oxygen, they employed a layer of TiO_2 on the perovskite and minimized perovskite's oxidation by blocking the generation of superoxide.[23] Furthermore, ab initio studies by Zhang and Sit on the generation of superoxide from $MAPbI_3$ perovskite suggested that the surface Pb^{2+} ions react with superoxide. The superoxide will break the Pb-X bond and form a covalent bond with

lead, Pb-O, which is responsible for the disintegration of the octahedral structure PbX_6.[28] The disintegration of perovskite by the oxygen species enhanced under photoexcitation leading to the formation of charge carrier traps because of the uncoordinate bond between the superoxide and the crystal. These traps cause two times faster nonradiative recombination compared to that of the pristine sample. Therefore, charge carrier dynamics of the perovskite are greatly affected by the superoxide, which promotes atomic fluctuations by the breaking of crystal geometry.[35,36] Péan *et al.* showed that superoxide generation depends on various factors such as the intensity of oxygen diffusion, the density of defects and grains, and the perovskite morphology.[37] Conversely, various contradicting theories about the role of oxygen in the structural deterioration of halide perovskite are present. For example, the passivation of superoxide at halide vacancies and other defects with oxides increases the PL quantum efficiency.[31,38–40] Scheblykin and coworkers observed enhanced PL quantum efficiencies through the photochemical reaction of oxygen to trap states in $MAPbI_3$.[39] Also, Brenes *et al.* explained through density functional theory calculations that in the perovskite film, oxygen molecule and surface iodide vacancies bind strongly. This correlation leads to the formation of a thin passivating layer of moisture, which reduces the subband gap traps and reorganizes the band structure to that of a pristine case.[31] The two contradicting theories related to the roles of oxygen on the defect passivation, degradation, and quenching and enhancement of PL quantum efficiency of perovskites attracted me to investigate the relation between oxidation and reactive state on PL of perovskite nanocrystals (PNCs).

This chapter correlates the ensemble and single-particle PL behavior of $MAPbI_3$ PNCs in aerobic and anaerobic conditions. Here, I analyzed the effect of superoxide on PNCs during the ON- and OFF-state and observed that the ON-states are susceptible to react with superoxide, whereas OFF-state hinders the oxidation of perovskite. Through ensemble and single-particle studies, I examined that the PL intensity of PNCs continuously decreases in air. In contrast, PL stabilizes in argon and polymer environments under a similar photoexcitation intensity. Additionally, in air, after a long-OFF state, the PNC recovers its PL to the original level, suggesting that the ionized form of PNCs doesn't involve in the oxidation of PNC, the generation and reaction of superoxide with PNC. From analyzing the PL decay profiles of $MAPbI_3$ PNCs, I observed that argon atmosphere increases the charge carrier lifetime compared to the air atmosphere irrespective of the excitation intensity. I also estimated that under OFF-state, the rate of nonradiative

recombination is higher than that of the electron transfer rate to oxygen, which guided the photodegradation and PL blinking mechanism of PNCs.

3.2 Results and Discussion

3.2.1 Characterization of $MAPbI_3$ Perovskite Nanocrystals

I synthesized $MAPbI_3$ PNCs by a modified ligand-mediated transport method.[41] In this synthesis, I dissolved lead iodide and methylamine hydroiodide in hexane along with the ligands, oleic acid and hexadecylamine. The synthesis is described in section 2.2.1. The PNCs were characterized by absorption and fluorescence spectroscopy, XRD, and TEM. The absorption and fluorescence spectra of these PNCs are shown in Figure 3.1a. The PNCs showed broad absorption in the UV-visible region and narrow emission in the near-infrared region *ca* 720 nm, with full-width at half maximum of ~55 nm. For single-particle studies, the PNCs were suspended in toluene and drop-cast on a glass coverslip. The uniform distribution of single PNCs was observed under an EMCCD (Figure 3.1b). Further, for

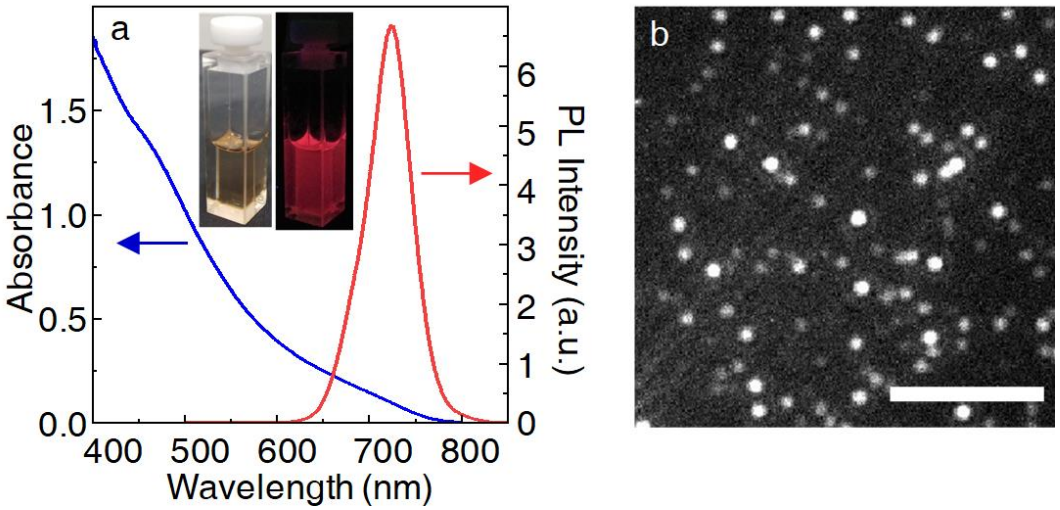

Figure 3.1. (a) Absorption and emission spectra of $MAPbI_3$ PNCs suspended in toluene. [Inset: Images of $MAPbI_3$ PNC suspension in cuvette under room light (left) and UV light (right)]. (b) Single-particle PL image of $MAPbI_3$ PNCs photoexcited with 532 nm cw laser (excitation intensity was 825 W cm^{-2}, scale bar: 10 µm)

calculating the size of the PNCs, TEM images were analyzed. One such TEM image is shown in Figure 3.2a. I used ImageJ software to estimate >100 PNCs and constructed the size distribution histogram (Figure 3.2b). The average size of $MAPbI_3$ PNCs is estimated

at 11.5±2.1 nm. I also analyzed the crystal phase and space group from the XRD pattern. Figure 3.2c shows the XRD pattern with the corresponding miller indices for $MAPbI_3$ PNCs. I compared the XRD pattern of the tetragonal phase of $MAPbI_3$ single crystal from Saidaminov *et al.* In the tetragonal phase, two among three lattice constants (*a*, *b*, *c*) are the same, *a*=*b*=8.83Å and *c*=12.68Å.[14] In this report, the main miller indices of tetragonal phase with space group *I4/m* for $MAPbI_3$ crystal were (110), (112), (211), (202), (220), (114), (312), (224), and (314), which lies around 14°, 20°, 23°, 24°, 28°, 32°, 35°, 41°, 43°, 46°, and 47° Bragg's diffraction peaks, respectively. As shown in Figure 3.2c, the XRD pattern of $MAPbI_3$ PNCs in this study matches to that in the literature. Thus, I confirm that the PNCs are in the tetragonal phase with space group *I4/m*.

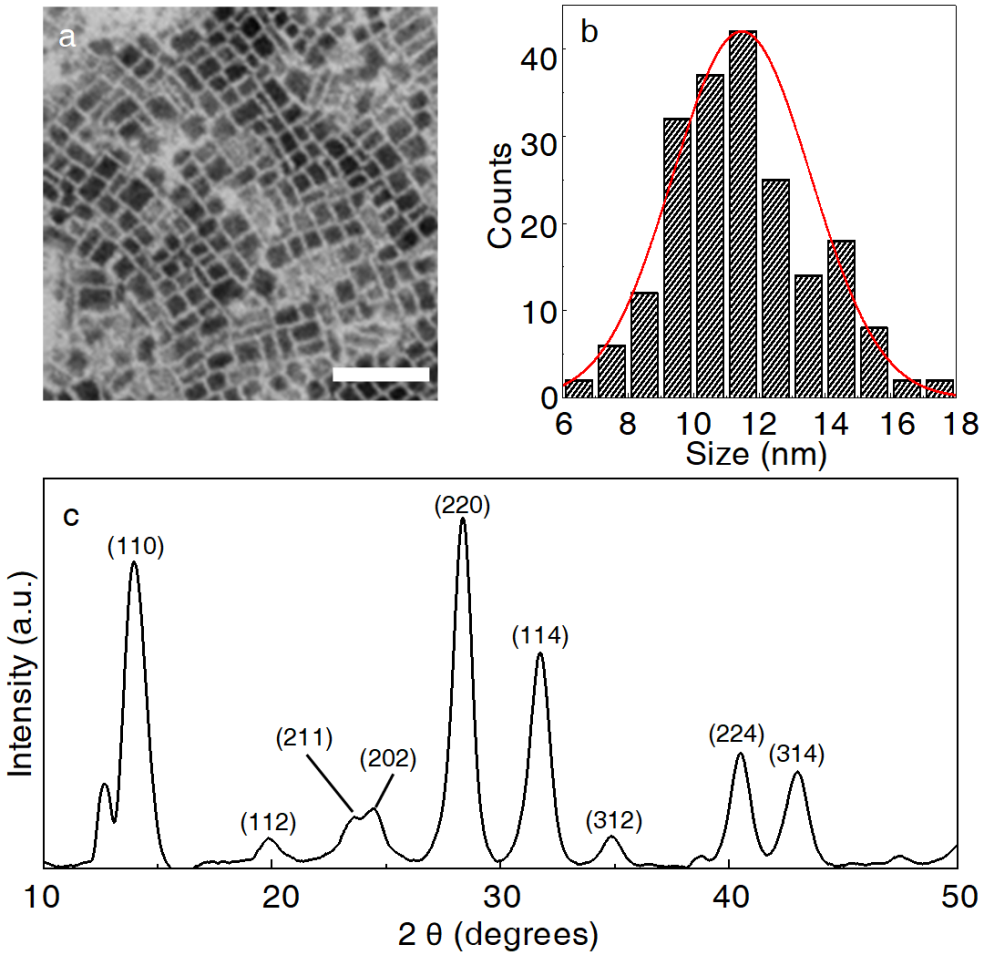

Figure 3.2. Characterization of size and shape of $MAPbI_3$ PNCs. (a) TEM image (Scale bar: 50 nm) and (b) its corresponding PNC size histogram. (c) XRD peaks with corresponding miller indices.

3.2.2 Photodegradation and Photostability

To confirm the photostability of $MAPbI_3$ PNCs, I carried out a time-controlled PL experiment. I suspended $MAPbI_3$ PNCs in toluene and photoexcited with 532 nm laser at excitation power intensity of 50 mW cm^{-2}. The PL intensities of $MAPbI_3$ PNCs were recorded every 2 min of photoexcitation in air and argon environment. As shown in Figures 3.3a and b(i), the PL intensity drastically decreased by 68% in 30 min, when the PNC suspension was saturated by air. This decrease in the PL intensities under air saturation corresponds to the generation of superoxide and its reaction with the $MAPbI_3$ PNCs. Haque and coworkers demonstrated that the electron transfers from the excited perovskite to the oxygen and generates the superoxide, deprotonates the MA-cation, occupies the halide

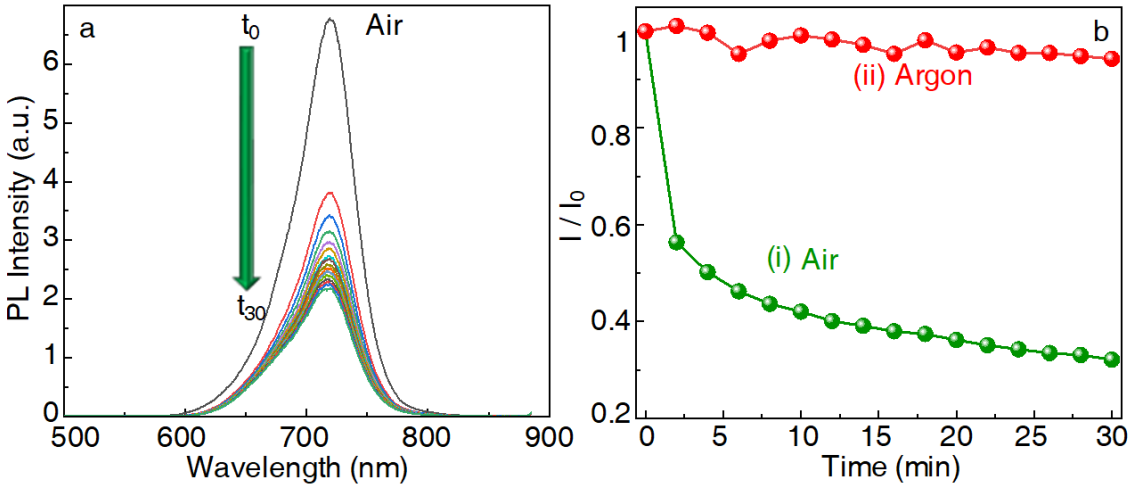

Figure 3.3. Photostability of $MAPbI_3$ PNCs. (a) PL spectra of PNCs saturated with air under photoexcitation by 532 nm cw laser (50 mW cm^{-2}), and (b) the relative PL intensities recorded every 2 min of photoirradiation under (i) air and (ii) argon atmosphere.

vacancies, and deteriorates the $MAPbI_3$ PNCs.[23,25] Another report by Hong *et al.* reported that the decrease in PL attributes to the activation and deactivation of photoinduced quenching traps.[42] By acquiring halide vacancies, the superoxide contributes to the formation of electron and hole traps and quenches the PL. Therefore, to suppress the oxygen reactivity, I checked the PL behavior under argon environment. I continuously purged argon into the suspension of PNCs during the experiment and recorded the PL intensities every 2 min of photoexcitation. As shown in Figure 3.3b(ii), when argon was introduced, the PL intensities of the $MAPbI_3$ PNCs were stable for a long time under similar

photoexcitation. This suggests that the electron transfer from oxygen to the PNCs was reduced under argon atmosphere, and the superoxide generation was suppressed.

3.2.3 Photoluminescence Blinking of $MAPbI_3$ Nanocrystals

To understand the mechanism of the generation of superoxide and the oxidation of PNCs, single-particle experiments were carried out. I recorded the PL intensity trajectories of single $MAPbI_3$ PNCs under air/glass, argon/glass, polymer/glass, and dry-air/glass interfaces. Detailed information about the experimental setup of single-particle microspectroscopy is given in Chapter 2, section 2.2.6. For recording PL intensity trajectories of single PNCs under air/glass interface, I drop-cast the PNCs on a glass coverslip and excited with 532 nm cw laser (825 W cm^{-2}). The PL intensity trajectories of single PNCs at the air/glass interface show distinct ON- and OFF-events, as shown in Figure 3.4. When the particle was in ON-state, there was a gradual decrease in the PL

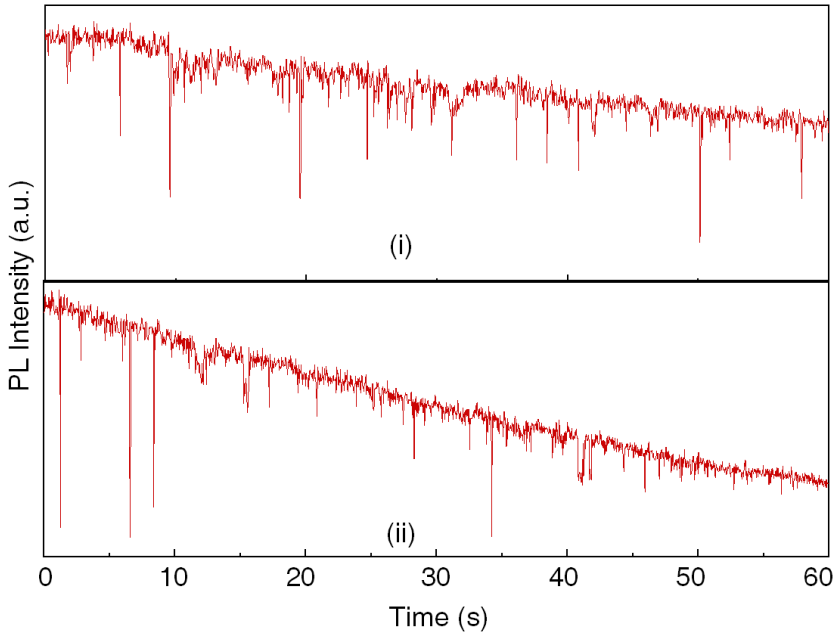

Figure 3.4. Typical single-particle PL intensity trajectories of $MAPbI_3$ PNCs in air. The PNCs were excited with a 532 nm cw laser.

intensity, which varied from particle to particle. Some PNCs degraded slowly [Figure 3.4(i)], and some degraded within 1 min of photoirradiation [Figure 3.4(ii)]. The decrease in PL intensity attributes to the disintegration of the PNCs by the passivation of superoxide on the surface iodine vacancies. As explained in the literature, the more the concentration

of halide defects, the more likely the superoxide will generate.[25] Therefore, the ability of oxygen to diffuse in the PNC will determine the rate of degradation.

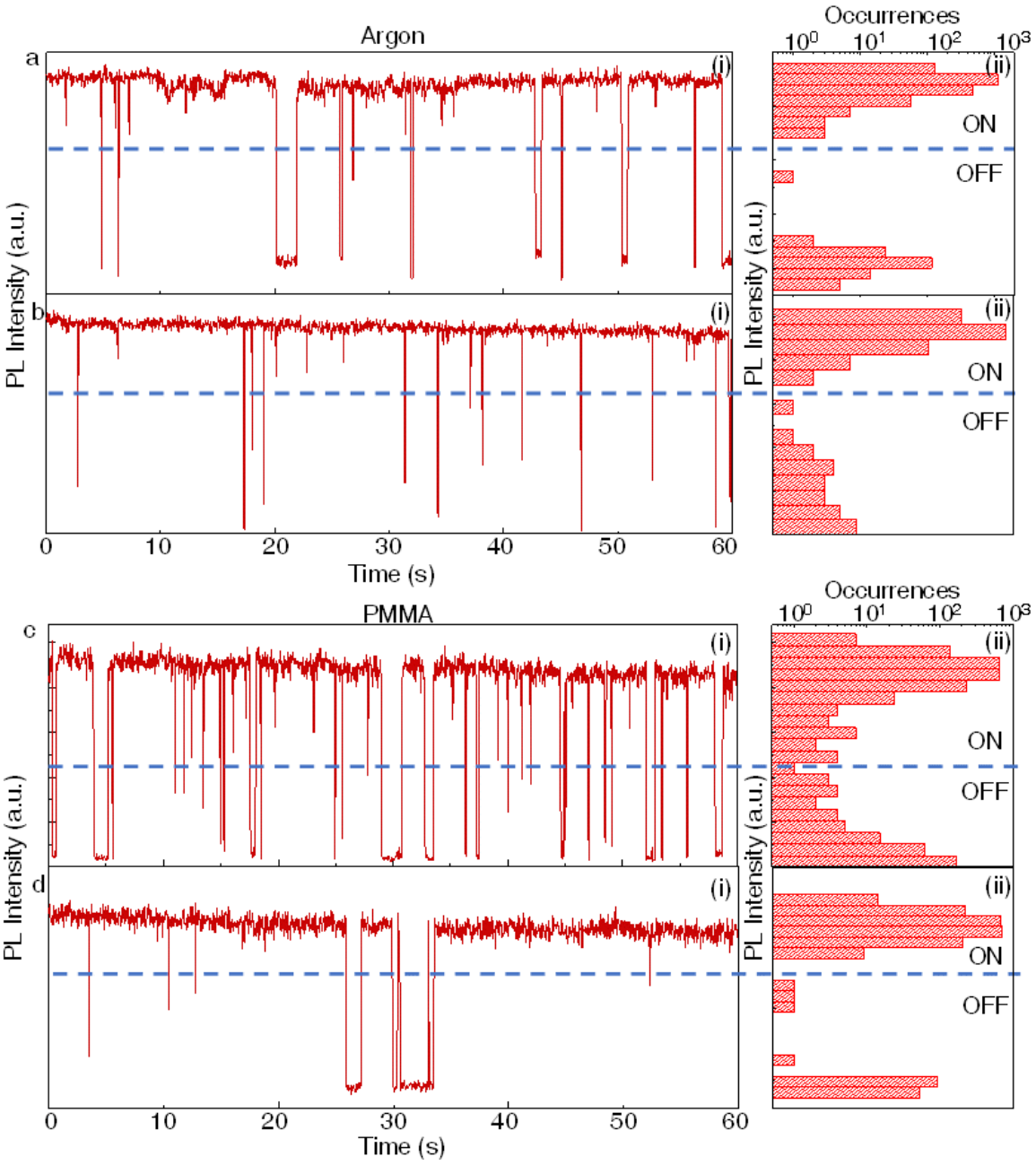

Figure 3.5. Typical single-particle (i) PL intensity trajectories and (ii) the corresponding occurrences of $MAPbI_3$ PNCs (a,b) at argon/glass interface and (c,d) after surface polymerization with poly(methyl methacrylate) [PMMA] and photoexcited by a 532 nm cw laser. The dashed line denotes the threshold for determining ON and OFF-events.

Like the ensemble experiment, for suppressing the oxygen reactivity and the degradation of PNCs, I saturated the PNCs with argon. For argon/glass interface, a silicon

chamber was prepared, as explained in section 2.2.2. Also, I analyzed the PNCs by coating them with a polymer-matrix to avoid the moisture effect. For polymer/glass interface, 5 mg of PMMA was dissolved in 1 mL toluene, and 10 µL of this PMMA solution was added to the suspension of $MAPbI_3$ PNCs. This solution was drop-cast on a glass coverslip and observed under the microscope. The PL intensity trajectories of single $MAPbI_3$ PNCs were recorded similarly by photoexciting the sample with 532 nm cw laser. The typical PL intensity trajectories of single PNCs at argon/glass and polymer/glass interface are shown in Figure 3.5a-d(i), respectively. From the occurrences of the PL intensity [Figure 3.5 a-d(ii)], the blinking behavior with distinct ON- and OFF-event is apparent. The occurrence of ON-events was more than that of the OFF-events because the excitation intensity was high (875 W cm^{-2}). Tian *et al.* reported that with the increase in excitation intensity, the OFF-events decrease because the efficiency of active quenchers in trapping a large number of charges decreases. In other words, the emission of the PNC increases at high-intensity excitation.[43,44] Nevertheless, at high-excitation intensity, the PNC degrades fast under air atmosphere. In contrast, the PL stabilizes under argon and polymer atmosphere. The stability in argon and polymer environment supports the ensemble PL results, suggesting that the perovskite oxidation and the superoxide generation and perovskite oxidation can be suppressed by avoiding oxygen and moisture.

To understand whether oxygen or moisture is responsible for the degradation of PNCs, I analyzed the single-particle PL intensity trajectories after saturating a single-particle sample chamber with dry air. I dried the air by sequentially passing through the columns filled with sodium hydroxide, molecular sieves (5 Å), and granular silica gel. The PNCs were drop-cast on a glass coverslip covered with a silicon chamber, and the dry air was passed inside the chamber. The PNCs in dry air were observed under an EMCCD, and the PL intensity trajectories were recorded (Figure 3.6). Even after eliminating the moisture, PNCs in dry air showed photobleaching and PL blinking. Thus, I assume oxygen itself generates superoxide and oxidizes the PNCs, which leads to the degradation of PNCs. Nonetheless, the role of moisture alone is not examined by considering several reports about degradation of halide perovskites in humid atmospheres.

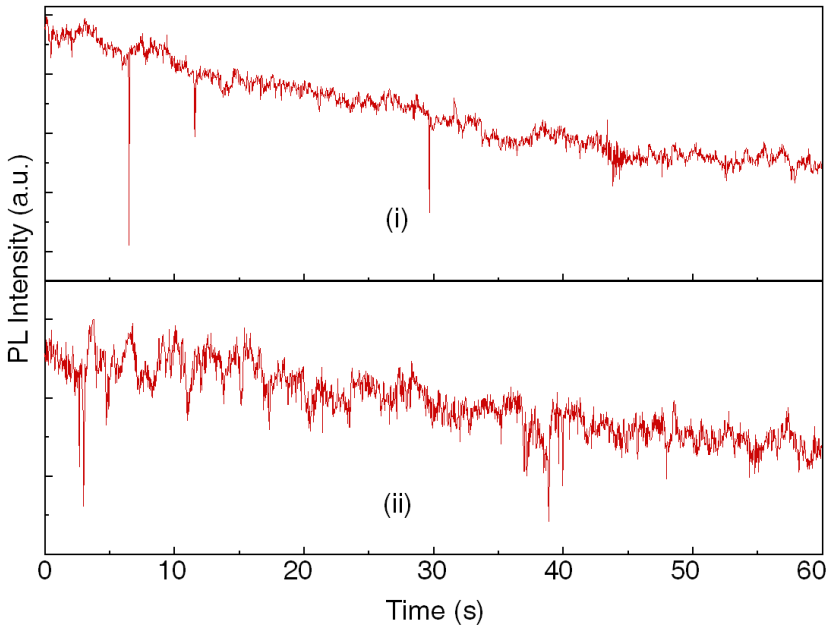

Figure 3.6. Typical single-particle PL intensity trajectories of $MAPbI_3$ PNCs in dry air. The PNCs were excited with a 532 nm cw laser.

However, the blinking was independent of the atmosphere. To determine the changes in ON-and OFF-event occurrences according to the local atmosphere, I analyzed the distribution of ON- and OFF-times in >100 single $MAPbI_3$ PNCs each at air/glass, argon/glass, and polymer/glass interface shown in Figures 3.7a-c, respectively. For this

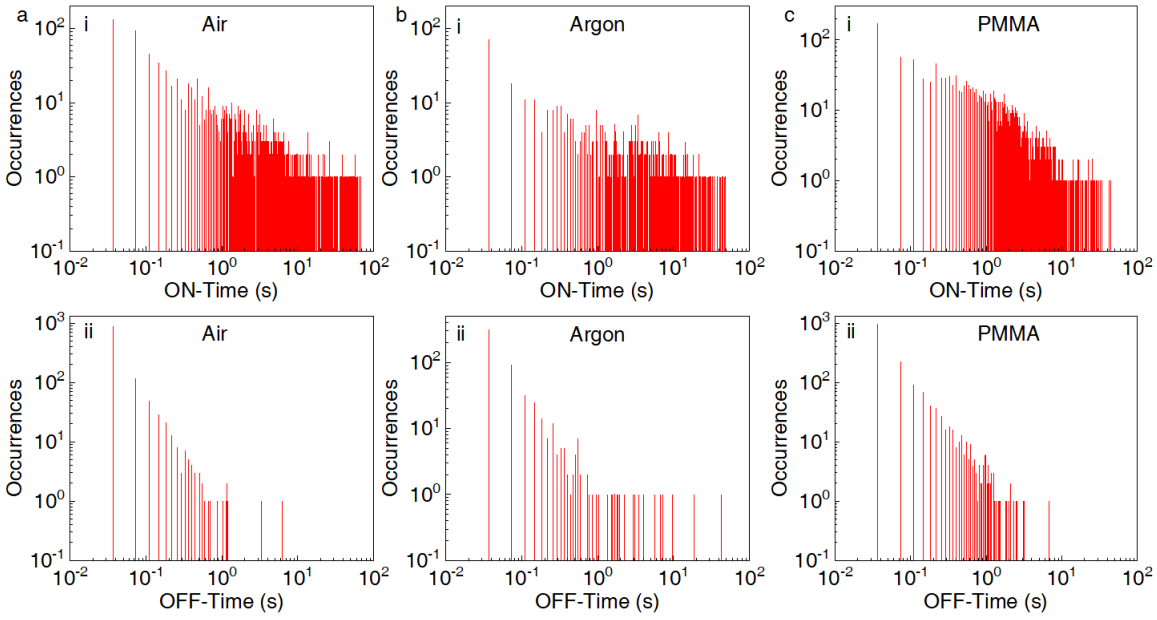

Figure 3.7. (i) ON and (ii) OFF time histogram of >300 single $MAPbI_3$ PNCs at (a) air/glass interface, (b) argon/glass interface, and (c) polymerized PNCs.

analysis, I estimated the PL intensity threshold, where it turns ON from the OFF-event in each PL intensity trajectory. For example, in Figure 3.5, the blue dashed line represents the threshold point in the corresponding PL intensity trajectories under argon and polymer atmosphere. In the case of air atmosphere, PL intensity was continuously decreasing. So, for estimating the threshold, baseline correction was carried out for each PL intensity trajectory. I also analyzed the variation in the average OFF-intensities in air/glass, argon/glass, and polymer matrix, as shown in Figure 3.8. From Figures 3.7 and 3.8, I observed that the number of ON-events was more than that of the OFF-events in all the cases, suggesting the number of emitting sites and quenchers are almost equal at air/glass, argon/glass, and polymer matrix. In a PNC, the quenchers can form from halide or cation-assisted traps. As the quenchers act as the nonradiative recombination centers, I assume that those trap centers will become inactive under argon and the polymer environment. Therefore, argon and polymer atmosphere aids in reducing the traps.

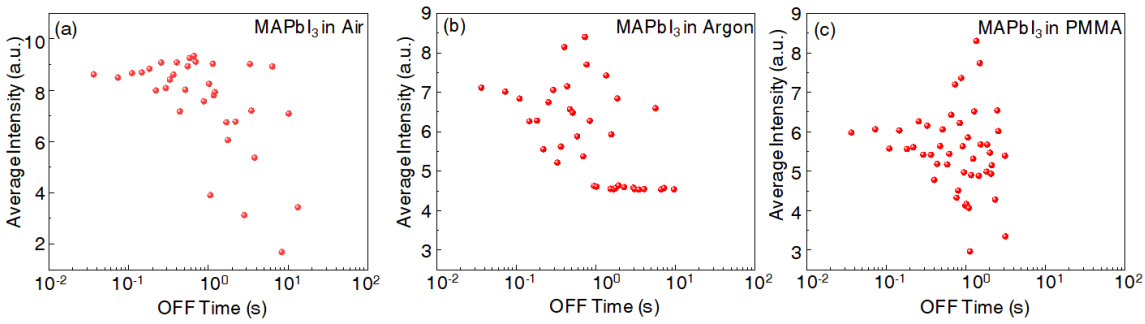

Figure 3.8. Variation of average PL intensity with its OFF-time in >300 single $MAPbI_3$ PNCs at (a) air/glass interface, (b) argon/glass interface, and (c) in polymerized PNCs.

3.2.4 The Mechanism of Photodegradation

Although $MAPbI_3$ PNCs at air/glass interface showed a gradual decrease in PL intensity during an ON-event, some PL intensity trajectories of $MAPbI_3$ PNCs at air/glass interface also showed a long-OFF-event. Figure 3.9 shows the typical examples of such PL intensity trajectories with long-OFF events. In these PL intensity trajectories, when the particle was in the OFF-state, the PL intensity before and after turning OFF was at the same level, as shown by the dashed line in Figure 3.9. Such PL intensity trajectories lead to the understanding of the role of oxygen reactivity towards PNCs. It shows that under an OFF-

event, when the PNC is in the ionized excited state, the photodegradation does not occur, and the PNC does not react with the superoxide. In general, PL blinking in PNCs occurs from the surface trap states, charging-discharging of the trap states, photoinduced defects, and fast nonradiative Auger relaxation.[43–50] On the other hand, oxidation of PNC leads to the superoxide generation by electron transfer from PNC to molecular oxygen during photoexcitation.[23,25,27–29,51,52] Furthermore, electron transfer from one state to another is the main reason for both the blinking and the oxidation. Therefore, based on the above statements, I am considering four different states involved in the blinking, oxidation, and

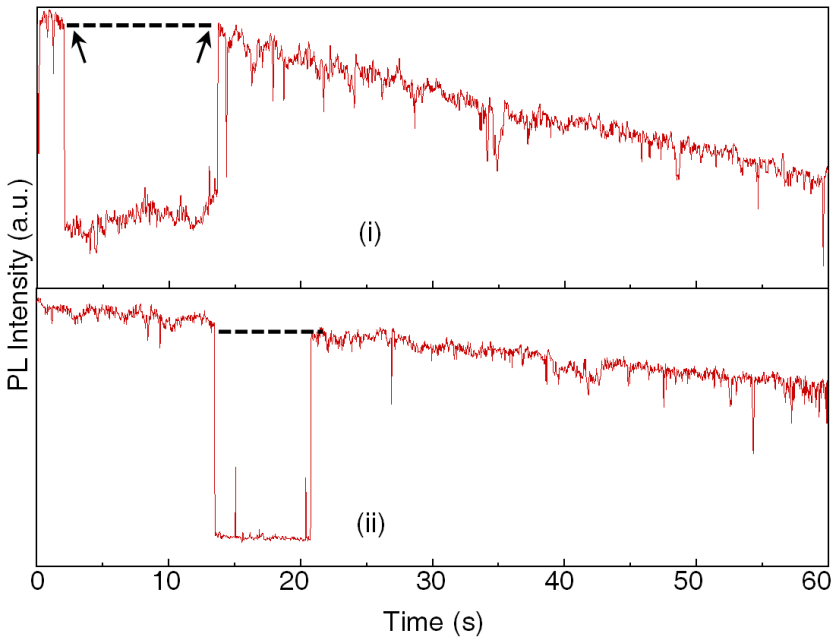

Figure 3.9. Typical PL intensity trajectories of $MAPbI_3$ PNCs saturated by air photoexcited by a 532 nm cw laser having long OFF-events.

degradation of PNC. These states are (i) ground, (ii) excited, (iii) neutral, and (iv) ionized states. The ON-state includes ground, neutral, and excited states, whereas OFF-state includes ground and excited ionized states. The oxidation of PNC by photoinduced electron transfer to molecular oxygen is a dark reaction. Thus, the above states can be affected by the superoxide generation and the oxidation of PNC. But in Figure 3.9, the complete recovery of the PL intensity after a long-OFF event in the PNC suggests that the ionized PNC does not generate superoxide during an OFF-state when the charge carriers nonradiatively recombine. So, under the OFF-event nonradiative recombination dominates the electron transfer to oxygen. Therefore, the oxidation of PNCs stops, and the superoxide doesn't generate and react with the PNC.

Generally, in blinking, the nonradiative recombination represents the OFF-state. In the case of halide perovskite, oxidation of PNC and the generation of superoxide is a dark state. Therefore, superoxide generation is high when the electron transfer rate is more than that of the nonradiative recombination rate. However, recovery of PL intensity during OFF-event suggests that the ionization of PNCs prevents it from oxidation and its reaction towards superoxide. In other words, the rate of nonradiative recombination is higher than that of the electron transfer to oxygen. To prove this, I recorded the PL decay profiles of $MAPbI_3$ PNCs at low- and high-excitation intensities under air and argon environment (Figure 3.10). I fitted the PL decays using the third exponential equation (Chapter 2, eq. 2.1) and estimated the average PL lifetime through the intensity averaged equation (Chapter

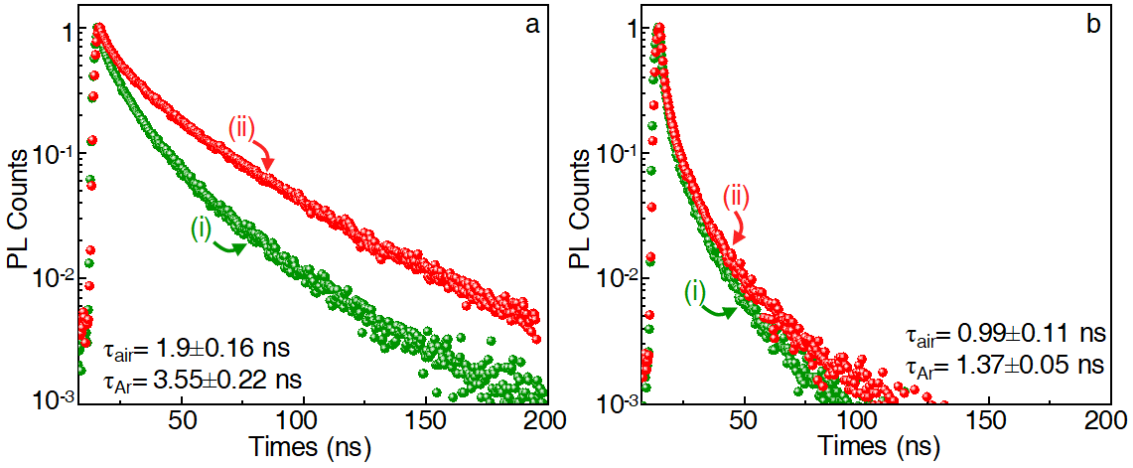

Figure 3.10. PL decay profiles of $MAPbI_3$ PNC films at (i) air/glass, and (ii) argon/glass interfaces under (a) low-excitation intensity (0.007 W cm^{-2}), and (b) high-excitation intensity (1.4 W cm^{-2}) of a 400 nm fs laser.

2, eq. 2.3). The average PL lifetime of $MAPbI_3$ PNC under a low-intensity excitation in air was 1.9±0.16 ns, which was lower than that of argon atmosphere, 3.55±0.22 ns. Similarly, under a high-excitation intensity, the average PL lifetime of $MAPbI_3$ PNCs in air atmosphere (0.99±0.11 ns) was lower than in argon atmosphere (1.37±0.05 ns). Irrespective of laser excitation intensity, the low PL lifetime values in air atmosphere suggest that electron transfer to oxygen plays a significant role in quenching the emissive states. From the average PL lifetimes in the four cases, I calculated the approximate rate of electron transfer and the nonradiative recombination. At low-excitation intensity, the PL lifetime of $MAPbI_3$ PNC is

$$\tau_1 = \frac{1}{k_r + k_{nr} + k_{et}} \quad (3.1)$$

Here, τ_1 is 1.9±0.16 ns, k_r is the rate of radiative relaxation, k_{nr} is the rate of nonradiative relaxation, and k_{et} is the rate of electron transfer to oxygen. When argon was introduced in the $MAPbI_3$ PNC atmosphere, the reactivity of oxygen towards PNC stopped. So, I ruled out the electron transfer to oxygen when PNCs were in argon atmosphere, and the PL lifetime of $MAPbI_3$ PNC at low excitation in argon atmosphere became

$$\tau_2 = \frac{1}{k_r + k_{nr}} \quad (3.2)$$

Here, τ_2 is 3.55±0.22 ns. By solving equations 3.1 and 3.2, I estimated the rate of electron transfer from $MAPbI_3$ PNC to oxygen at 2.45×10^8 s^{-1}.

For calculating the fast nonradiative recombination, the PL lifetime of $MAPbI_3$ PNC at high-excitation intensity is considered as

$$\tau_3 = \frac{1}{k_r + k_{nr} + k_A + k_{et}} \quad (3.3)$$

Here, τ_3 is 0.99±0.11 ns, and k_A is the additional rate of nonradiative relaxation.

By solving equation 3.3 from equations 3.1 and 3.2, I estimated the additional rate of nonradiative relaxation in $MAPbI_3$ PNC at 4.84×10^8 s^{-1}. Similar to PL lifetime at low excitation intensity, I ruled out the electron transfer at a high-excitation intensity under argon atmosphere, and the PL lifetime at this condition is

$$\tau_4 = \frac{1}{k_r + k_{nr} + k_A} \quad (3.4)$$

Here, τ_4 is 1.37±0.05 ns. By solving equations 3.1 to 3.4, I confirmed the rate of additional nonradiative relaxation ($k_A = 4.54\times10^8$ s^{-1}). Thus, I proved that the $k_{et} < k_A$ at high-excitation intensity.

The mechanism of PL blinking and photodegradation of $MAPbI_3$ PNCs are shown in Figure 3.11. This mechanism takes into account the four electronic states for the electron transfer, radiative, and nonradiative relaxation pathways. The first is the ground state of the perovskite, which corresponds to its valence band maximum. The second is the excited state corresponding to the conduction band of the perovskite, which lies at higher energy. The third corresponds to neutral states. The neutral ground, and excited states are included

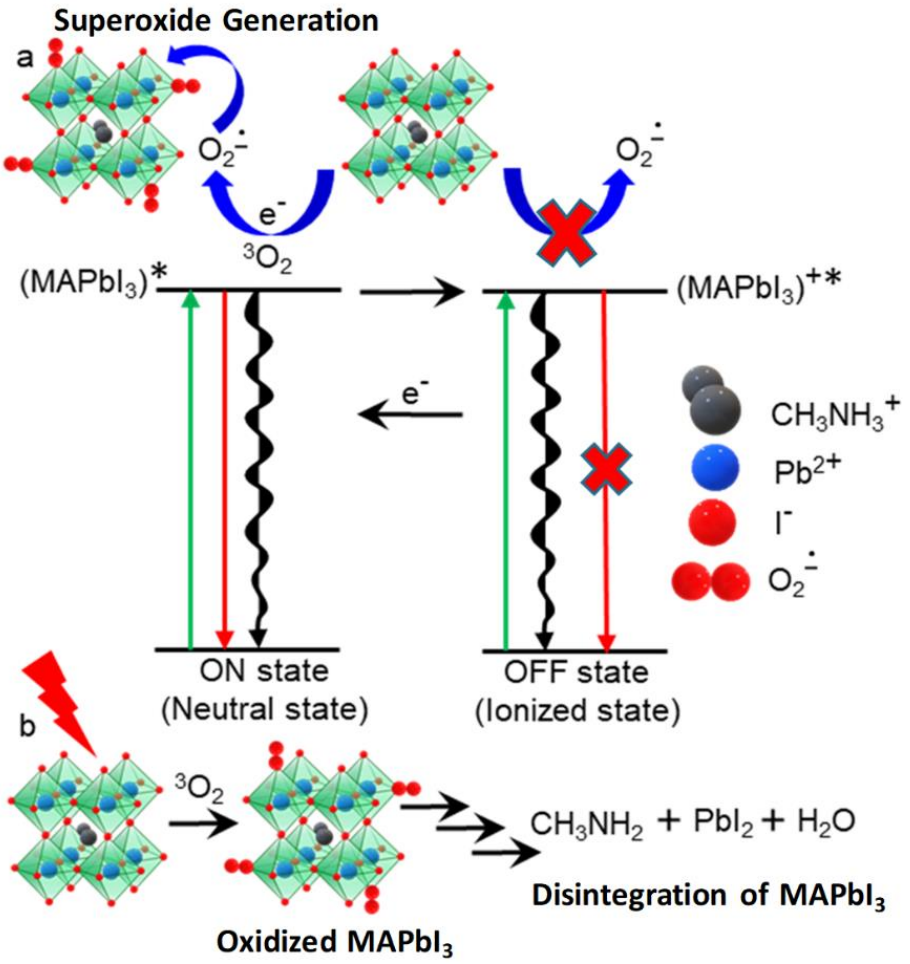

Figure 3.11. (a) Scheme of the electron transfer mechanism, the generation of superoxide by oxidizing $MAPbI_3$ PNCs, and all four electronic states. (b) The disintegration of $MAPbI_3$ PNCs by superoxide.

for determining the ON-state. The fourth is the ionized state corresponding to the electron and hole trap states. The ground, excited, and ionized states are included for determining the OFF-state. Under the ON-state, the electron will radiatively recombine, represented by the red arrow in Figure 3.11. Conversely, the electron will nonradiatively recombine from the excited state if it transfers to the molecular oxygen or the ionized state, represented by the curvy black arrow in Figure 3.11. According to Tian *et al*., the inhomogenous blinking in the PNC occurs by the photoactivation and deactivation of the quenching and emitting sites, which corresponds to the chemical and structural defects of the PNC.[43] Further, Aristidou *et al*. reported the structural defects such as the halide vacancies are responsible for the photogenerated superoxide, which diffuses into the $MAPbI_3$ PNCs, deprotonates the methylammonium cation, and subsequently deteriorates the perovskite geometry into CH_3NH_2, PbI_2, and H_2O as shown in Figure 3.11b. By referring to the literature, I

hypothesize that when the perovskite is in its excited state, the electron transfers from PNC to oxygen and oxidizes the PNC. The electron transfer competes with the other recombination pathways when the PNC is in a neutral state. After the electron transfer to oxygen, the superoxide generates at the halide vacancies in the PNCs.

On the other hand, when the PNC gets ionized, it prevents electron transfer to oxygen. As shown in Fig. 3.9, the similar level of PL intensity before and after a long-living OFF-state represents no degradation of the PNC, which means the PNC doesn't react to oxygen in an ionized state. Furthermore, the rate of nonradiative recombination in the ionized state overcomes the rate of electron transfer, which also supports the calculated rates obtained from the average PL lifetimes. Thus, the suppression of superoxide generation provides stability in the PNCs. These results in aerobic and anaerobic conditions and the rates of electron transfer and nonradiative recombination suggest that under a neutral state, the $MAPbI_3$ PNCs will continuously degrade due to the generation of superoxide.

3.3 Conclusion

This chapter has demonstrated the relation between photoluminescence blinking and oxidation of $MAPbI_3$ perovskite nanocrystals. I examined the photoluminescence behavior at the ensemble and single-particle levels in different environmental conditions- air, argon, polymer, and dry air. I confirmed the continuous decrease of photoluminescence in $MAPbI_3$ perovskite nanocrystals by the oxidation of perovskite and superoxide generation when interacted with oxygen and light. The photoluminescence intensity trajectories of single-particle showed that the photodegradation was suppressed in argon and polymer atmosphere. The photoluminescence intensity trajectories with long-OFF events and the recovery of photoluminescence intensity suggested that ionized excited state prevents the electron transfer from perovskite nanocrystal to oxygen, the oxidation of perovskite nanocrystals, and the superoxide generation. Thus, during an ON-state, the $MAPbI_3$ perovskite nanocrystals continuously generate superoxide, and the photoluminescence decreases gradually over time. Furthermore, by calculating the average photoluminescence lifetimes of perovskite nanocrystals under high and low excitation intensity in air and argon atmosphere, I estimated that the rate of electron transfer to oxygen (2.45×10^8 s^{-1}) is lower than that of the nonradiative relaxation (4.84×10^8 s^{-1}) during an OFF-state. Therefore, suppressing the electron transfer to oxygen and the superoxide generation will increase the photoluminescence of perovskite nanocrystals.

3.4 References

(1) Kojima, A.; Teshima, K.; Shirai, Y.; Miyasaka, T. Organometal Halide Perovskites as Visible-Light Sensitizers for Photovoltaic Cells. *J. Am. Chem. Soc.* **2009**, *131*, 6050–6051.

(2) Deschler, F.; Price, M.; Pathak, S.; Klintberg, L. E.; Jarausch, D. D.; Higler, R.; Hüttner, S.; Leijtens, T.; Stranks, S. D.; Snaith, H. J.; Atatüre, M.; Phillips, R. T.; Friend, R. H. High Photoluminescence Efficiency and Optically Pumped Lasing in Solution-Processed Mixed Halide Perovskite Semiconductors. *J. Phys. Chem. Lett.* **2014**, *5*, 1421–1426.

(3) Al-Ashouri, A.; Köhnen, E.; Li, B.; Magomedov, A.; Hempel, H.; Caprioglio, P.; Márquez, J. A.; Morales Vilches, A. B.; Kasparavicius, E.; Smith, J. A.; Phung, N.; Menzel, D.; Grischek, M.; Kegelmann, L.; Skroblin, D.; Gollwitzer, C.; Malinauskas, T.; Jošt, M.; Matič, G.; Rech, B.; Schlatmann, R.; Topič, M.; Korte, L.; *et al.* Monolithic Perovskite/Silicon Tandem Solar Cell with >29% Efficiency by Enhanced Hole Extraction. *Science* **2020**, *370*, 1300–1309.

(4) Hassan, Y.; Ashton, O. J.; Park, J. H.; Li, G.; Sakai, N.; Wenger, B.; Haghighirad, A. A.; Noel, N. K.; Song, M. H.; Lee, B. R.; Friend, R. H.; Snaith, H. J. Facile Synthesis of Stable and Highly Luminescent Methylammonium Lead Halide Nanocrystals for Efficient Light Emitting Devices. *J. Am. Chem. Soc.* **2019**, *141*, 1269–1279.

(5) Weng, G.; Xue, J.; Tian, J.; Hu, X.; Bao, X.; Lin, H.; Chen, S.; Zhu, Z.; Chu, J. Picosecond Random Lasing Based on Three-Photon Absorption in Organometallic Halide $CH_3NH_3PbBr_3$ Perovskite Thin Films. *ACS Photonics* **2018**, *5*, 2951–2959.

(6) Daus, A.; Roldán-Carmona, C.; Domanski, K.; Knobelspies, S.; Cantarella, G.; Vogt, C.; Grätzel, M.; Nazeeruddin, M. K.; Tröster, G. Metal-Halide Perovskites for Gate Dielectrics in Field-Effect Transistors and Photodetectors Enabled by PMMA Lift-Off Process. *Adv. Mater.* **2018**, *30*, 1707412.

(7) Shi, D.; Adinolfi, V.; Comin, R.; Yuan, M.; Alarousu, E.; Buin, A.; Chen, Y.; Hoogland, S.; Rothenberger, A.; Katsiev, K.; Losovyj, Y.; Zhang, X.; Dowben, P. A.; Mohammed, O. F.; Sargent, E. H.; Bakr, O. M. Low Trap-State Density and Long Carrier Diffusion in Organolead Trihalide Perovskite Single Crystals. *Science*

2015, *347*, 519–522.

(8) Dong, Q.; Fang, Y.; Shao, Y.; Mulligan, P.; Qiu, J.; Cao, L.; Huang, J. Electron-Hole Diffusion Lengths >175 μm in Solution-Grown $CH_3NH_3PbI_3$ Single Crystals. *Science* **2015**, *347*, 967–970.

(9) Song, J.; Li, J.; Li, X.; Xu, L.; Dong, Y.; Zeng, H. Quantum Dot Light-Emitting Diodes Based on Inorganic Perovskite Cesium Lead Halides ($CsPbX_3$). *Adv. Mater.* **2015**, *27*, 7162–7167.

(10) Jia, Y.; Kerner, R. A.; Grede, A. J.; Rand, B. P.; Giebink, N. C. Continuous-Wave Lasing in an Organic-Inorganic Lead Halide Perovskite Semiconductor. *Nat. Photonics* **2017**, *11*, 784–788.

(11) Wang, H.; Kim, D. H. Perovskite-Based Photodetectors: Materials and Devices. *Chem. Soc. Rev.* **2017**, *46*, 5204–5236.

(12) Chung, H.; Jung, S. Il; Kim, H. J.; Cha, W.; Sim, E.; Kim, D.; Koh, W.-K.; Kim, J. Composition-Dependent Hot Carrier Relaxation Dynamics in Cesium Lead Halide ($CsPbX_3$, X=Br and I) Perovskite Nanocrystals. *Angew. Chem. Int. Ed.* **2017**, *56*, 4160–4164.

(13) Yuyama, K.; Islam, M. J.; Takahashi, K.; Nakamura, T.; Biju, V. Crystallization of Methylammonium Lead Halide Perovskites by Optical Trapping. *Angew. Chem. Int. Ed.* **2018**, *57*, 13424–13428.

(14) Saidaminov, M. I.; Abdelhady, A. L.; Murali, B.; Alarousu, E.; Burlakov, V. M.; Peng, W.; Dursun, I.; Wang, L.; He, Y.; MacUlan, G.; Goriely, A.; Wu, T.; Mohammed, O. F.; Bakr, O. M. High-Quality Bulk Hybrid Perovskite Single Crystals within Minutes by Inverse Temperature Crystallization. *Nat. Commun.* **2015**, *6*, 7586.

(15) Tan, Z.-K.; Moghaddam, R. S.; Lai, M. L.; Docampo, P.; Higler, R.; Deschler, F.; Price, M.; Sadhanala, A.; Pazos, L. M.; Credgington, D.; Hanusch, F.; Bein, T.; Snaith, H. J.; Friend, R. H. Bright Light-Emitting Diodes Based on Organometal Halide Perovskite. *Nat. Nanotechnol.* **2014**, *9*, 687–692.

(16) Chiba, T.; Hayashi, Y.; Ebe, H.; Hoshi, K.; Sato, J.; Sato, S.; Pu, Y.-J.; Ohisa, S.; Kido, J. Anion-Exchange Red Perovskite Quantum Dots with Ammonium Iodine

Salts for Highly Efficient Light-Emitting Devices. *Nat. Photonics* **2018**, *12*, 681–687.

(17) National Renewable Energy Laboratory, Best Research-Cell Efficiency Chart; *www.nrel.gov/pv/cell-efficiency.html*.

(18) Jin, H.; Debroye, E.; Keshavarz, M.; Scheblykin, I. G.; Roeffaers, M. B. J.; Hofkens, J.; Steele, J. A. It's a Trap! On the Nature of Localised States and Charge Trapping in Lead Halide Perovskites. *Mater. Horizons* **2020**, *7*, 397–410.

(19) Gerhard, M.; Louis, B.; Camacho, R.; Merdasa, A.; Li, J.; Kiligaridis, A.; Dobrovolsky, A.; Hofkens, J.; Scheblykin, I. G. Microscopic Insight into Non-Radiative Decay in Perovskite Semiconductors from Temperature-Dependent Luminescence Blinking. *Nat. Commun.* **2019**, *10*, 1698.

(20) Meggiolaro, D.; Motti, S. G.; Mosconi, E.; Barker, A. J.; Ball, J.; Andrea Riccardo Perini, C.; Deschler, F.; Petrozza, A.; De Angelis, F. Iodine Chemistry Determines the Defect Tolerance of Lead-Halide Perovskites. *Energy Environ. Sci.* **2018**, *11*, 702–713.

(21) Milot, R. L.; Eperon, G. E.; Snaith, H. J.; Johnston, M. B.; Herz, L. M. Temperature-Dependent Charge-Carrier Dynamics in $CH_3NH_3PbI_3$ Perovskite Thin Films. *Adv. Funct. Mater.* **2015**, *25*, 6218–6227.

(22) Wang, L.; Wang, K.; Zou, B. Pressure-Induced Structural and Optical Properties of Organometal Halide Perovskite-Based Formamidinium Lead Bromide. *J. Phys. Chem. Lett.* **2016**, *7*, 2556–2562.

(23) Aristidou, N.; Sanchez-Molina, I.; Chotchuangchutchaval, T.; Brown, M.; Martinez, L.; Rath, T.; Haque, S. A. The Role of Oxygen in the Degradation of Methylammonium Lead Trihalide Perovskite Photoactive Layers. *Angew. Chem.* **2015**, *127*, 8326–8330.

(24) Ghimire, S.; Takahashi, K.; Takano, Y.; Nakamura, T.; Biju, V. Photon Recycling by Energy Transfer in Piezochemically Synthesized and Close-Packed Methylammonium Lead Halide Perovskites. *J. Phys. Chem. C* **2019**, *123*, 27752–27758.

(25) Aristidou, N.; Eames, C.; Sanchez-Molina, I.; Bu, X.; Kosco, J.; Islam, M. S.; Haque,

S. A. Fast Oxygen Diffusion and Iodide Defects Mediate Oxygen-Induced Degradation of Perovskite Solar Cells. *Nat. Commun.* **2017**, *8*, 15218.

(26) Li, Y.; Xu, X.; Wang, C.; Wang, C.; Xie, F.; Yang, J.; Gao, Y. Degradation by Exposure of Coevaporated $CH_3NH_3PbI_3$ Thin Films. *J. Phys. Chem. C* **2015**, *119*, 23996–24002.

(27) Bryant, D.; Aristidou, N.; Pont, S.; Sanchez-Molina, I.; Chotchunangatchaval, T.; Wheeler, S.; Durrant, J. R.; Haque, S. A. Light and Oxygen Induced Degradation Limits the Operational Stability of Methylammonium Lead Triiodide Perovskite Solar Cells. *Energy Environ. Sci.* **2016**, *9*, 1655–1660.

(28) Zhang, L.; Sit, P. H. L. Ab Initio Study of the Role of Oxygen and Excess Electrons in the Degradation of $CH_3NH_3PbI_3$. *J. Mater. Chem. A* **2017**, *5*, 9042–9049.

(29) Tang, X.; Brandl, M.; May, B.; Levchuk, I.; Hou, Y.; Richter, M.; Chen, H.; Chen, S.; Kahmann, S.; Osvet, A.; Maier, F.; Steinrück, H. P.; Hock, R.; Matt, G. J.; Brabec, C. J. Photoinduced Degradation of Methylammonium Lead Triiodide Perovskite Semiconductors. *J. Mater. Chem. A* **2016**, *4*, 15896–15903.

(30) Boyd, C. C.; Cheacharoen, R.; Leijtens, T.; McGehee, M. D. Understanding Degradation Mechanisms and Improving Stability of Perovskite Photovoltaics. *Chem. Rev.* **2019**, *119*, 3418–3451.

(31) Brenes, R.; Eames, C.; Bulović, V.; Islam, M. S.; Stranks, S. D. The Impact of Atmosphere on the Local Luminescence Properties of Metal Halide Perovskite Grains. *Adv. Mater.* **2018**, *30*, 1706208.

(32) Krishna, A.; Akhavan Kazemi, M. A.; Sliwa, M.; Reddy, G. N. M.; Delevoye, L.; Lafon, O.; Felten, A.; Do, M. T.; Gottis, S.; Sauvage, F. Defect Passivation *via* the Incorporation of Tetrapropylammonium Cation Leading to Stability Enhancement in Lead Halide Perovskite. *Adv. Funct. Mater.* **2020**, *30*, 1909737.

(33) Akhavan Kazemi, M. A.; Raval, P.; Cherednichekno, K.; Chotard, J.; Krishna, A.; Demortiere, A.; Reddy, G. N. M.; Sauvage, F. Molecular-Level Insight into Correlation between Surface Defects and Stability of Methylammonium Lead Halide Perovskite Under Controlled Humidity. *Small Methods* **2020**, 2000834.

(34) Müller, C.; Glaser, T.; Plogmeyer, M.; Sendner, M.; Döring, S.; Bakulin, A. A.;

Brzuska, C.; Scheer, R.; Pshenichnikov, M. S.; Kowalsky, W.; Pucci, A.; Lovrinčić, R. Water Infiltration in Methylammonium Lead Iodide Perovskite: Fast and Inconspicuous. *Chem. Mater.* **2015**, *27*, 7835–7841.

(35) He, J.; Fang, W.-H.; Long, R.; Prezhdo, O. V. Why Oxygen Increases Carrier Lifetimes but Accelerates Degradation of $CH_3NH_3PbI_3$ under Light Irradiation: Time-Domain Ab Initio Analysis. *J. Am. Chem. Soc.* **2020**, *142*, 14664–14673.

(36) Kong, W.; Rahimi-Iman, A.; Bi, G.; Dai, X.; Wu, H. Oxygen Intercalation Induced by Photocatalysis on the Surface of Hybrid Lead Halide Perovskites. *J. Phys. Chem. C* **2016**, *120*, 7606–7611.

(37) Péan, E. V.; De Castro, C. S.; Dimitrov, S.; De Rossi, F.; Meroni, S.; Baker, J.; Watson, T.; Davies, M. L. Investigating the Superoxide Formation and Stability in Mesoporous Carbon Perovskite Solar Cells with an Aminovaleric Acid Additive. *Adv. Funct. Mater.* **2020**, *30*, 1909839.

(38) Feng, X.; Su, H.; Wu, Y.; Wu, H.; Xie, J.; Liu, X.; Fan, J.; Dai, J.; He, Z. Photon-Generated Carriers Excite Superoxide Species Inducing Long-Term Photoluminescence Enhancement of $MAPbI_3$ Perovskite Single Crystals. *J. Mater. Chem. A* **2017**, *5*, 12048–12053.

(39) Tian, Y.; Peter, M.; Unger, E.; Abdellah, M.; Zheng, K.; Pullerits, T.; Yartsev, A.; Sundström, V.; Scheblykin, I. G. Mechanistic Insights into Perovskite Photoluminescence Enhancement: Light Curing with Oxygen Can Boost Yield Thousandfold. *Phys. Chem. Chem. Phys.* **2015**, *17*, 24978–24987.

(40) Tian, Y.; Merdasa, A.; Unger, E.; Abdellah, M.; Zheng, K.; Mckibbin, S.; Mikkelsen, A.; Pullerits, T.; Yartsev, A.; Sundström, V.; Scheblykin, I. G. Enhanced Organo-Metal Halide Perovskite Photoluminescence from Nanosized Defect-Free Crystallites and Emitting Sites. *J. Phys. Chem. Lett.* **2015**, *6*, 4171–4177.

(41) Wang, L.; Williams, N. E.; Malachosky, E. W.; Otto, J. P.; Hayes, D.; Wood, R. E.; Guyot-Sionnest, P.; Engel, G. S. Scalable Ligand-Mediated Transport Synthesis of Organic-Inorganic Hybrid Perovskite Nanocrystals with Resolved Electronic Structure and Ultrafast Dynamics. *ACS Nano* **2017**, *11*, 2689–2696.

(42) Hong, D.; Zhou, Y.; Wan, S.; Hu, X.; Xie, D.; Tian, Y. Nature of Photoinduced

Quenching Traps in Methylammonium Lead Triiodide Perovskite Revealed by Reversible Photoluminescence Decline. *ACS Photonics* **2018**, *5*, 2034–2043.

(43) Tian, Y.; Merdasa, A.; Peter, M.; Abdellah, M.; Zheng, K.; Ponseca, C. S.; Pullerits, T.; Yartsev, A.; Sundström, V.; Scheblykin, I. G. Giant Photoluminescence Blinking of Perovskite Nanocrystals Reveals Single-Trap Control of Luminescence. *Nano Lett.* **2015**, *15*, 1603–1608.

(44) Yuan, G.; Ritchie, C.; Ritter, M.; Murphy, S.; Gómez, D. E.; Mulvaney, P. The Degradation and Blinking of Single $CsPbI_3$ Perovskite Quantum Dots. *J. Phys. Chem. C* **2018**, *122*, 13407–13415.

(45) Merdasa, A.; Tian, Y.; Camacho, R.; Dobrovolsky, A.; Debroye, E.; Unger, E. L.; Hofkens, J.; Sundström, V.; Scheblykin, I. G. "Supertrap" at Work: Extremely Efficient Nonradiative Recombination Channels in $MAPbI_3$ Perovskites Revealed by Luminescence Super-Resolution Imaging and Spectroscopy. *ACS Nano* **2017**, *11*, 5391–5404.

(46) Yuan, H.; Debroye, E.; Caliandro, G.; Janssen, K. P. F.; Van Loon, J.; Kirschhock, C. E. A.; Martens, J. A.; Hofkens, J.; Roeffaers, M. B. J. Photoluminescence Blinking of Single-Crystal Methylammonium Lead Iodide Perovskite Nanorods Induced by Surface Traps. *ACS Omega* **2016**, *1*, 148–159.

(47) Thomas, E. M.; Ghimire, S.; Kohara, R.; Anil, A. N.; Yuyama, K.; Takano, Y.; Thomas, K. G.; Biju, V. Blinking Suppression in Highly Excited CdSe/ZnS Quantum Dots by Electron Transfer under Large Positive Gibbs (Free) Energy Change. *ACS Nano* **2018**, *12*, 9060–9069.

(48) Ghimire, S.; Biju, V. Relations of Exciton Dynamics in Quantum Dots to Photoluminescence, Lasing, and Energy Harvesting. *J. Photochem. Photobiol. C Photochem. Rev.* **2018**, *34*, 137–151.

(49) Wu, K.; Lim, J.; Klimov, V. I. Superposition Principle in Auger Recombination of Charged and Neutral Multicarrier States in Semiconductor Quantum Dots. *ACS Nano* **2017**, *11*, 8437–8447.

(50) Park, Y.-S.; Bae, W. K.; Pietryga, J. M.; Klimov, V. I. Auger Recombination of Biexcitons and Negative and Positive Trions in Individual Quantum Dots. *ACS Nano*

2014, *8*, 7288–7296.

(51) Gottesman, R.; Gouda, L.; Kalanoor, B. S.; Haltzi, E.; Tirosh, S.; Rosh-Hodesh, E.; Tischler, Y.; Zaban, A.; Quarti, C.; Mosconi, E.; De Angelis, F. Photoinduced Reversible Structural Transformations in Free-Standing $CH_3NH_3PbI_3$ Perovskite Films. *J. Phys. Chem. Lett.* **2015**, *6*, 2332–2338.

(52) Quitsch, W. A.; Dequilettes, D. W.; Pfingsten, O.; Schmitz, A.; Ognjanovic, S.; Jariwala, S.; Koch, S.; Winterer, M.; Ginger, D. S.; Bacher, G. The Role of Excitation Energy in Photobrightening and Photodegradation of Halide Perovskite Thin Films. *J. Phys. Chem. Lett.* **2018**, *9*, 2062–2069.

Chapter 4

Photoluminescence Blinking Suppression by Halide Vacancy Filling

Abstract

Halide perovskites are promising semiconductor materials for next-generation optical and electronic devices. However, the long-term durability and stability against the environment, such as moisture, oxygen, and light, cause adverse effects. The ionic and electronic defects generated by intrinsic or extrinsic factors disintegrate the perovskite structure and deteriorate the photoluminescence properties. One such defects are the halide vacancies, which form deep traps in the energy levels, and the leading cause for the nonradiative recombination or trapping of photo- or electro-generated charge carriers, causing undesired stochastic fluctuations of luminescence in perovskite nanocrystals and quantum dots, called blinking. This chapter demonstrates the suppressions of photoluminescence blinking and fast nonradiative recombination of the excitons by the real-time filling of halide vacancies in $MAPbBr_3$ and $MAPbI_3$ perovskite quantum dot with MABr and MAI, respectively. Furthermore, the post-synthetic treatment of perovskite quantum dots with halide salts helped in increasing the charge carriers' photoluminescence intensities and lifetimes. Also, I estimated the rate of halide-vacancy-assisted nonradiative recombinations at 1×10^{8} s^{-1} for $MAPbBr_3$ and 1.9×10^{9} s^{-1} for $MAPbI_3$ perovskite quantum dots. Apart from the controlled real-time experiments, I constructed the ON- and OFF- times probability distributions, which suggested the change in blinking behavior from type-A to type-B after the treatment. In other words, the charging-discharging of excitons changed to the trapping-detrapping of the trap states, confirming the filling of halide vacancies.

4.1 Introduction

Halide perovskites are the class of semiconductors having potential for real-world applications[1–5] due to their unique optical and electronic properties, such as tunable photoluminescence (PL) with high quantum yield (QY),[6–8] long lifetime,[9–11] and long diffusion length of photogenerated charge carriers.[12–14] These properties vary by size, composition, temperature, pressure, synthetic methods, and environmental factors. As discussed in chapter-3, these perovskites are susceptible to moisture, humidity, oxygen, and light.[15–18] These factors promote intrinsic defects in perovskites, such as cationic and anionic (halide) vacancies (V_{MA}, V_{Pb}, V_X), interstitial sites (MA_i, Pb_i, X_i), and antisites (MA_{Pb}, Pb_{MA}, Pb_X, X_{Pb}, X_{MA}, MA_X), which are responsible for the degradation of the structural and optical properties.[10,19,20] Most of these defects form shallow traps near the band-edge of perovskites. In contrast, halide-related defects form deep traps in the energy levels and are the centers of fast nonradiative recombinations affecting the PLQY and causing PL blinking.[16–28] Therefore, halide vacancy passivation and PL blinking suppression may overcome the obstacles in achieving stable PL and improved efficiencies of the perovskite-based applications.

The PL blinking was first identified in cadmium selenide quantum dots (QD) in 1996 by Nirmal *et al.*, where the photoionization and charge neutralization results in distinct ON- and OFF- times.[34] After that report, the mechanism of PL blinking is widely investigated in QDs and nanocrystals.[35–38] Galland *et al.* demonstrated that the PL blinking behaves in two different mechanisms in QDs, expressed as (i) type-A and (ii) type-B, where the pathways of nonradiative recombination are different.[35] Similar mechanisms are applicable in lead halide perovskites microcrystals, nanocrystals (PNCs), and PQDs.[26–29,39] In the conventional type-A blinking, the charging and discharging leads to the random switching between ON- and OFF- periods. Here, in the neutral state, perovskite undergoes radiative recombination (ON-event), and when charged as trions, Auger nonradiative recombination dominates (OFF-event), which leads to the decrease in PL intensity. On the other hand, in type-B blinking, activation and deactivation of the trap centers lead to random blinking. Conversely, the dynamics of trapping and detrapping of charge carriers are a dominant factor in type-B blinking. Fluorescence lifetime intensity distribution (FLID) and the probability distribution of ON- and OFF- times help to differentiate between these two mechanisms. Type-A and type-B simultaneously occur in the case of PQDs.[26–29] For instance, Trinh *et al.* described the blinking in formamidinium lead bromide ($FAPbBr_3$)

PQD is due to the diffusion-controlled electron transfer and Auger ionization which is causing simultaneous type-A and type-B blinking and photodegradation.[27] In another report, they verified the concurrent blinking mechanisms with FLID and ON-OFF-probability distribution under different photon collection bin time.[28] According to their result, OFF-time's probability distribution showed truncation power-law in the starting few minutes and linear power-law in the rest of the time.

Apart from FLID and probability distribution, other methods like super-resolution localization microscopy and electron microscopy help correlate structural or chemical defects and PL blinking by analyzing the nonradiative relaxation pathways.[24,30–32] The structural or chemical defects, such as ionic vacancies, can act as quenchers of emitting sites or trap the charge carrier and lead to nonradiative recombination. The rate of the quenching and trapping dramatically depends on the excitation intensity for the PL. For example, the OFF-events decrease at the high-excitation power in $MAPbI_3$ nanocrystals.[30] As explained by Agiorgousis *et al.*, in the case of $MAPbI_3$, iodine vacancies form a deep defect transition level (I^0/I^-).[10] Once the iodine vacancies are negatively charged, they act as donors, leading to the formation of the strong covalent Pb-Pb dimer and the decomposition of the structural morphology. Similarly, in $MAPbBr_3$ PNCs, bromine vacancies and interstitials form deep defect levels and are responsible for PL blinking by acting as the nonradiative recombination centers.[33] These trap centers are continuously activated and deactivated when introduced with oxygen and water from the environment and the light, which affects the rate of nonradiative recombination. Therefore, in lead halide perovskites, the surrounding atmosphere is the main criterion for determining the stability and its PL.

The relationship among the PL, surface states, and the atmosphere has been examined from the passivation of the lead halide perovskites by ligands,[40] polymers,[41] A-site cations,[42] and halide ions.[43,44] Among these, passivating halide ion defects post-synthetically has improved the PL stability in PNCs. For example, surface passivation with halide salts,[43] tetrafluoroborate salt ($NaBF_4$)[23] or Ag(I) complex[44] in PNCs, and perovskite coating with CdS QDs[45] or anhydrous silica spheres[46] showed increased PL intensity and suppressed PL blinking. Haque and coworkers used organic and inorganic halide salts and passivated the halide vacancies in $MAPbI_3$ perovskite film, and observed the suppression of superoxide generation and PL stability.[43] Another report by Samanta and coworkers showed the passivation of bromine in $CsPbBr_3$ PNCs by $NaBF_4^-$, which resulted in PL

blinking suppression and partial decrease in Auger recombination centers, hot-carrier, and band-edge carrier traps.[23] However, the correlation of halide vacancies with PL blinking and charge carrier dynamics in PQDs is yet to understand at the single-particle level.

This chapter has demonstrated the suppressions in PL blinking and fast nonradiative recombination with the increases in PL lifetime and PL intensity of $MAPbX_3$ (X=Br, I) PQDs at real-time filling of halide vacancies with MAX (X=Br, I) treatment. I performed controlled experiments for examining the PL intensity trajectories of the same PQD before and after the MAX treatment at the single-particle level. I observed the suppression of PL blinking in single $MAPbX_3$ PQDs after the treatment. I also recorded the PL quantum yields (QY) and lifetimes before and after the treatment and evaluated the nonradiative recombination rate assisted by halide vacancies in the perovskites. Along with assessing PL behavior, I analyzed ON-and OFF-probability distributions of PQDs before and after the treatment and confirmed the change in blinking behavior from type-A to type-B models.

4.2 Results and Discussion

4.2.1 Characterization of Perovskite Quantum Dots

I synthesized $MAPbBr_3$ and $MAPbI_3$ PQDs by modification of ligand-assisted reprecipitation (LARP) methods.[7] The modification of the synthesis and its purification are described in section 2.2.1. LARP method is used to obtain uniform and isolated small-sized PQDs by using long-chain organic ligands (oleic acid and hexadecene) for crystal growth. I characterized these $MAPbX_3$ PQDs by absorption spectroscopy, UV-*vis* spectroscopy and TEM. For absorbance and PL spectra, the $MAPbX_3$ PQDs were dispersed in toluene, and for TEM imaging, the $MAPbX_3$ PQDs suspended in toluene was dropped on a copper grid and dried under vacuum overnight. The $MAPbBr_3$ PQDs in this study shows broad absorption and narrow emission *ca* 530 nm with the full width at half maximum (FWHM) of ~22 nm (Figure 4.1a). The size of $MAPbBr_3$ PQDs is estimated from the TEM image (Figure 4.1b) around 10.6±1.6 nm. The size distribution of >100 $MAPbBr_3$ PQDs is shown in Figure 4.1c. Similarly, $MAPbI_3$ PQDs shows broad absorption and emission *ca* 750 nm with FWHM of ~46 nm, as shown in Figure 4.2a. The red-shift absorbance and PL of $MAPbI_3$ PQDs in comparison to $MAPbBr_3$ is due to the size of the halide ion.[39,47,48] In perovskites' valence band maxima, the contribution of halide *p*-character is more when the *p*-orbital of halogen and *s*-orbital of metal mixes. The increase in halide *p*-character (from

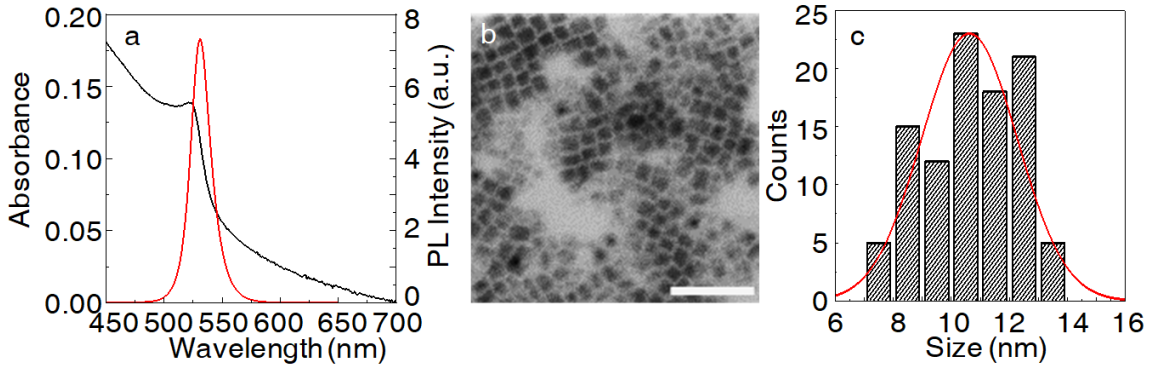

Figure 4.1. Characteristics of $MAPbBr_3$ PQDs. (a) Absorption and emission spectra of a $MAPbBr_3$ PQDs suspended in toluene. (b) TEM image (scale: 50 nm) and (c) the corresponding histogram of $MAPbBr_3$ PQD size.

Br^- to I^-) decreases the perovskite bandgap due to the rise in spin-orbit coupling. Hence, the decrease in the bandgap shifts the spectra towards the low energy region. Figure 4.2b shows the TEM image of $MAPbI_3$ PQDs, with a size of around 8.6±1.5 nm. The size distribution of >100 $MAPbI_3$ PQDs is shown in Figure 4.2c. To investigate the role of halide vacancies on PL blinking of the $MAPbX_3$ PQDs, single-particle microspectroscopy is used. The

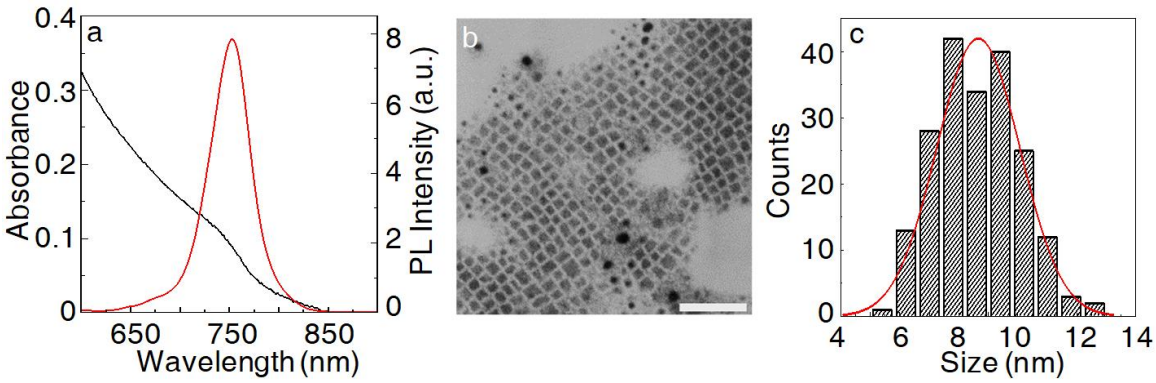

Figure 4.2. Characteristics of $MAPbI_3$ PQDs. (a) Absorption and emission spectra of a $MAPbI_3$ PQDs suspended in toluene. (b) TEM image (scale: 50 nm) and (c) the corresponding histogram of $MAPbI_3$ PQD size.

sample for this measurement was prepared by drop-casting the $MAPbX_3$ PQDs suspended in toluene on a glass coverslip and dragged with the lens cleaning paper for the uniform distribution of single PQDs. Through this process, I was able to control particles' density in the field of view (~10 to 15 single PQDs per 50×50 μm^2 frame). For example, the images recorded from the EMCCD camera of photoluminescent isolated single $MAPbBr_3$ and $MAPbI_3$ PQDs are shown in Figure 4.3a and b, respectively, when irradiated with cw lasers.

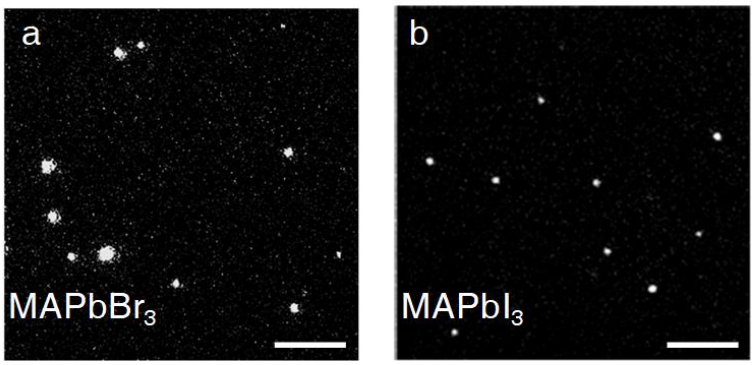

Figure 4.3. Single-particle images of isolate (a) $MAPbBr_3$ PQDs photoexcited with 460 nm cw laser (6.2 W cm^{-2}, scale: 10 μm) and (b) $MAPbI_3$ PQDs photoexcited with a 532 nm cw laser (2 W cm^{-2}, scale: 10 μm).

The single-photon emitting particles were characterized by correlating the coincidence photon counts by the photoexcitation of the PQDs. Park *et al.* and Yuan *et al.* showed strong antibunching of photons in $CsPbI_3$ PQDs by measuring the lowest second-order correlation function (~0.1) at zero delay time, which is the signature of quantum emitters with efficient Auger recombination.[26,49] For obtaining single-photon coincidence counts of $MAPbI_3$ PQDs, PQDs suspended in toluene was spin-coated on a glass coverslip and photoexcited with 450 nm pulsed laser. The excited photons were detected by two avalanche photodiodes at each 125 s delay time. As shown in Figure 4.4a, $MAPbI_3$ PQD shows low coincidence counts at zero delay time, suggesting that photons were excited one by one from a single-emitting particle. On the other hand, a high coincidence counts at zero delay time confirms the presence of a multiphoton-emitting particle or the aggregation of small particles, as shown in Figure 4.4b. The multiphoton emission generally occurs when the excitation intensity is high or when multiple photons absorb tandemly, so we can rule out multiphoton emissions by keeping the low excitation intensity.

This chapter aims to suppress the PL blinking by filling halide vacancies in PQDs. For recording PL intensity trajectories of $MAPbX_3$ (X=Br, I), $MAPbX_3$ PQDs suspended in toluene was drop-cast on a glass coverslip and dragged by using lens cleaning paper. The isolated single $MAPbBr_3$ and $MAPbI_3$ PQDs were obtained through this method, which was photoexcited by 460 and 532 nm cw laser, respectively, and observed under EMCCD. Figure 4.4c-f show some representative PL intensity trajectories observed in $MAPbBr_3$ (Figure 4.4c,d) and $MAPbI_3$ (Figure 4.4e,f) PQDs. These are the two extreme PL blinking behavior observed in the same field of view of PQDs- (i) with frequent ON- and OFF-event

and (ii) with long ON-events. Such PL behavior concludes that the PL blinking differs from particle to particle irrespective of the preparation and the excitation intensity. So, for checking the role of halide vacancy filling, I analyzed the PL blinking in the same PQDs before and after the treatment. I also evaluated the probability distribution of ON- and OFF-times in more than 200 single PQDs.

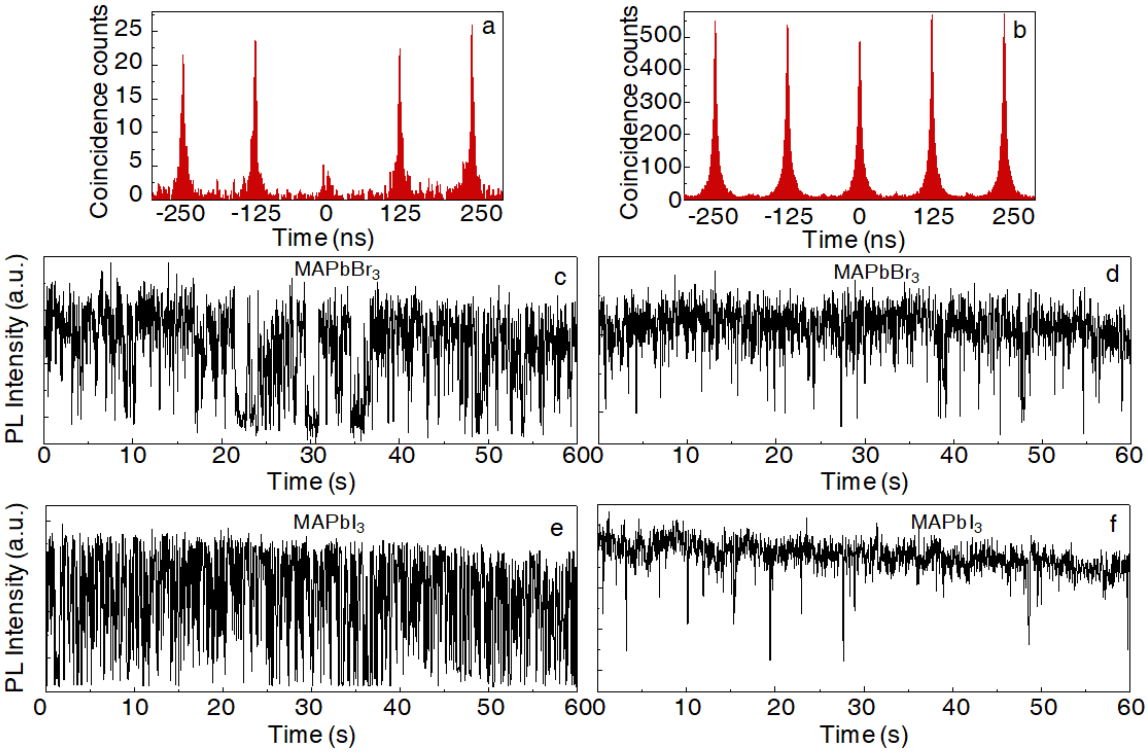

Figure 4.4. Single-particle PL behavior of $MAPbX_3$ PQDs. (a,b) Single-photon coincidence counts of $MAPbI_3$ PQDs irradiated with a 450 nm pulsed laser (30 nW). (a) Single-emitting $MAPbI_3$ PQD and (b) multiphoton emission or aggregates of $MAPbI_3$ PQDs. (c,d) PL intensity trajectories of $MAPbBr_3$ PQDs with (c) high- and (d) low-frequency blinking behavior when photoexcited with a 460 nm cw laser (6.2 W cm^{-2}). (e,f) PL intensity trajectories of $MAPbI_3$ PQDs with (c) high- and (d) low-frequency blinking behavior when photoexcited with a 532 nm cw laser (2 W cm^{-2}).

4.2.2 Halide Vacancy Filling in Single Perovskite Quantum Dots

In lead halide perovskites, ion migration is an obstacle for achieving high PL efficiency and long-term stability. For $MAPbX_3$ perovskite, all the ions MA^+, Pb^{2+}, and X^-, migrate in the crystal under photoexcitation. Huang *et al.* said that the distance between two halide

ions is less than two MA^+ and Pb^{2+} cations in perovskites.[50] Therefore, the migration of halide ions is faster than MA^+ and Pb^{2+} cations. Halide defects in perovskites constitute vacancies, antisites, and interstitials sites. These defects form deep electron and hole traps in the bandgaps of perovskite and responsible for the fast Auger nonradiative recombination.[10,33,50–52] According to the migrating ability, halide defects are first to be filled in the perovskites compared to MA^+ cation. Therefore, to understand the role of halide vacancies of $MAPbX_3$ PQD, I examined the PL blinking before and after the treatment of PQDs with MAX (Br, I), shown in Figures 4.5 and 4.6. 10 mM MAX solutions were prepared by dissolving 0.05 mmol of MAX (MABr= 5.6 mg, MAI= 8 mg) in 5 mL dichloromethane (DCM). Firstly, the PL intensity trajectory of a single $MAPbI_3$ PQD was recorded [Figure 4.5a (i)]. After 50 s, I added MAI solution on the $MAPbI_3$-coated glass coverslip and observed PL behavior of the same PQD [Figure 4.5a (ii)]. Initially, after the

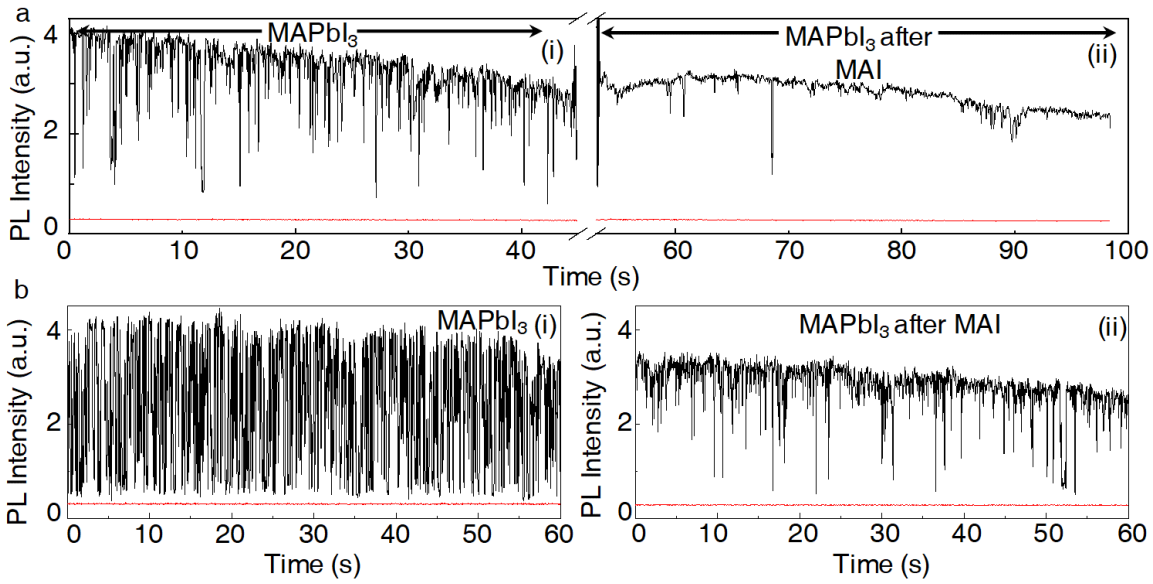

Figure 4.5. PL intensity trajectories of $MAPbI_3$ PQDs. (a, b) The real-time treatment of PQDs before (i) and after (ii) the 10 mM MAI.

MAI addition, the PL fluctuated because of the change in the refractive index, and after a while, the blinking was suppressed. In other words, the time of ON-events increased, resulting in the enhancement of PL. Another example of the real-time addition of MAI on $MAPbI_3$ PQD is shown in Figure 4.5b. Here, the untreated $MAPbI_3$ PQDs showed high-frequency blinking with short ON-and OFF-events. This blinking behavior changed to low-frequency blinking with long ON-events after the treatment.

Similarly, I treated the $MAPbBr_3$ PQDs with MABr and successfully suppressed the PL blinking, as shown in Figure 4.6. Here as well, the PL blinking of the untreated $MAPbBr_3$ PQDs [Figure 4.6a, b(i)] showed high-frequency PL blinking with more OFF-events, which was changed to low-frequency PL blinking with more ON-events after the MABr treatment [Figure 4.6a, b(ii)]. By observing the PL blinking suppression of $MAPbX_3$ PQDs after the treatment with MAX, I conclude that the addition of excess MAX successfully fills the halide vacancies. As the halide-vacancy-related defects constitute deep traps in the bandgaps, filling such defects will reduce the fast Auger nonradiative recombination. According to Chapter-3, the halide vacancy generates superoxide, which ultimately degrades the lead halide perovskites. Therefore, in addition to blinking suppression, the halide vacancy filling also suppresses the generation of superoxide and perovskite oxidation.

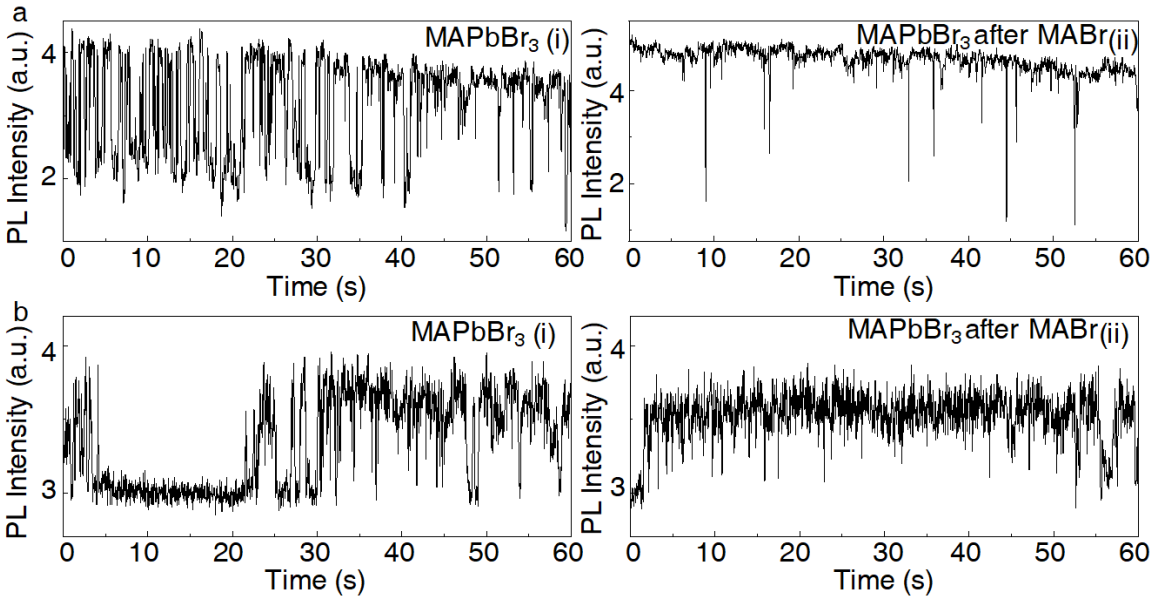

Figure 4.6. PL intensity trajectories of $MAPbBr_3$ PQDs. (a, b) The real-time treatment of PQDs before (i) and after (ii) the 10 mM MABr.

I analyzed the PL blinking of untreated PQDs and the PL blinking suppression by filling halide vacancy after the treatment. Generally, the blinking in PQDs is based on the charging and discharging of excitons (type-A blinking) and the trapping and detrapping of charge carriers (type-B blinking). In type-A blinking, the charging and discharging of excitons results in the generation of trions and the fast Auger nonradiative recombination. Here, the trion generates in a deep trap resulting in the exciton quenching and subsequently decreases the PL intensity and the lifetime. The probability distribution of ON- and OFF

times follow a truncated power law, which is the type-A blinking signature, as explained in Chapter 1 (Section 1.2.2, equation 1.5), $P(\tau) = A_0\tau^{-\alpha}e^{-\frac{\tau}{\tau_c}}$. Here, A_0 is a constant, α is the power-law coefficient, τ_c is the truncation time, and the probability distribution [$P(\tau)$] is calculated using equation 1.7 (Chapter 1, Section 1.2.2), $P(\tau) = \frac{2N_i}{(\tau_{i+1}+\tau_i)-(\tau_i+\tau_{i-1})}$, here, N_i is the occurrence of i^{th} ON- or OFF- time, and τ is the time. The N_i of ON-and OFF-times for pristine $MAPbI_3$ PQDs are shown in Figure 4.7a,b, whereas the MAI-treated PQDs are shown in Figure 4.7c,d. In type-B blinking, charge carriers trap at the band edge or shallow

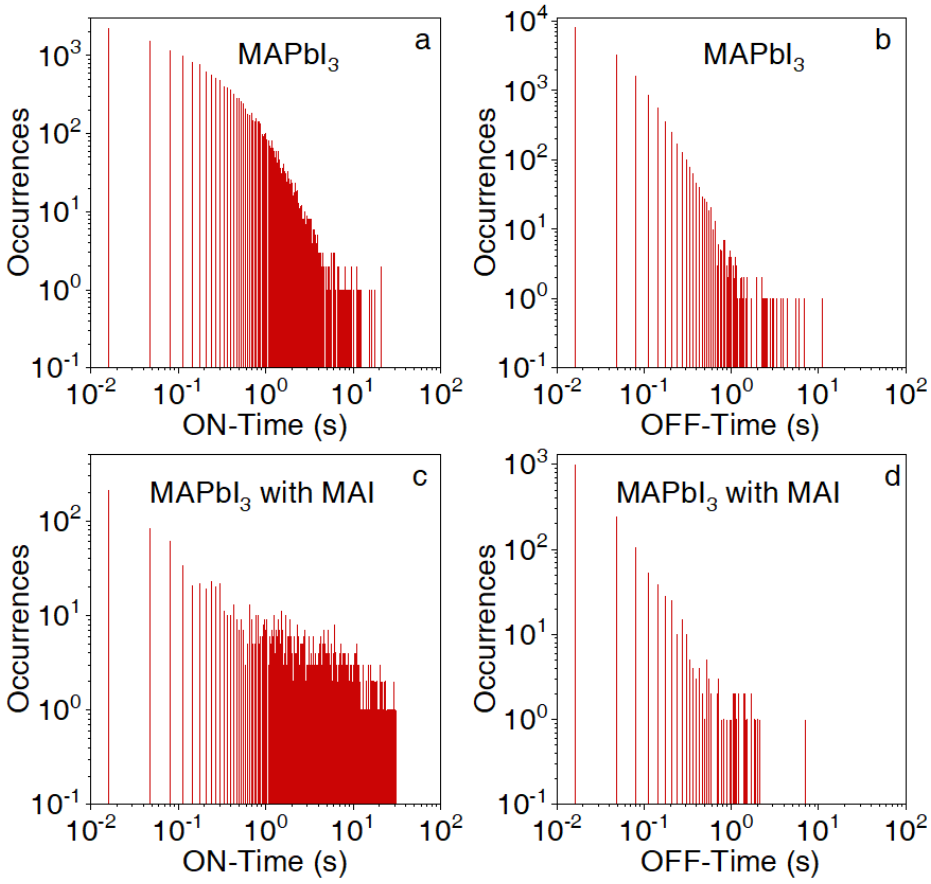

Figure 4.7. The occurrences (N_i) of (a,c) ON- and (b,d) OFF- times of $MAPbI_3$ PQDs before (a,b) and after (c,d) the MAI treatment.

trap states. Trapping and detrapping of short-lived electrons and holes trap states govern nonradiative recombination rate and control the PL intensity and lifetime of the charge carriers, as suggested by Xiao *et al.*[22] The probability distribution of ON- and OFF times follow a linear power law, which is the type-B blinking signature (Chapter 1, Section 1.2.2, equation 1.6), $P(\tau) = A_0\tau^{-\alpha}$. For correlating the role of halide vacancies with the blinking mechanism (type-A and -B), I analyzed more than 200 single $MAPbI_3$ PQDs before and

after the treatment. I fitted the ON- and OFF-time probability distribution by truncated and linear power laws.

The pristine $MAPbI_3$ PQDs showed the truncated power-law behavior of ON-and OFF-times probability distribution (Figure 4.8a,b). Whereas, the MAI-treated PQDs followed linear power-law behavior (Figure 4.8c,d). Pristine PQDs simultaneously show

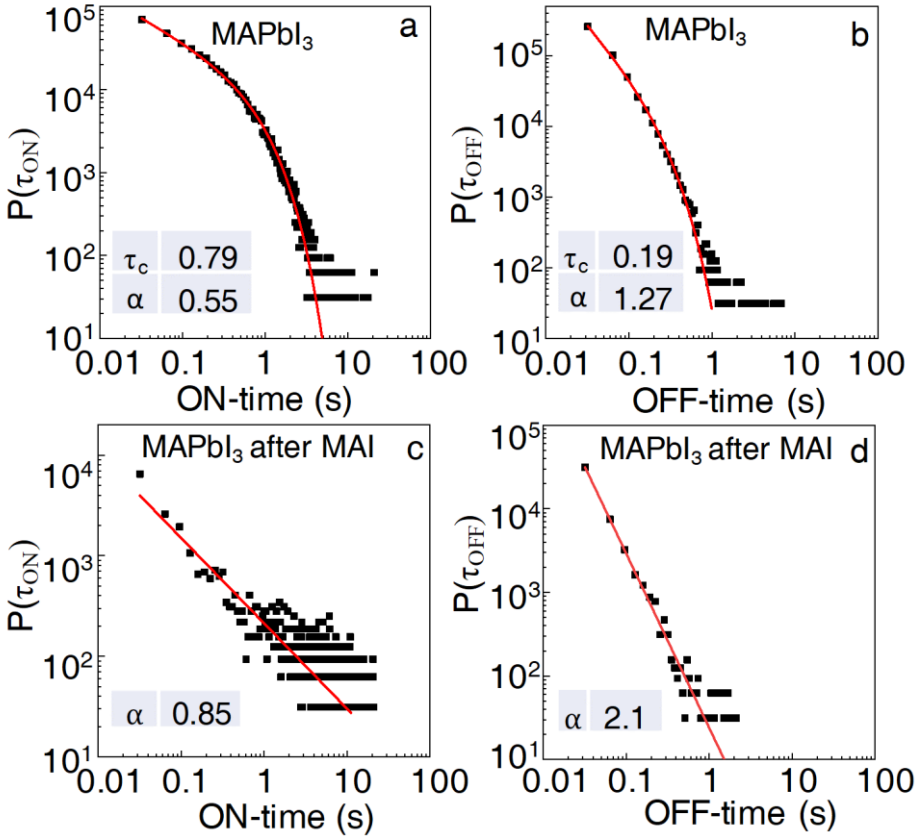

Figure 4.8. The probability distribution of (a,c) ON- and (b,d) OFF- times of $MAPbI_3$ PQDs before (a,b) and after (c,d) the MAI treatment.

both type-A and -B blinking, as explained in the literature.[26–29] Also, type-B blinking in PQDs is subcategorized into two divisions: (i) hot electron and hot hole trapping, which doesn't modulate the PL lifetime, (ii) short-lived band-edge charge carrier trapping or shallow trapping, which linearly decreases the PL lifetime with time.[28,29] Kim *et al.*observed that the deep traps associate with type-A blinking, whereas shallow traps associate with type-B blinking.[29] Therefore, from these findings, I deduce that pristine $MAPbX_3$ PQDs fitted with truncated power-law show both type-A and -B blinking, where type-A dominates for the charge carrier recombination. And the MAX treated $MAPbX_3$ PQDs, fitted with linear power-law, show the dominance of type-B blinking. The change

of blinking from type-A to type-B attributes to the reduction of deep traps associated with halide-vacancy and the suppression of fast nonradiative recombination in $MAPbX_3$ PQDs.

4.2.3 Halide Vacancy Filling in Ensemble of Perovskite Quantum Dots

The single-particle experiment revealed the suppression of PL blinking by the halide vacancy filling. The halide vacancy role on the charge carrier recombination rates and efficiencies is also verified at the ensemble level by recording the PL intensities and decay profiles before and after the MAX treatment on $MAPbX_3$ PQDs. For recording PL intensities, the $MAPbBr_3$ and $MAPbI_3$ PQDs suspensions in toluene were drop-cast on glass coverslips. The PL intensities of the samples are recorded at 2 min interval. For the MAX treatment, I dropped 10 mM MABr and MAI solution (in DCM) on the $MAPbBr_3$- or $MAPbI_3$- coated glass coverslips, respectively. The change in relative PL intensities before and after the treatment is shown in Figure 4.9. The PL intensity of $MAPbBr_3$ PQDs increased by 185%, and after the MABr treatment, the PL intensity increased by 280% (Figure 4.9a). In the case of pristine $MAPbI_3$ PQDs, the PL intensity is increased by 150%,

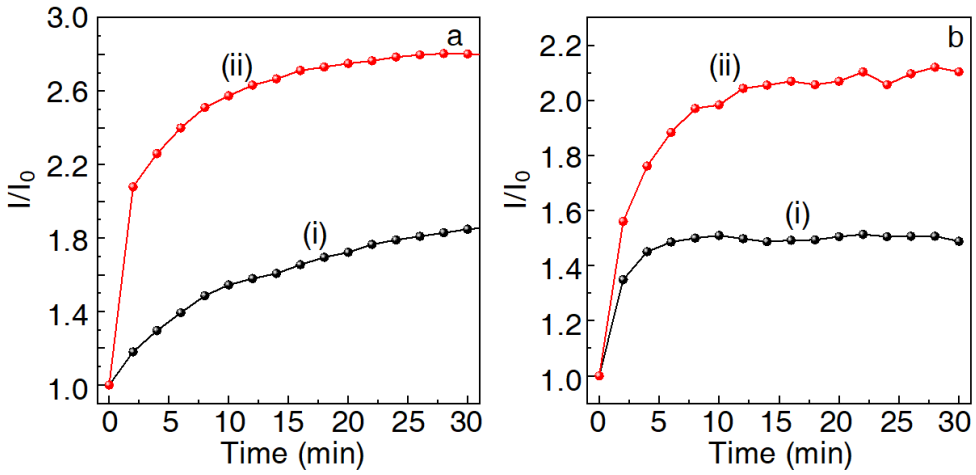

Figure 4.9. Relative PL intensities of (a) $MAPbBr_3$ PQDs and (b) $MAPbI_3$ PQDs before (i) and after (ii) the treatment with MABr and MAI, respectively.

and after the MAI treatment, the PL intensity increased by 210% (Figure 4.9b). The more percentage increase of PL intensities after the treatment results in the filling of halide vacancies. The enormous rise in PL intensities in both cases relates to the photo-brightening effect and reduction in halide-vacancy-related defects, suppressing the nonradiative

recombination of photogenerated charge carriers. The photo-brightening effect in perovskites is possible when the excitation intensity is very low and the sample is kept under dark, which reduces the chance of the oxidation of perovskite and the generation of superoxide.

Also, by SEM-EDX measurement, I estimated the density of halide vacancies in the $MAPbX_3$ PQDs by analyzing the elemental composition of lead and iodide in $MAPbI_3$ PQDs before and after the MAI treatment. Here, the PQD samples were prepared by drop-casting $MAPbI_3$ PQDs suspended in toluene on an ITO glass. The sample was dried under vacuum for 2 h, and the PQDs were examined under the SEM-EDX, and the SEM images and elemental compositions of the PQDs were obtained. Figure 4.10a shows typical SEM-EDX spectrum of $MAPbI_3$ PQDs. Then, I treated the same PQDs with a 10 mM MAI solution in DCM. The SEM-EDX spectrum of the same area after the treatment was examined (Figure 4.10b). From the EDX spectra, I estimated that the elemental ratio of I to Pb was increased by *ca* 4 % after the MAI treatment. Nevertheless, the sample to sample variations of this elemental ratio and the E-beam induced sample damage did not allow me to precisely quantify the defect density.

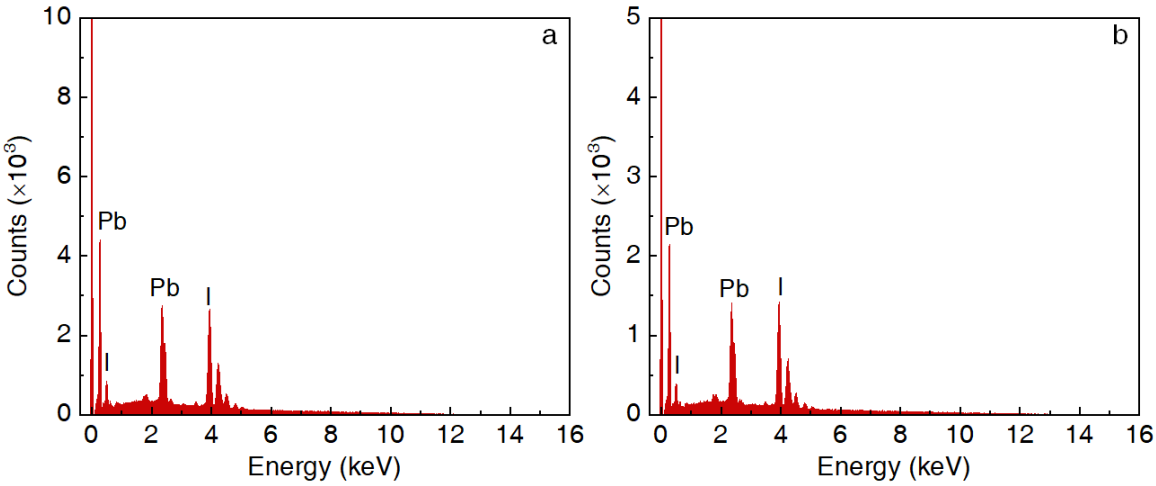

Figure 4.10. SEM-EDX spectra of $MAPbI_3$ PQDs (a) before and (b) after MAI treatment.

Further, to confirm the role of halides on PL, I analyzed the relative PLQY of the $MAPbBr_3$ PQD suspension with reference to fluorescein. As shown in Figure 4.11a, the emission maxima of fluorescein is *ca* 516 nm, and that of $MAPbBr_3$ is *ca* 532 nm. For reference, fluorescein was used because $MAPbBr_3$ emission maximum lies within the

fluorescein emission. According to the literature, the QY of the fluorescein is 0.79 in ethanol. The relative QY of $MAPbBr_3$ is calculated by

$$QY = QY_{ref.} \times \frac{A_{ref}}{A_{PNC}} \times \frac{E_{PNC}}{E_{ref}} \times \frac{\eta_{PNC}^2}{\eta_{ref}^2} \quad (4.1)$$

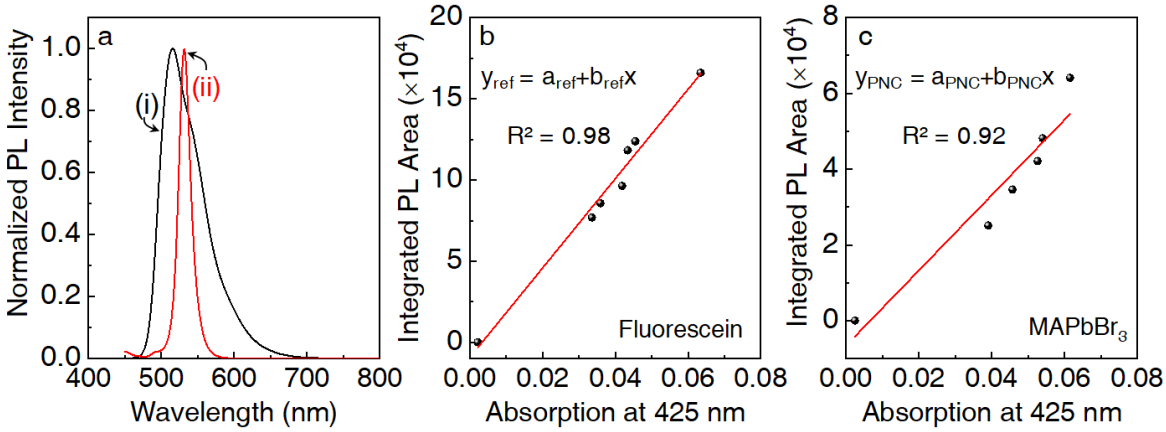

Figure 4.11. PLQY estimation. (a) Emission spectra of fluorescein and $MAPbBr_3$ PQDs. (b,c) Linear fit for absorbance to integrated emission area in (b) fluorescein and (b) $MAPbBr_3$ PQDs.

$$QY = QY_{ref.} \times \frac{b_{PNC}}{b_{ref}} \times \frac{\eta_{PNC}^2}{\eta_{ref}^2} \quad (4.2)$$

Here, *A* is the absorbance, *E* is the integrated area of the emission, η is the refractive index of the solvent, *b* is the slope of the fitting equation ($y=a+bx$), and *ref.* denotes the reference. I recorded absorbance and PL of fluorescein and $MAPbBr_3$ PQDs at various dilutions and plotted *A* vs. *E*, as shown in Figure 4.11b, c, respectively. The PLQY of the $MAPbBr_3$ PQD calculated from the above equations (4.1 and 4.2) is 0.35, and that of MABr treated $MAPbBr_3$ PQD is 0.98.

Similarly, I calculated the PLQY of fresh $MAPbI_3$ PQD with reference to AlexaFluor700 Figure 4.12. The PL maxima of the AlexaFluor700 is *ca* 714 nm and the PLQY is 0.25 in phosphate-buffer saline solution. As the sample lies in the near-infrared region, the relative PLQY was calculated after applying the correction to the quantum efficiency of the detector in the 650 to 800 nm region. The relative PLQY of $MAPbI_3$ PQD is estimated at 0.23, and that of MAI treated $MAPbI_3$ PQD is 0.48. Thus, the filling of halides in the PQDs leads to the enhancement of the PL.

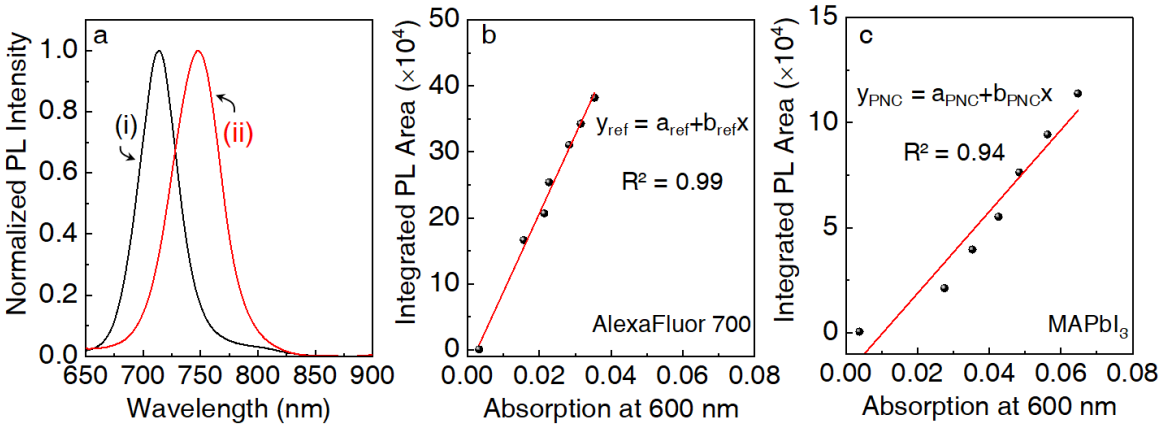

Figure 4.12. PLQY estimation. (a) Emission spectra of AlexaFluor 700 and $MAPbI_3$ PNCs. (b,c) Linear fit for absorbance to integrated emission area in (b) AlexaFluor 700 and (b) $MAPbI_3$ PQDs.

To verify it further, the relationship among halide vacancy filling, PL blinking, and the charge carrier dynamics before and after the treatment of $MAPbX_3$ PQDs, the PL decay profiles are recorded. The samples were prepared by drop-casting the $MAPbX_3$ PQD suspended in toluene on glass-coverslips. First, the PL decay profiles were recorded for the pristine PQD sample, then the 10 mM MAX solution (in DCM) was dropped on the $MAPbX_3$-coated glass coverslips (Figure 4.13). Again, the PL decay profiles of the treated area were recorded. The excitation intensity for recording the PL lifetime of $MAPbBr_3$ PQD samples was 3.5 mW cm^{-2}, and for $MAPbI_3$ PQD samples was 9 mW cm^{-2}. Similar to chalcogenide QDs, the perovskite also shows multiphase decay dynamics.[35,37] Therefore, I fitted the PL decay profile with a fourth order exponential decay equation and calculated

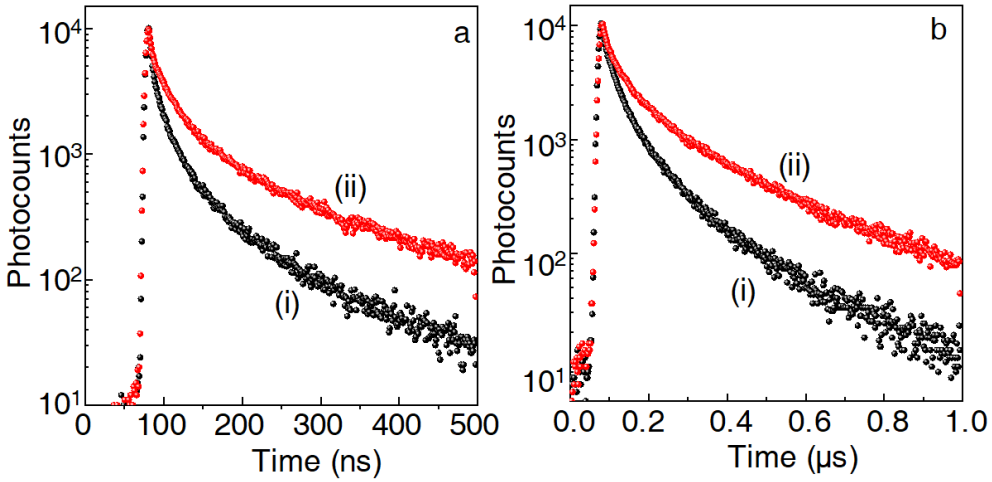

Figure 4.13. PL decay profiles of ensembled-averaged (a) $MAPbBr_3$ PQDs and (b) $MAPbI_3$ PQDs before (i) and after (ii) the treatment with MABr and MAI, respectively.

the average PL lifetime (Chapter 2, section 2.2.5, equation 2.2 and 2.3). The average PL lifetime of ensemble-averaged $MAPbBr_3$ PQDs increased from 11.5 to 23 ns after treating with MABr solution (Figure 4.13a). And the average PL lifetime of ensemble-averaged $MAPbI_3$ PQD increased from 27 to 65 ns after treating with MAI solution (Figure 4.13b). The dynamics of emissive and nonemissive states can be convoluted by the fitting of the decay profiles. Here, the PQDs showed fast decay in the starting few ns, which associates with nonemissive states. This fast decay was suppressed after the treatment with MAX. However, the long decay, which associates with an emissive state, remains similar before and after the treatment.

For estimating the rates of nonradiative recombination through halide-vacancies, the relative PL intensities and the average PL lifetimes before and after the treatment of $MAPbX_3$ PQDs were considered. In the case of $MAPbI_3$ PQDs, an increase by 2.1 fold in relative PL intensities and 2.4 fold increase in average PL lifetime were observed. The PL lifetime (τ_0) for the pristine $MAPbI_3$ PQDs can be written as,

$$\tau_0 = \frac{1}{(k_r + k_{nr_1} + k_{nr_2}) + k_{nrI_v}} \tag{4.3}$$

here, $k_r$is the rate of radiative recombination, k_{nr_1} and $k_{nr_2}$are the rates of nonradiative recombination through the states other than iodide vacancies, and k_{nrI_v} is the rate of nonradiative recombination through the iodide vacancies. The PL lifetime (τ) of $MAPbI_3$ treated with MAI can be written as

$$\tau = \frac{1}{(k_r + k_{nr_1} + k_{nr_2})} \tag{4.4}$$

Thus, by combining equations 4.3 and 4.4,

$$\frac{\tau}{\tau_0} = \frac{(k_r + k_{nr_1} + k_{nr_2}) + k_{nrI_v}}{(k_r + k_{nr_1} + k_{nr_2})} \tag{4.5}$$

By putting τ as 27 ns and τ_0 as 65 ns, I calculated the k_{nrI_v} at 1.54×10^7 s^{-1}.

Similarly, I calculated the rate of nonradiative recombination through bromide vacancies (k_{nrBr_v}) in the case of $MAPbBr_3$ PQDs. I observed a 2.8 fold increase in relative PL intensities and a 2.0 fold increase in average PL lifetime. Therefore, by putting τ as 11.5 ns and τ_0 as 23 ns, I calculated the k_{nrBr_v} at 4.35×10^7 s^{-1}. The $>10^7$ s^{-1} rate is minimal as

per the standard nonradiative recombination, which is $>10^9$ s^{-1}. Thus, it was necessary to consider the fast component of isolated single PQDs.

For analyzing the PL lifetime of isolated $MAPbX_3$ PQDs, the PQDs were diluted in toluene and drop-casted on a glass coverslip. In this experiment, I consider only 5-10 isolated single-particles under the field of view. The $MAPbX_3$ PQDs were irradiated with 460 nm cw laser, and the PL decays were recorded before and after MAX treatment using a time-correlated single-photon counting system. The instrumentation of the time-correlated single-photon counting system is detailed in Chapter-2, section 2.2.5. The PL decays were fitted similarly, using the fourth order exponential equation. The PL decay profiles of isolated $MAPbBr_3$ and $MAPbI_3$ PQDs before and after MABr and MAI treatment are shown in Figure 4.14. Here, the initial rapid decay of PQDs was suppressed

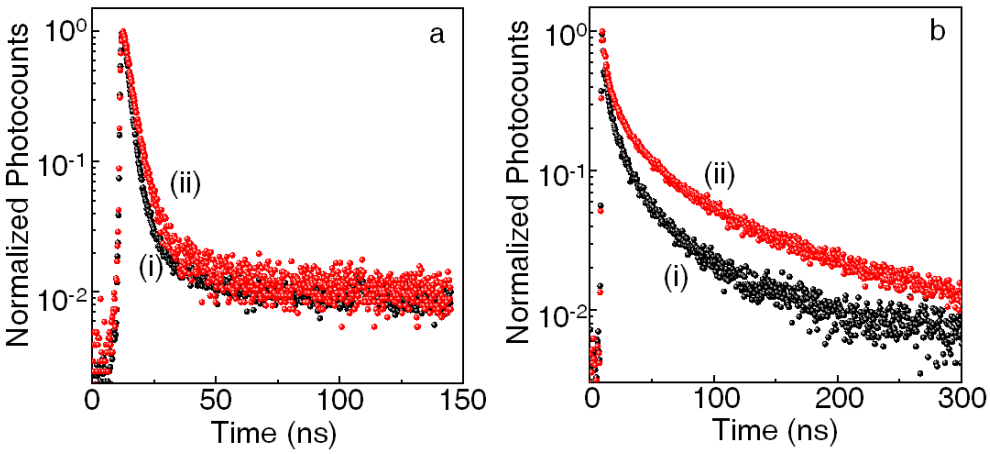

Figure 4.14. PL decay profiles of (a) $MAPbBr_3$ PQDs and (b) $MAPbI_3$ PQDs before (i) and after (ii) the treatment with MABr and MAI, respectively.

after the treatment, which results in the decrease of deep traps and the fast nonradiative relaxation associated with halide vacancies. In the case of $MAPbBr_3$ PQDs, the fast component increased from 2.5 to 3.2 ns after MABr treatment (Figure 4.14a), and in the case of $MAPbI_3$ PQDs, it increased from 0.26 to 0.51 ns after the MAI treatment (Figure 4.14b). While considering the lifetime of fast component, I estimated the rate of nonradiative recombination through halide vacancies from equations 4.3 to 4.5 at 1×10^8 s^{-1} for $MAPbBr_3$ and 1.9×10^9 s^{-1} for $MAPbI_3$ PQDs. These high rates indicate the fast nonradiative recombination of excitons is mainly by the halide vacancies. Hence, the halide vacancies act as quenchers for PL intensity and lifetime in $MAPbX_3$ PQDs, and they are responsible for the PL blinking in PQDs.

4.2.4 The Mechanism of Photoluminescence Blinking

In Figure 4.15, I schematically represented the effect of halide-vacancy filling with the PL blinking suppression, increases in PL intensity, and PL lifetimes of $MAPbX_3$ PQDs. Figure 4.15a shows the filling of halide vacancies in pristine PQD. Figure 4.15b shows the mechanism of type-A and type-B blinking in pristine PQD and treated PQDs, respectively. If deep electron and hole traps are present in the energy levels of PQD, the positive or negative trions can generate [Figure 4.15b(i)]. In type-A blinking, charging-discharging of these photogenerated trions is responsible for the fast Auger nonradiative recombination. The deep traps correspond to the halide vacancies in the as-synthesized PQDs electronic levels.[10,33,50–52] And the fast Auger nonradiative recombination decreases the PL intensity and the PL lifetime of the PQDs. When the $MAPbX_3$ PQDs were treated with MAX, it helped in filling the deep-traps related to halide vacancies [Figure 4.15b(ii)]. Hence, it changed the power-law behavior from truncated (type-A) to linear (type-B), analyzed from

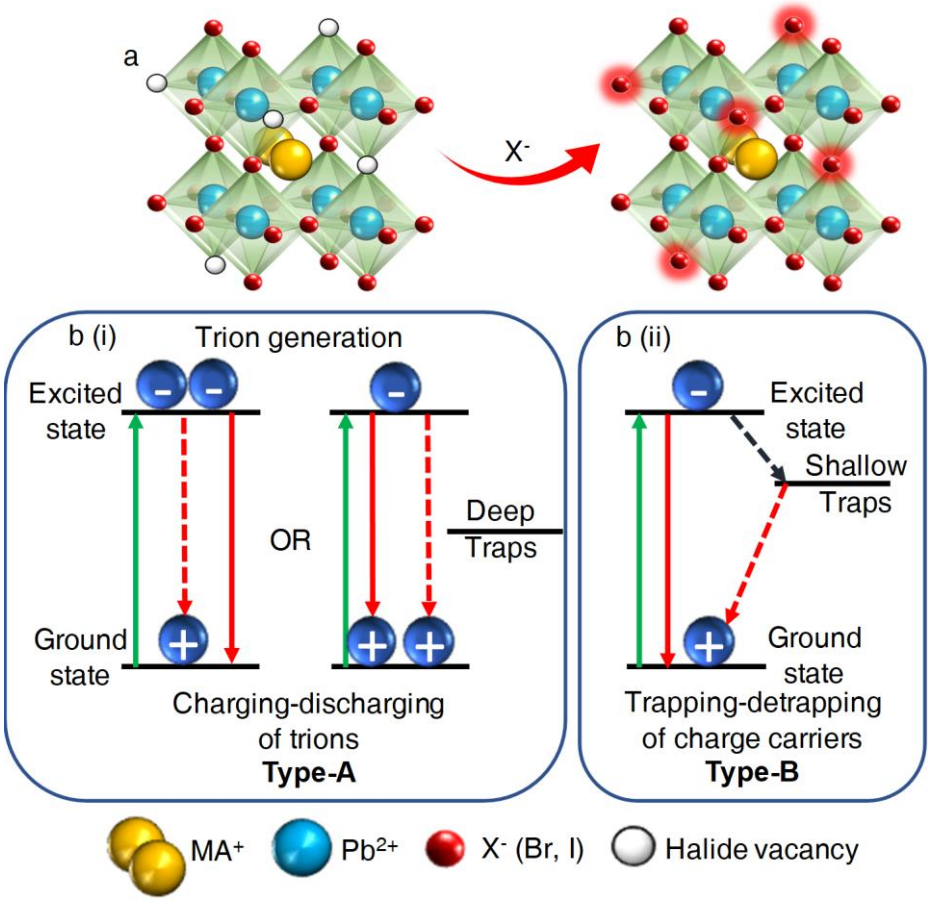

Figure 4.15. (a) Schematic representation of the filling of halide vacancies in PQD and (b) the corresponding change in the models of PL blinking mechanism in (i) type-A and (ii) type-B.

the probability distribution of ON-and OFF- times. In type-B blinking, trapping and detrapping of shallow or band-edge trap states are responsible for the nonradiative recombination of photogenerated excitons.

4.3 Conclusion

In summary, I studied the role of halide vacancies in the photoluminescence properties and the charge carrier dynamics of the $MAPbX_3$ perovskite quantum dots at the single-particle and the ensemble level. When the lead halide perovskite interacts with light and air, it oxidizes and reacts with environmental oxygen to generate superoxide. This superoxide occupies the halide vacancies present in the lead halide perovskite and degrades the nanocrystals. Therefore, in this chapter, I aimed to fill the halide vacancies and prevent superoxide generation under air atmosphere. For this, I chose MAX salts for increasing the halide ions concentration in the perovskite quantum dots. I demonstrated the role of halide vacancies before and after the addition of MABr (and MAI) on $MAPbBr_3$ (and $MAPbI_3$) perovskite quantum dots. I synthesized $MAPbBr_3$ and $MAPbI_3$ with a size of ~10.6 and ~8.5 nm, respectively, using the ligand-assisted reprecipitation method. $MAPbBr_3$ and $MAPbI_3$ both showed narrow and single emission maximum *ca* 530 and 750 nm. These perovskite quantum dots showed photoluminescence blinking when photoexcited with distinct ON(radiative)- and OFF(nonradiative)-times. The blinking varies from particle to particle independent of excitation intensity. Some perovskite quantum dots showed strong photon-antibunching verifying the emission from a single-emitting particle, whereas some showed multiphoton emission. Therefore, I checked the post-synthesis filling of halide ions on the same perovskite quantum dot before and after the halide salt treatment. I suppressed the photoluminescence blinking at real-time addition of halide ions in $MAPbX_3$ perovskite quantum dots. After the treatment with MAX, the duration of ON-events increased compared to before the treatment. This promotes the increase in photoluminescence and the reduction of halide-vacancy-assisted nonradiative recombination. After analyzing more than 200 single-particles of $MAPbI_3$, I constructed the probability distribution of ON-and OFF-times, which showed the change in blinking mechanisms from type-A to type-B after the treatment, suggesting decreased deep-traps. In other words, the dominance of charging-discharging of photogenerated excitons in $MAPbI_3$ perovskite quantum dots changed by the trapping-detrapping of excitons after the treatment. I also verified the

photoluminescence behavior of $MAPbX_3$ before and after the filling of halide vacancies at ensemble-level experiments. $MAPbBr_3$ and $MAPbI_3$ perovskite quantum dots showed an increase of 2.8- and 2.1-fold in the photoluminescence intensities after the treatment. From the SEM-EDX data, I estimated that the halide vacancy concentration in the perovskite quantum dots is *ca* 4%. I examined the photoluminescence decay profiles of the ensemble of single $MAPbBr_3$ and $MAPbI_3$ perovskite quantum dots before and after the treatment and observed the increase in photoluminescence lifetime with the filling of halide vacancies suggesting the decrease in the suppression of nonradiative relaxation pathways. With the help of the average lifetimes of $MAPbX_3$ perovskite quantum dots, I calculated the halide-vacancy-assisted nonradiative recombination rates at 1×10^8 s^{-1} for $MAPbBr_3$ and 1.9×10^9 s^{-1} for $MAPbI_3$ perovskite quantum dots. Thus, I demonstrated the real-time suppression of PL blinking with the suppression of halide-vacancy-assisted nonradiative recombination and increases in photoluminescence lifetime and intensity in $MAPbX_3$ perovskite quantum dots by filling the halide vacancies. In lead halide perovskites, the blinking changes from type-A to type-B by filling up deep-traps related to halide vacancies, but cation vacancies are yet to consider for better photoluminescence efficiencies and more extended stability.

4.4 References

(1) Kojima, A.; Teshima, K.; Shirai, Y.; Miyasaka, T. Organometal Halide Perovskites as Visible-Light Sensitizers for Photovoltaic Cells. *J. Am. Chem. Soc.* **2009**, *131*, 6050–6051.

(2) Yang, W. S.; Noh, J. H.; Jeon, N. J.; Kim, Y. C.; Ryu, S.; Seo, J.; Seok, S. Il. High-Performance Photovoltaic Perovskite Layers Fabricated through Intramolecular Exchange. *Science* **2015**, *348*, 1234–1237.

(3) Dou, L.; Yang, Y. (Micheal); You, J.; Hong, Z.; Chang, W.-H.; Li, G.; Yang, Y. Solution-Processed Hybrid Perovskite Photodetectors with High Detectivity. *Nat. Commun.* **2014**, *5*, 5404.

(4) Wang, N.; Cheng, L.; Ge, R.; Zhang, S.; Miao, Y.; Zou, W.; Yi, C.; Sun, Y.; Cao, Y.; Yang, R.; Wei, Y.; Guo, Q.; Ke, Y.; Yu, M.; Jin, Y.; Liu, Y.; Ding, Q.; Di, D.; Yang, L.; Xing, G.; Tian, H.; Jin, C.; Gao, F.; Friend, R. H.; Wang, J.; Huang, W. Perovskite Light-Emitting Diodes Based on Solution-Processed Self-Organized Multiple Quantum Wells. *Nat. Photonics* **2016**, *10*, 699–704.

(5) Chen, S.; Roh, K.; Lee, J.; Chong, W. K.; Lu, Y.; Mathews, N.; Sum, T. C.; Nurmikko, A. A Photonic Crystal Laser from Solution Based Organo-Lead Iodide Perovskite Thin Films. *ACS Nano* **2016**, *10*, 3959–3967.

(6) Protesescu, L.; Yakunin, S.; Bodnarchuk, M. I.; Krieg, F.; Caputo, R.; Hendon, C. H.; Yang, R. X.; Walsh, A.; Kovalenko, M. V. Nanocrystals of Cesium Lead Halide Perovskites ($CsPbX_3$, X = Cl, Br, and I): Novel Optoelectronic Materials Showing Bright Emission with Wide Color Gamut. *Nano Lett.* **2015**, *15*, 3692–3696.

(7) Zhang, F.; Zhong, H.; Chen, C.; Wu, X. G.; Hu, X.; Huang, H.; Han, J.; Zou, B.; Dong, Y. Brightly Luminescent and Color-Tunable Colloidal $CH_3NH_3PbX_3$ (X = Br, I, Cl) Quantum Dots: Potential Alternatives for Display Technology. *ACS Nano* **2015**, *9*, 4533–4542.

(8) Levchuk, I.; Osvet, A.; Tang, X.; Brandl, M.; Perea, J. D.; Hoegl, F.; Matt, G. J.; Hock, R.; Batentschuk, M.; Brabec, C. J. Brightly Luminescent and Color-Tunable Formamidinium Lead Halide Perovskite $FAPbX_3$ (X = Cl, Br, I) Colloidal Nanocrystals. *Nano Lett.* **2017**, *17*, 2765–2770.

(9) Ghimire, S.; Chouhan, L.; Takano, Y.; Takahashi, K.; Nakamura, T.; Yuyama, K.; Biju, V. Amplified and Multicolor Emission from Films and Interfacial Layers of Lead Halide Perovskite Nanocrystals. *ACS Energy Lett.* **2019**, *4*, 133–141.

(10) Agiorgousis, M. L.; Sun, Y.-Y.; Zeng, H.; Zhang, S. Strong Covalency-Induced Recombination Centers in Perovskite Solar Cell Material $CH_3NH_3PbI_3$. *J. Am. Chem. Soc.* **2014**, *136*, 14570–14575.

(11) Guo, T.; Bose, R.; Zhou, X.; Gartstein, Y. N.; Yang, H.; Kwon, S.; Kim, M. J.; Lutfullin, M.; Sinatra, L.; Gereige, I.; Al-Saggaf, A.; Bakr, O. M.; Mohammed, O. F.; Malko, A. V. Delayed Photoluminescence and Modified Blinking Statistics in Alumina-Encapsulated Zero-Dimensional Inorganic Perovskite Nanocrystals. *J. Phys. Chem. Lett.* **2019**, *10*, 6780–6787.

(12) Stranks, S. D.; Eperon, G. E.; Grancini, G.; Menelaou, C.; Alcocer, M. J. P.; Leijtens, T.; Herz, L. M.; Petrozza, A.; Snaith, H. J. Electron-Hole Diffusion Lengths Exceeding 1 Micrometer in an Organometal Trihalide Perovskite Absorber. *Science* **2013**, *342*, 341–344.

(13) Shi, D.; Adinolfi, V.; Comin, R.; Yuan, M.; Alarousu, E.; Buin, A.; Chen, Y.; Hoogland, S.; Rothenberger, A.; Katsiev, K.; Losovyj, Y.; Zhang, X.; Dowben, P. A.; Mohammed, O. F.; Sargent, E. H.; Bakr, O. M. Low Trap-State Density and Long Carrier Diffusion in Organolead Trihalide Perovskite Single Crystals. *Science* **2015**, *347*, 519–522.

(14) Ma, L.; Hao, F.; Stoumpos, C. C.; Phelan, B. T.; Wasielewski, M. R.; Kanatzidis, M. G. Carrier Diffusion Lengths of over 500 Nm in Lead-Free Perovskite $CH_3NH_3SnI_3$ Films. *J. Am. Chem. Soc.* **2016**, *138*, 14750–14755.

(15) Milot, R. L.; Eperon, G. E.; Snaith, H. J.; Johnston, M. B.; Herz, L. M. Temperature-Dependent Charge-Carrier Dynamics in $CH_3NH_3PbI_3$ Perovskite Thin Films. *Adv. Funct. Mater.* **2015**, *25*, 6218–6227.

(16) Wang, L.; Wang, K.; Zou, B. Pressure-Induced Structural and Optical Properties of Organometal Halide Perovskite-Based Formamidinium Lead Bromide. *J. Phys. Chem. Lett.* **2016**, *7*, 2556–2562.

(17) Aristidou, N.; Sanchez-Molina, I.; Chotchuangchutchaval, T.; Brown, M.; Martinez,

L.; Rath, T.; Haque, S. A. The Role of Oxygen in the Degradation of Methylammonium Lead Trihalide Perovskite Photoactive Layers. *Angew. Chem.* **2015**, *127*, 8326–8330.

(18) Ghimire, S.; Takahashi, K.; Takano, Y.; Nakamura, T.; Biju, V. Photon Recycling by Energy Transfer in Piezochemically Synthesized and Close-Packed Methylammonium Lead Halide Perovskites. *J. Phys. Chem. C* **2019**, *123*, 27752–27758.

(19) Jin, H.; Debroye, E.; Keshavarz, M.; Scheblykin, I. G.; Roeffaers, M. B. J.; Hofkens, J.; Steele, J. A. It's a Trap! On the Nature of Localised States and Charge Trapping in Lead Halide Perovskites. *Mater. Horizons* **2020**, *7*, 397–410.

(20) Ran, C.; Xu, J.; Gao, W.; Huang, C.; Dou, S. Defects in Metal Triiodide Perovskite Materials towards High-Performance Solar Cells: Origin, Impact, Characterization, and Engineering. *Chem. Soc. Rev.* **2018**, *47*, 4581–4610.

(21) Chouhan, L.; Ghimire, S.; Biju, V. Blinking Beats Bleaching: The Control of Superoxide Generation by Photo-ionized Perovskite Nanocrystals. *Angew. Chem. Int. Ed.* **2019**, *58*, 4875–4879.

(22) Li, B.; Huang, H.; Zhang, G.; Yang, C.; Guo, W.; Chen, R.; Qin, C.; Gao, Y.; Biju, V. P.; Rogach, A. L.; Xiao, L.; Jia, S. Excitons and Biexciton Dynamics in Single $CsPbBr_3$ Perovskite Quantum Dots. *J. Phys. Chem. Lett.* **2018**, *9*, 6934–6940.

(23) Ahmed, T.; Seth, S.; Samanta, A. Mechanistic Investigation of the Defect Activity Contributing to the Photoluminescence Blinking of $CsPbBr_3$ Perovskite Nanocrystals. *ACS Nano* **2019**, *13*, 13537–13544.

(24) Yuan, H.; Debroye, E.; Bladt, E.; Lu, G.; Keshavarz, M.; Janssen, K. P. F.; Roeffaers, M. B. J.; Bals, S.; Sargent, E. H.; Hofkens, J. Imaging Heterogeneously Distributed Photo-Active Traps in Perovskite Single Crystals. *Adv. Mater.* **2018**, *30*, 1705494.

(25) Sharma, D. K.; Hirata, S.; Biju, V.; Vacha, M. Stark Effect and Environment-Induced Modulation of Emission in Single Halide Perovskite Nanocrystals. *ACS Nano* **2019**, *13*, 624–632.

(26) Yuan, G.; Ritchie, C.; Ritter, M.; Murphy, S.; Gómez, D. E.; Mulvaney, P. The Degradation and Blinking of Single $CsPbI_3$ Perovskite Quantum Dots. *J. Phys. Chem.*

C **2018**, *122*, 13407–13415.

(27) Trinh, C. T.; Minh, D. N.; Ahn, K. J.; Kang, Y.; Lee, K. G. Organic-Inorganic FAPbBr3 Perovskite Quantum Dots as a Quantum Light Source: Single-Photon Emission and Blinking Behaviors. *ACS Photonics* **2018**, *5*, 4937–4943.

(28) Trinh, C. T.; Minh, D. N.; Ahn, K. J.; Kang, Y.; Lee, K.-G. Verification of Type-A and Type-B-HC Blinking Mechanisms of Organic–Inorganic Formamidinium Lead Halide Perovskite Quantum Dots by FLID Measurements. *Sci. Rep.* **2020**, *10*, 2172.

(29) Kim, T.; Jung, S. Il; Ham, S.; Chung, H.; Kim, D. Elucidation of Photoluminescence Blinking Mechanism and Multiexciton Dynamics in Hybrid Organic-Inorganic Perovskite Quantum Dots. *Small* **2019**, *15*, 1900355.

(30) Tian, Y.; Merdasa, A.; Peter, M.; Abdellah, M.; Zheng, K.; Ponseca, C. S.; Pullerits, T.; Yartsev, A.; Sundström, V.; Scheblykin, I. G. Giant Photoluminescence Blinking of Perovskite Nanocrystals Reveals Single-Trap Control of Luminescence. *Nano Lett.* **2015**, *15*, 1603–1608.

(31) Yuan, H.; Debroye, E.; Caliandro, G.; Janssen, K. P. F.; Van Loon, J.; Kirschhock, C. E. A.; Martens, J. A.; Hofkens, J.; Roeffaers, M. B. J. Photoluminescence Blinking of Single-Crystal Methylammonium Lead Iodide Perovskite Nanorods Induced by Surface Traps. *ACS Omega* **2016**, *1*, 148–159.

(32) Merdasa, A.; Tian, Y.; Camacho, R.; Dobrovolsky, A.; Debroye, E.; Unger, E. L.; Hofkens, J.; Sundström, V.; Scheblykin, I. G. "Supertrap" at Work: Extremely Efficient Nonradiative Recombination Channels in $MAPbI_3$ Perovskites Revealed by Luminescence Super-Resolution Imaging and Spectroscopy. *ACS Nano* **2017**, *11*, 5391–5404.

(33) Galisteo-López, J. F.; Calvo, M. E.; Rojas, T. C.; Míguez, H. Mechanism of Photoluminescence Intermittency in Organic–Inorganic Perovskite Nanocrystals. *ACS Appl. Mater. Interfaces* **2019**, *11*, 6344–6349.

(34) Nirmal, M.; Dabbousi, B. O.; Bawendi, M. G.; Macklin, J. J.; Trautman, J. K.; Harris, T. D.; Brus, L. E. Fluorescence Intermittency in Single Cadmium Selenide Nanocrystals. *Nature* **1996**, *383*, 802–804.

(35) Galland, C.; Ghosh, Y.; Steinbrück, A.; Sykora, M.; Hollingsworth, J. A.; Klimov,

V. I.; Htoon, H. Two Types of Luminescence Blinking Revealed by Spectroelectrochemistry of Single Quantum Dots. *Nature* **2011**, *479*, 203–207.

(36) Hamada, M.; Nakanishi, S.; Itoh, T.; Ishikawa, M.; Biju, V. Blinking Suppression in CdSe/ZnS Single Quantum Dots by TiO_2 Nanoparticles. *ACS Nano* **2010**, *4*, 4445–4454.

(37) Thomas, E. M.; Ghimire, S.; Kohara, R.; Anil, A. N.; Yuyama, K.; Takano, Y.; Thomas, K. G.; Biju, V. Blinking Suppression in Highly Excited CdSe/ZnS Quantum Dots by Electron Transfer under Large Positive Gibbs (Free) Energy Change. *ACS Nano* **2018**, *12*, 9060–9069.

(38) Hohng, S.; Ha, T. Near-Complete Suppression of Quantum Dot Blinking in Ambient Conditions. *J. Am. Chem. Soc.* **2004**, *126*, 1324–1325.

(39) Chouhan, L.; Ghimire, S.; Subrahmanyam, C.; Miyasaka, T.; Biju, V. Synthesis, Optoelectronic Properties and Applications of Halide Perovskites. *Chem. Soc. Rev.* **2020**, *49*, 2869–2885.

(40) Vickers, E. T.; Graham, T. A.; Chowdhury, A. H.; Bahrami, B.; Dreskin, B. W.; Lindley, S.; Naghadeh, S. B.; Qiao, Q.; Zhang, J. Z. Improving Charge Carrier Delocalization in Perovskite Quantum Dots by Surface Passivation with Conductive Aromatic Ligands. *ACS Energy Lett.* **2018**, *3*, 2931–2939.

(41) Raja, S. N.; Bekenstein, Y.; Koc, M. A.; Fischer, S.; Zhang, D.; Lin, L.; Ritchie, R. O.; Yang, P.; Alivisatos, A. P. Encapsulation of Perovskite Nanocrystals into Macroscale Polymer Matrices: Enhanced Stability and Polarization. *ACS Appl. Mater. Interfaces* **2016**, *8*, 35523–35533.

(42) Krishna, A.; Akhavan Kazemi, M. A.; Sliwa, M.; Reddy, G. N. M.; Delevoye, L.; Lafon, O.; Felten, A.; Do, M. T.; Gottis, S.; Sauvage, F. Defect Passivation *via* the Incorporation of Tetrapropylammonium Cation Leading to Stability Enhancement in Lead Halide Perovskite. *Adv. Funct. Mater.* **2020**, *30*, 1909737.

(43) Aristidou, N.; Eames, C.; Sanchez-Molina, I.; Bu, X.; Kosco, J.; Islam, M. S.; Haque, S. A. Fast Oxygen Diffusion and Iodide Defects Mediate Oxygen-Induced Degradation of Perovskite Solar Cells. *Nat. Commun.* **2017**, *8*, 15218.

(44) Li, H.; Qian, Y.; Xing, X.; Zhu, J.; Huang, X.; Jing, Q.; Zhang, W.; Zhang, C.; Lu,

Z. Enhancing Luminescence and Photostability of $CsPbBr_3$ Nanocrystals *via* Surface Passivation with Silver Complex. *J. Phys. Chem. C* **2018**, *122*, 12994–13000.

(45) Tang, X.; Yang, J.; Li, S.; Liu, Z.; Hu, Z.; Hao, J.; Du, J.; Leng, Y.; Qin, H.; Lin, X.; Lin, Y.; Tian, Y.; Zhou, M.; Xiong, Q. Single Halide Perovskite/Semiconductor Core/Shell Quantum Dots with Ultrastability and Nonblinking Properties. *Adv. Sci.* **2019**, *6*, 1900412.

(46) Hu, Z.; Liu, Z.; Bian, Y.; Li, S.; Tang, X.; Du, J.; Zang, Z.; Zhou, M.; Hu, W.; Tian, Y.; Leng, Y. Enhanced Two-Photon-Pumped Emission from *in Situ* Synthesized Nonblinking $CsPbBr_3/SiO_2$ Nanocrystals with Excellent Stability. *Adv. Opt. Mater.* **2018**, *6*, 1700997.

(47) Manser, J. S.; Christians, J. A.; Kamat, P. V. Intriguing Optoelectronic Properties of Metal Halide Perovskites. *Chem. Rev.* **2016**, *116*, 12956–13008.

(48) Huang, L.; Lambrecht, W. R. L. Electronic Band Structure, Phonons, and Exciton Binding Energies of Halide Perovskites $CsSnCl_3$, $CsSnBr_3$, and $CsSnI_3$. *Phys. Rev. B* **2013**, *88*, 165203.

(49) Park, Y. S.; Guo, S.; Makarov, N. S.; Klimov, V. I. Room Temperature Single-Photon Emission from Individual Perovskite Quantum Dots. *ACS Nano* **2015**, *9*, 10386–10393.

(50) Yuan, Y.; Huang, J. Ion Migration in Organometal Trihalide Perovskite and Its Impact on Photovoltaic Efficiency and Stability. *Acc. Chem. Res.* **2016**, *49*, 286–293.

(51) Buin, A.; Comin, R.; Xu, J.; Ip, A. H.; Sargent, E. H. Halide-Dependent Electronic Structure of Organolead Perovskite Materials. *Chem. Mater.* **2015**, *27*, 4405–4412.

(52) Yang, J. H.; Yin, W. J.; Park, J. S.; Wei, S. H. Fast Self-Diffusion of Ions in $CH_3NH_3PbI_3$: The Interstiticaly Mechanism: Versus Vacancy-Assisted Mechanism. *J. Mater. Chem. A* **2016**, *4*, 13105–13112.

Chapter 5

The Roles of A-Site and B-Site Cations on Photoluminescence Properties

Abstract

Halide perovskites offer efficient light-harvesting and light-emitting applications due to their unique optical and electronic properties. However, these perovskites are susceptible to moisture, water, oxygen, and light. The halide perovskite consists of many intrinsic defects, such as interstitials, antisites, and ionic vacancies. These defects form shallow or deep traps in the bandgap, causing nonradiative carrier/exciton recombination and inducing photoluminescence blinking. In this chapter, I explicitly analyze the role of cation vacancies-assisted defects in caesium lead bromide ($CsPbBr_3$) perovskite quantum dots. For filling the Cs^+ or Pb^{2+} vacancies, I supplemented the quantum dots with caesium oleate or lead oleate. The quantum dot photoluminescence intensity decreases upon treating it with a vacancy filling agent, with or without photoirradiation. Although caesium oleate slightly suppresses quantum dot photodegradation, lead oleate does not affect photoluminescence. Further, I examined the photoluminescence decay profiles of $CsPbBr_3$ perovskite quantum dots. I observed that caesium oleate or lead oleate does not change the photogenerated charge carrier's average lifetime. Also, I recorded the single-particle photoluminescence intensity trajectories of $CsPbBr_3$ with and without caesium oleate and lead oleate. By analyzing >200 single-particle photoluminescence intensity trajectories, I find that type-A blinking dominates in $CsPbBr_3$ quantum dots regardless of the cation vacancies filling. Therefore, the Cs^+ or Pb^{2+} traps have a negligible effect on the photoluminescence blinking and charge carrier properties of the $CsPbBr_3$ quantum dots.

5.1 Introduction

Lead halide perovskites emerge into next-generation semiconductor materials for real-world application to photovoltaic and electrooptic devices such as solar cells, LEDs, and lasers.[1–10] This class of materials shows a long charge carrier diffusion length, high carrier mobility, high absorption cross-section, a wide range of emission wavelength on par with chalcogenide quantum dots.[11–15] Additionally, lead halide perovskites are defect tolerant.[16–18] Through thermodynamic modeling, Kang *et al.* demonstrated high photoluminescence (PL) quantum yield (QY) for $CsPbBr_3$ perovskites without any electronic passivation. Most of their intrinsic defects have shallow transition levels, which require low formation energies.[16,17] However, some intrinsic or point defects, such as interstitials and antisites of anions and cations, have high defect formation energies.[16,17,19,20] Thus, suppressions of such defects are necessary for achieving long-term stability goals.

In lead halide perovskites, the most crucial passivation is to reduce the deep traps formed by the halide vacancies. In Chapter-4, I investigated the nonradiative relaxation and PL blinking of perovskites quantum dots (PQDs) before and after filling the halide vacancies with halide salts.[21] In PQDs and perovskite nanocrystals (PNCs), the removal of surface ligands during purification can create undercoordinated halide ions or cations, which act as surface traps. Furthermore, the vacancies of A- and B-site cations, their interstitials, and antisites inside the crystal lead to trap formation. These trap states are responsible for nonradiative relaxation, lowering the device efficiencies. A-site cations lie in the center of the four $[BX_6]^-$ octahedra.[22,23] Although an A-site cation doesn't contribute to the valence band maximum (VBM) or conduction band minimum (CBM), it stabilizes the octahedral geometry of the perovskite structure. The size of the cation maintains the Pb-X-Pb dihedral angle as well as the octahedral tilt. For instance, Cs^+ cation, which is smaller than formamidinium cation (FA^+), leads to a sizeable octahedral tilt by lowering the Pb-X-Pb angle to ~153° from the ideal 180°.[23,24] Further, the octahedral tilt induces spin-orbit coupling and affects halide perovskites' charge carrier dynamics. Hence, the spin-orbit coupling increases with a decrease in the A-site cation size, reducing the perovskite bandgap. To improve the charge carrier mobility and stabilize the halide perovskites, filling the ionic vacancies is necessary. For instance, Ling *et al.* demonstrated the surface passivation of $CsPbI_3$ PQDs films with caesium acetate to enhance the electronic coupling and reduce the trap-assisted nonradiative recombination. The surface passivation stabilized the PQDs from moisture and improved the stability in the ambient

atmosphere.[25] Another study by Guo *et al.* on the surface passivation of a mixed-cation mixed-halide perovskite through caesium oleate (CsOL), the device performance of the perovskite was improved.[26] Thus, the PL efficiency of halide perovskites enhances by reducing the A-site cation vacancy. Although several groups investigated the PL blinking of $CsPbX_3$ (X=Br, I) PNCs and QDs, [27–33] a relation between PL blinking and A-site cation is yet to be identified.

Besides A-site cations, B-site cation vacancies also form defects in the energy levels of the halide perovskites. In the lead halide perovskite structure, the B-site cation is octahedrally coordinated with halide ions. The 6*s* and 6*p*- orbitals of lead contribute to the VBM and CBM of perovskites by hybridizing with the halide *p*-orbitals.[22,23,34] Vogel *et al.* explained that a Pb^{2+} vacancy creates an unoccupied state near the VBM. This defect causes fast nonradiative relaxation, decreasing the PL quantum yield of perovskite.[20] Filling of lead vacancies deep in a crystal is challenging. Thus, many researchers focused on the surface vacancy passivation by chemically bonding lead with the uncoordinated bonds or dangling bonds. Huang and coworkers passivated the uncoordinated lead centers using lead oxysalts such as $PbSO_4$ and $Pb_3(PO)_4$.[35] This passivation decreased the defect density and enhanced the radiative recombination rate. The lead oxysalts formed a layer on the perovskite surface by chemically bonding with the uncoordinated halide ions. This layer helped in reducing the detrimental factors of moisture and water. Although most of the studies are on surface defect passivation at the ensemble level, the role of B-site cation vacancy-assisted degradation is still unknown at the single-particle level.

This chapter demonstrates the roles of A-site and B-site cations on the PL of $CsPbBr_3$ PQDs. I examined the PL properties of PQDs at the single-particle and the ensemble levels with or without CsOL or lead oleate [$Pb(OL)_2$]. These compounds helped me understand the role of A- or B-site trap-assisted recombination of photogenerated charge carriers in the PQDs. Firstly, I examined the PL intensities and lifetimes of $CsPbBr_3$ PQDs before/after adding CsOL or $Pb(OL)_2$. I observed additional Pb-cations quickly degrade the PQDs, whereas additional Cs-cations slightly enhance the PL intensity. Further, I recorded the single-particle PL intensity trajectories of the PQDs before and after the addition of CsOL or $Pb(OL)_2$. Also, I analyzed >200 PL intensity trajectories for obtaining the ON- and OFF-time probability distributions.

5.2 Results and Discussion

5.2.1 Characterization of $CsPbBr_3$ Perovskite Quantum Dots

I synthesized $CsPbBr_3$ PQDs by the hot-injection method.[9,36] In this synthesis, a hot solution of caesium acetate in hexadecane was injected into a solution of $PbBr_2$ in a mixture of oleic acid and hexadecyl amine at 120 °C. The details of the $CsPbBr_3$ PQDs, CsOL, and $Pb(OL)_2$ syntheses and purification are given in Chapter 2. I synthesized CsOL and $Pb(OL)_2$ according to literature methods for passivating the cation vacancies.[37,38] As shown in Figure 5.1a, a suspension of $CsPbBr_3$ PQDs in toluene showed the characteristic band-edge absorption and narrow emission bands. For single-particle studies, samples were prepared by drop-casting a dilute solution of $CsPbBr_3$ PQDs on a glass coverslip and dragged with a lens cleaning paper. Through this process, I was able to control the density of PQDs in the field of view from ~10 to 15 single PQDs in a 50×50 μm^2 frame, as shown in Figure 5.1b.

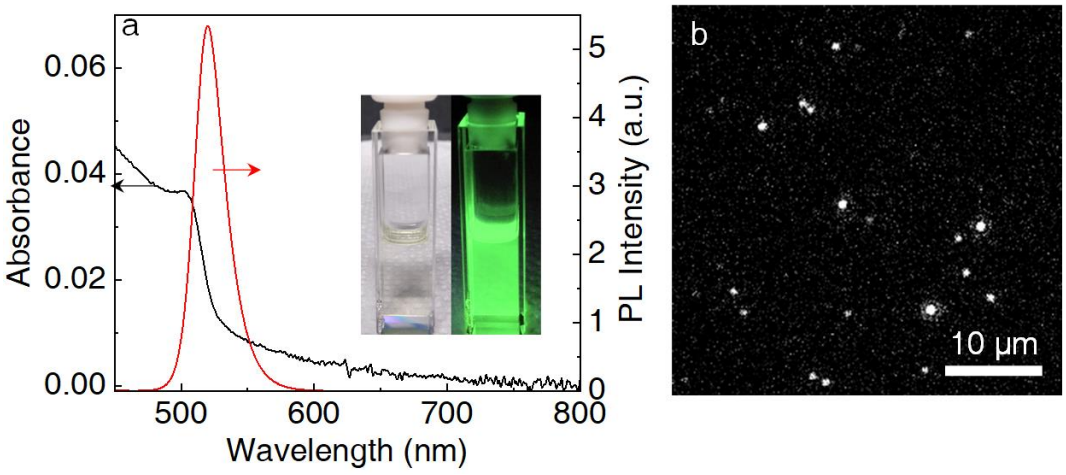

Figure 5.1. Characteristics of $CsPbBr_3$ PQDs. (a) Absorption and emission spectra (b) Single-particle image of isolate $CsPbBr_3$ PQDs photoexcited with a 460 nm cw laser (1.5 W cm^{-2}, scale: 10 μm). Inset: photographs of a $CsPbBr_3$ PQD sample under the visible and UV lights.

5.2.2 Vacancy Filling Using CsOL and $Pb(OL)_2$

Halide perovskites are susceptible to moisture, oxygen, and light. Mulvaney and coworkers reported that PQDs undergo irreversible decomposition in a moist environment due to

oxygen and water reaction.[30] This decomposition of PQDs further accelerates when photo-irradiated. Therefore, to understand the stability of $CsPbBr_3$ PQDs, I recorded the PL intensities of a toluene saturated PQD solution with or without photo-irradiation (Figure 5.2). The PL intensity of a $CsPbBr_3$ PQD solution showed a decrease of 29% PL intensity during 30 min (Figure 5.2a). A PQD solution was photo-irradiated, and the PL intensity was re-recorded after every 1 min irradiation. The solution's PL intensity was decreased by 88% (Figure 5.2b), which suggests the degradation of the photoexcited PQDs due to reaction with moisture and oxygen.

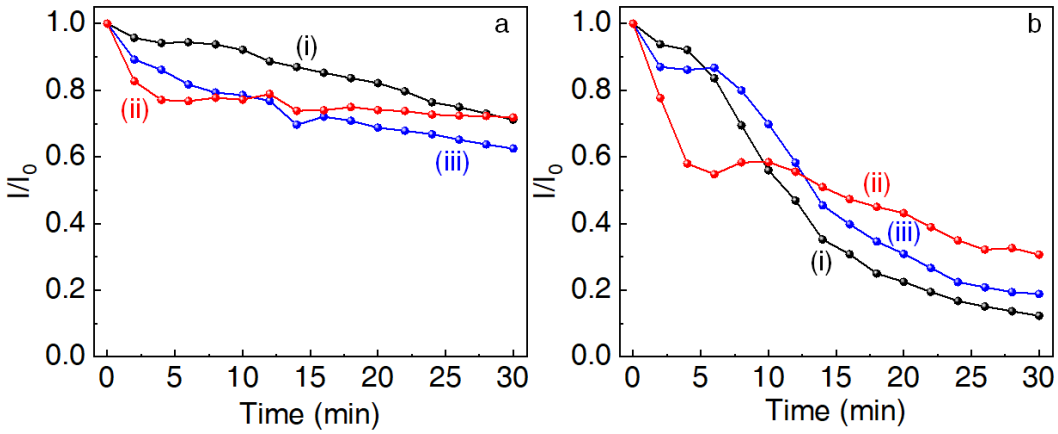

Figure 5.2. Relative PL intensities of solutions of (i) $CsPbBr_3$ PQDs, (ii) $CsPbBr_3$ PQDs with CsOL and (iii) $CsPbBr_3$ PQDs with $Pb(OL)_2$ (a) without and (b) with photoirradiation by a 430 nm cw laser (100 mW cm^{-2}).

To understand the roles of A- and B-site cations on the degradation of PQDs, I treated a PQD sample with CsOL or $Pb(OL)_2$. Here, a 0.1 mM CsOL or 10 nM $Pb(OL)_2$ solution was added to a PQD sample, and the PL intensity was recorded with or without photo-irradiation. The PL intensities of the PQD solution supplemented with CsOL were decreased by 28% without and 69% with photo-irradiation. Similarly, the PL intensities of the PQD solution supplemented with $Pb(OL)_2$ were decreased by 37% without and 81% with photo-irradiation. By comparing these two results, I assume that CsOL decelerates the degradation of photoexcited $CsPbBr_3$ PQD. This deceleration is attributed to photoinduced passivation of the surface Cs^+ vacancies and stabilization of the peripheral $[PbBr_6]^-$ octahedra in the PQD. In contrast, the continuous PL intensity decrease with $Pb(OL)_2$, which is like untreated PQDs, suggests that Pb^{2+} ions cannot passivate any Pb^{2+} vacancy within the octahedra.

The degradation of the PQD solution was likely enhanced by the moisture and oxygen content of the solvent itself.[39–41] Hence, to examine the effect of moisture and oxygen, I recorded the PL intensities of $CsPbBr_3$ PQD films with or without CsOL or $Pb(OL)_2$ (Figure 5.3a). For this measurement, $CsPbBr_3$ PQD films were prepared by drop-casting of PQD solutions on glass coverslips and dried. The PL intensities of PQD films with or without CsOL or $Pb(OL)_2$ were recorded every 2 min. Relative PL intensities of the film samples are shown in Figure 5.3. Unlike the sample solutions discussed above, a film with or without the passivating agents showed stable PL intensity. Although the PL intensity was decreased by 8% for the pristine PQD film or a film treated with the 10 nM $Pb(OL)_2$ solution and dried, interestingly, the PL intensity of a PQD film treated with the 0.1 mM CsOL solution and dried was increased to 122% over 30 min photo-irradiation. This increase could be due to the surface Cs^+ vacancy passivation of PQDs by Cs^+. This result also suggests that the decrease in the PL intensity of a PQD solution (Figure 5.2) is due to the effect of moisture and oxygen. Mathews and coworkers reported that the passivation of halide perovskite through Cs^+ prevents the formation of low-dimension perovskite structures (from 3D or 2D to 1D or 0D) when the Cs^+ diffuses inside the cuboctahedral vacancies.[26]

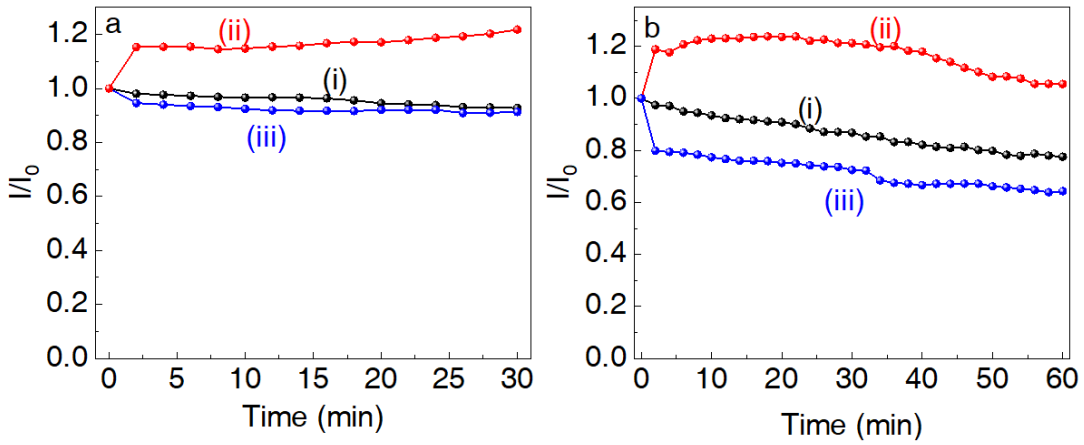

Figure 5.3. Relative PL intensities of the film samples of (i) $CsPbBr_3$ PQDs, (ii) $CsPbBr_3$ PQDs with CsOL, and (iii) $CsPbBr_3$ PQDs with $Pb(OL)_2$ (a) without and (b) with photoirradiation by a 430 nm cw laser (100 mW cm^{-2}).

Also, I investigated the effect of photo-irradiation on the PL stability of $CsPbBr_3$ PQD films with or without CsOL or $Pb(OL)_2$. The film samples of PQDs were prepared as explained above. A PQD film was irradiated with a 430 nm cw laser, and the PL intensity

was recorded every 2 min. The PL intensity of a pristine $CsPbBr_3$ PQD film was decreased by 22% over 60 min (Figure 5.3b), which was 36% for a film treated with a $Pb(OL)_2$ solution. The reductions in the PL intensities suggest partial degradation of the PQDs by heterogeneous moisture and oxygen actions. Conversely, the CsOL treated PQD film showed a 5% increase in the PL intensity over 60 min. As explained by Hao *et al*., oxygen molecules can form a strong bond with the surface lead atoms and form lead oxide. This lead oxide further makes the perovskite more vulnerable to humidity.[42] Therefore, $Pb(OL)_2$ addition has a diverse effect on the PQDs.

To further understand the charge carrier dynamics of $CsPbBr_3$ with and without the addition of CsOL and $Pb(OL)_2$, I recorded the PL decay profiles, as shown in Figure 5.4. For this, a thin film of $CsPbBr_3$ PQD was prepared on a glass coverslip (18×18 mm^2) by dropping a PQD solution in toluene and drying under the ambient atmosphere. First, the PL decay of a pristine $CsPbBr_3$ PQD film was recorded. Then, 0.1 mM CsOL was dropped on the glass coverslip, and the solvent was dried. The PL decay of this sample was recorded and compared with the pristine sample. Similarly, the PL decays of another PQD film on a glass coverslip before and after the treatment with a 100 nM $Pb(OL)_2$ solution was examined. The intensity averaged PL lifetimes calculated by the equation ($\Sigma\tau_i A_i/\Sigma A_i$) show 8.2±0.3 ns for pristine $CsPbBr_3$ PQDs, 9.7±0.6 ns for CsOL treated PQDs, and 8.8±0.04 ns for $Pb(OL)_2$ treated PQDs. These lifetime values suggest that CsOL or $Pb(OL)_2$ does not significantly impact the carrier recombination rates in the PQDs.

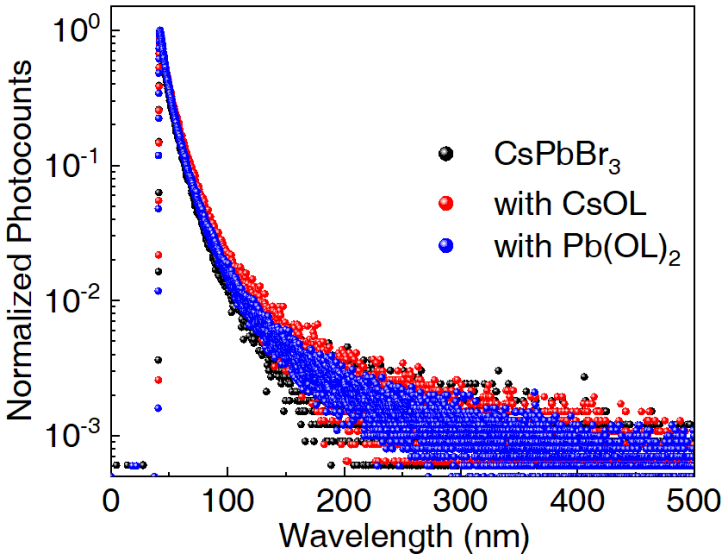

Figure 5.4. PL decay profiles of $CsPbBr_3$ PQDs with or without CsOL or $Pb(OL)_2$. The samples were excited by a 470 nm LED.

5.2.3 The Roles of CsOL and $Pb(OL)_2$ on Photoluminescence Blinking

To understand the cation-vacancies assisted degradation of PQDs at the single-particle level, I investigated PL blinking of single $CsPbBr_3$ PQDs with or without supplementing the complementary cation salts. For recording PL intensity trajectories of $CsPbBr_3$ PQDs, a dilute PQD solution was drop-casted on a glass coverslip and dragged using lens cleaning paper. A PL image of $CsPbBr_3$ PQDs isolated in a single particle sample, photoexcited with a 460 nm cw laser, and recorded using an EMCCD camera resembles Figure 5.1b. Figure 5.5 a(i) and b(i) show representative PL intensity trajectories of single $CsPbBr_3$ PQDs. Similar to $MAPbX_3$ PQDs in Chapter 4, the $CsPbBr_3$ PQDs show two extreme PL blinking behaviors in the same field of view: those with intense blinking showing short ON-OFF events [Figure 5.5 a(i)], and those with long ON-events [Figure 5.5 b(i)]. The corresponding PL intensity histograms are shown in Figure 5.5 a(ii) and Figure 5.5 b(ii). Here, the occurrence of ON events is more than the OFF events. Such PL intensity distributions show that the PL blinking differs from particle to particle.

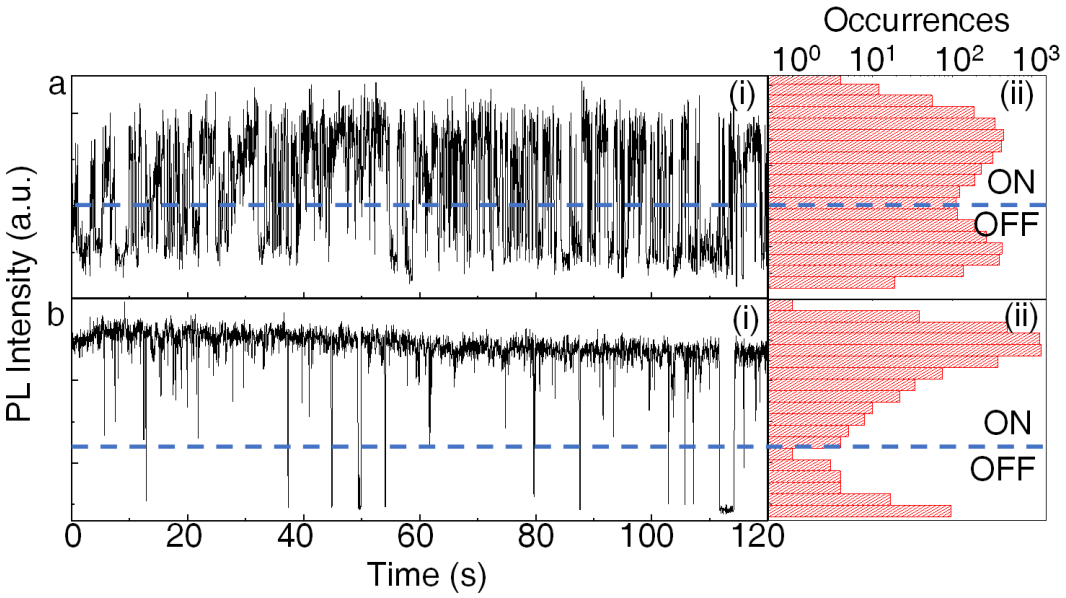

Figure 5.5. Single-particle PL intensity trajectories of $CsPbBr_3$ PQDs with [a(i)] a high- and [b(i)] low-frequency blinking behavior under photo-excitation with a 460 nm cw laser (1.5 W cm^{-2}). [a(ii) and b(ii)] The corresponding occurrences of PL intensities.

For A-site cation vacancy filling, first, I used the 0.1 mM CsOL solution in toluene. The solution of CsOL was drop-casted on a glass coverslip to distribute it on single $CsPbBr_3$ PQDs uniformly, and the single-particle PL images and trajectories were recorded. The PL

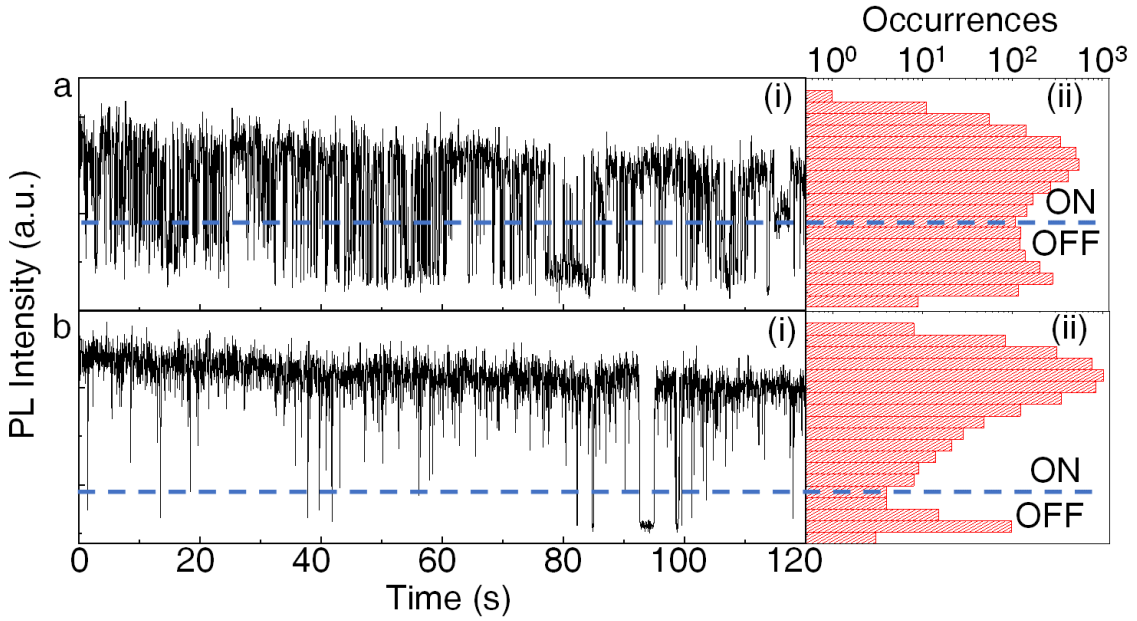

Figure 5.6. Single-particle PL intensity trajectories of $CsPbBr_3$ PQDs after adding 0.1 mM CsOL with [a(i)] high- and [b(i)] low- frequency blinking behavior when photoexcited with 460 nm cw laser (1.5 W cm^{-2}). [a(ii) and b(ii)] The corresponding occurrences of PL intensity.

intensity trajectories of the PQDs treated with CsOL are shown in Figure 5.6 a(i), and b(i). Similar to pristine $CsPbBr_3$ PQDs, the CsOL-treated PQDs showed two extreme blinking behaviors. Therefore, to understand the role of Cs^+ cation in $CsPbBr_3$ PQDs at the single-particle level, I examined the ON- and OFF-time probability distributions. Here, I analyzed the blinking trajectories of over 200 $CsPbBr_3$ single PQDs with or without the CsOL treatment, and the threshold intensity for the ON- and OFF-time probability was determined (Figure 5.5 and 5.6). ON- and OFF-events occurrences are shown in Figure 5.7 before and after the treatment with CsOL in $CsPbBr_3$ PQDs. These occurrences were further converted to the probability distribution of ON and OFF-times by using the power-law equation. For $CsPbBr_3$ PQDs, the ON and OFF-time probability distributions (Figure 5.8) follow a truncated power-law behavior before and after CsOL addition; (Chapter 1, Section 1.2.2, equation 1.5), $P(\tau) = A_0\tau^{-\alpha}e^{-\frac{\tau}{\tau_c}}$. The truncated power-law is the signature of the type-A blinking due to the charging and discharging of the PQD. After the treatment with CsOL, the truncation time (τ_c) increased from 2 to 3 s. As the ON-truncation time increased, the OFF- truncation time decreased from 0.6 to 0.4 s. The truncation time denotes the average time the particles took for switching from the ON-to-OFF or the OFF-to-ON states. In other words, it determines the time of charging and discharging of the particles. Therefore, on

average, a minimal effect of the Cs^+ cation passivation in $CsPbBr_3$ PQDs is observed in the single-particle experiments.

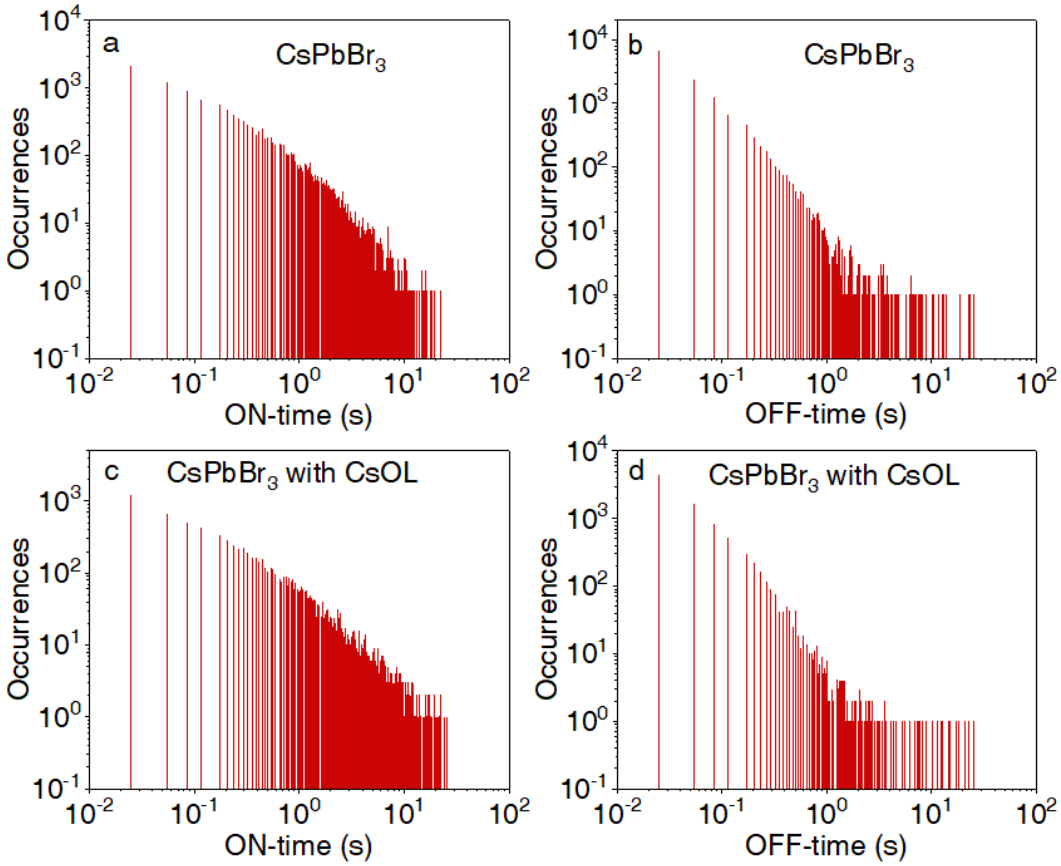

Figure 5.7. The occurrence histogram of (a,c) ON- and (b,d) OFF- times of $CsPbBr_3$ PQDs before (a,b) and after (c,d) the CsOL treatment.

Conversely, to understand the role of B-site cation vacancies on the PL blinking, I used 1 nM $Pb(OL)_2$ for filling the vacancies in $CsPbBr_3$ PQDs. The sample for Pb^{2+} cation filling is prepared by following the method for CsOL. A solution of $Pb(OL)_2$ was dropped on the glass coverslip coated with $CsPbBr_3$ PQDs, and the single-particle PL behavior was recorded. The PL intensity trajectories of PQDs treated with $Pb(OL)_2$ are shown in Figure 5.9 a(ii), b(ii). Photodegradation of several PQDs was enhanced after $Pb(OL)_2$ addition, and the PL intensity was decreased due to two reasons: (i) the formation of PbO on the surface of PQDs, and (ii) the inability of the large Pb^{2+} ions to passivate the perovskite lattice.

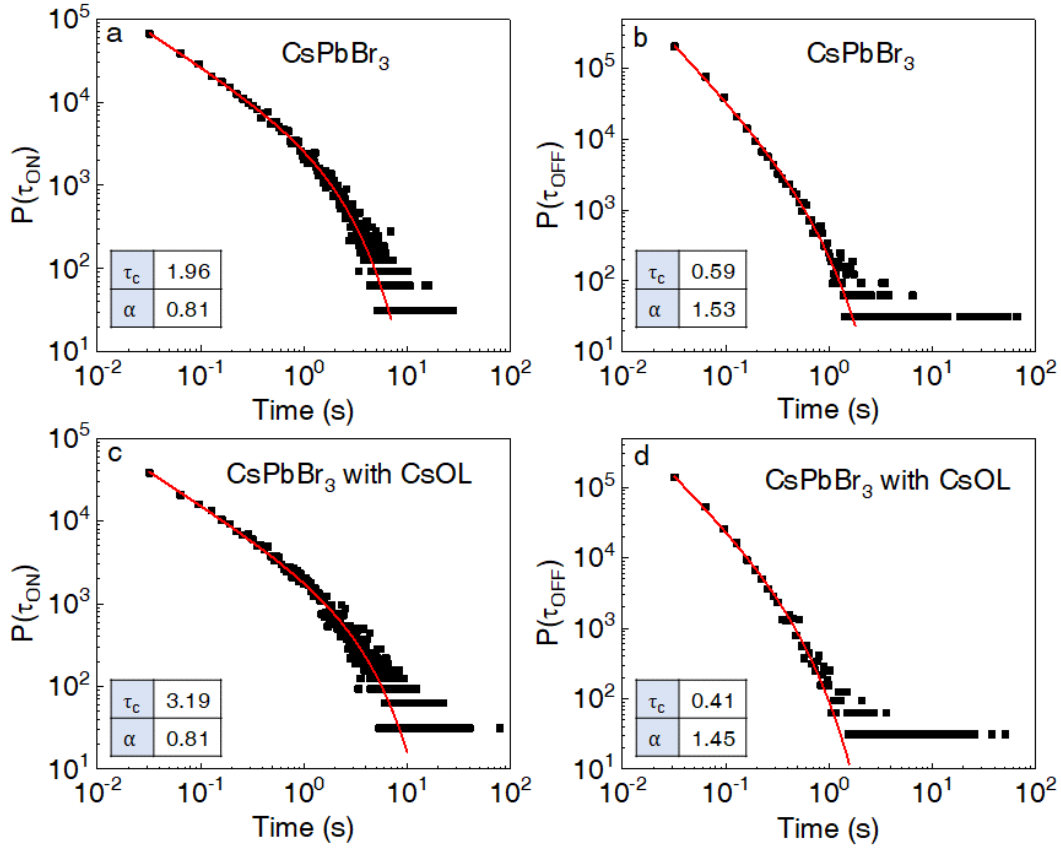

Figure 5.8. The probability distributions of (a,c) ON- and (b,d) OFF- time of $CsPbBr_3$ PQDs before (a,b) and after (c,d) the CsOL treatment.

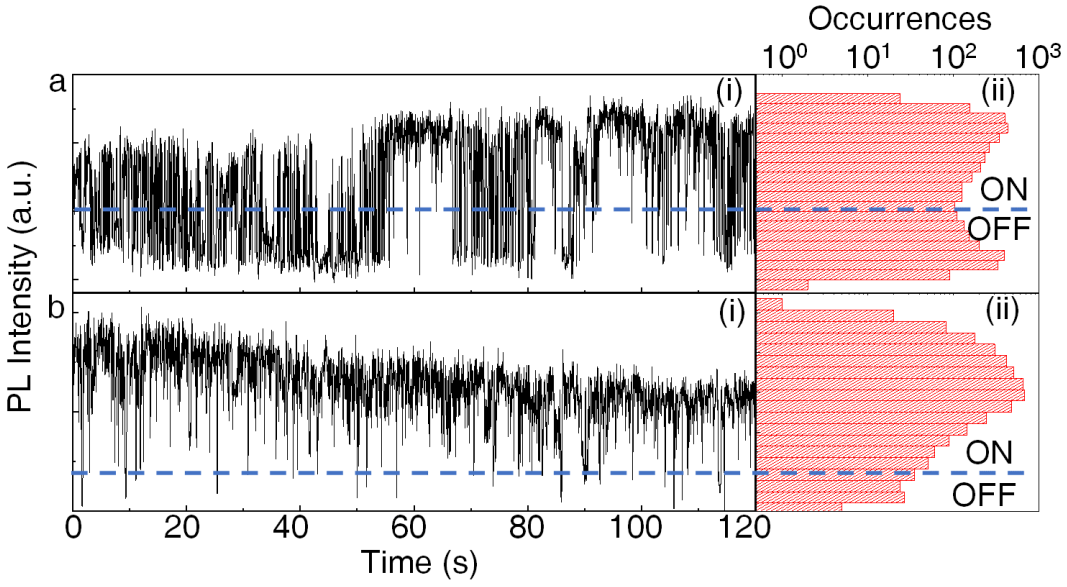

Figure 5.9. Single-particle PL intensity trajectories of $CsPbBr_3$ PQDs after adding 1 nM $Pb(OL)_2$. Trajectories with [a(i)] high- and [b(i)] low-frequency blinking when photoexcited with a 460 nm cw laser (1.5 W cm^{-2}). [a(ii) and b(ii)] The corresponding occurrences of PL intensity.

To reduce the adverse effect of Pb-ions on lead halide perovskite, I synthesized lead-free $Cs_3Bi_2I_9$ PNCs through the hot-injection method.[43] I used CsOL and BiI_3 as the precursors and oleic acid and oleylamine as the ligands in this synthesis. However, the photoluminescence intensity of $Cs_3Bi_2I_9$ PNCs was extremely low. Therefore, the photostability of $Cs_3Bi_2I_9$ PNCs was challenging to analyze at the single PQD level. The poor PL intensity is attributed to many defects and an increased rate of nonradiative carrier/exciton recombination. Thus, to date, compared to lead halide perovskites, the lead-free perovskites are not promising for light-harvesting and light-emitting applications.[44]

5.2.4 The Mechanism of Vacancy Filling

In Figure 5.10, I schematically represented the effect of excess Cs^+ ion on $CsPbBr_3$ PQDs. In lead halide perovskites, A-site cations don't contribute to the VBM or CBM. However, their vacancies form shallow defects near the VBM in the energy states of the perovskites. Guo *et al.* explained that CsOL passivates the interfacial defects and vacancies in a $CsPbBr_3$ perovskite film. And the oleate group reacts with the uncoordinated lead ions to make the perovskite hydrophobic.[26] Therefore, for filling the A-site vacancies, CsOL was added to $CsPbBr_3$ PQDs. At the ensemble and single-particle experiments, I observed a slight increase in the PL intensity and the truncation of the ON-time probability distribution. Hence, I assume that Cs^+ ions from CsOL occupy the surface A-site vacancies of the perovskites.

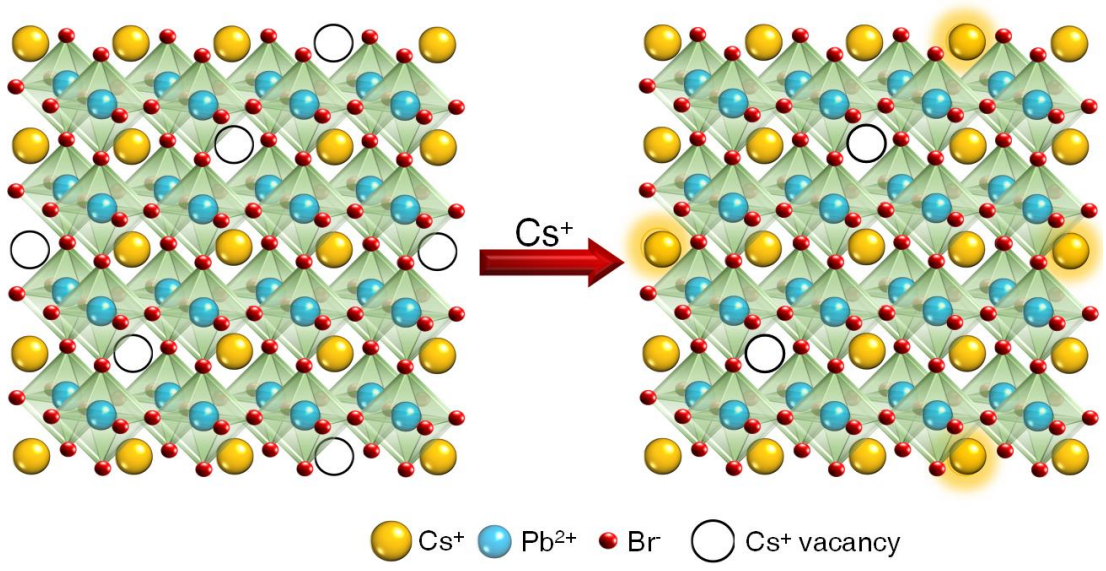

Figure 5.10. A scheme of the surface Cs^+ ion vacancy filling in a $CsPbBr_3$ PQD.

5.3 Conclusion

I studied the role of A-site and B-site cations in $CsPbBr_3$ perovskite quantum dot at the ensemble and single-particle levels. This quantum dot contains defects such as cation and anion vacancies, interstitials, and antisites, which cause nonradiative relaxations, photoluminescence blinking, and degradation of the perovskite. I used caesium oleate and lead oleate to prevent perovskite degradation by filling the Cs^+ and Pb^{2+} vacancies. I synthesized the quantum dot by the hot-injection method. This quantum dot showed an excitonic band *ca* 500 nm and a narrow emission band *ca* 520 nm. Two types of photoluminescence blinking with bright (ON) and dark (OFF) states were observed when the quantum dots were excited with a high-intensity laser. I observed frequently switching ON and OFF events in one type of blinking, whereas the second type was dominated by long ON events. Next, I examined the time-dependent photoluminescence with or without photoirradiation to understand the quantum dot's stability. I observed a rapid decrease in the photoluminescence intensity when the quantum dot was photo-irradiated. Then, I studied the photoluminescence behavior with the addition of caesium oleate or lead oleate. Although the photoluminescence intensity of a quantum dot sample supplemented with caesium oleate increased, lead oleate showed the opposite effect.

To further correlate the cation vacancies with the rates of exciton/carrier relaxation, I calculated the average photoluminescence lifetime of the quantum dot samples with or without the addition of Cs^+ or Pb^{2+}. Also, I recorded the photoluminescence intensity trajectories of single quantum dots with or without the addition of Cs^+ or Pb^{2+}. Similar to pristine quantum dots, the caesium oleate or lead oleate treated ones showed photoluminescence blinking. I analyzed more than 200 single quantum dots with or without caesium oleate and fitted the ON- and OFF-time probability distribution to the truncated power-law. Both the pristine and the treated quantum dots showed type-A blinking due to charging and discharging. Nevertheless, the caesium oleate-treated quantum dots showed a slight increase in the truncation ON-time, whereas the truncation OFF-time was decreased. Therefore, I assume that the caesium oleate passivated the surface Cs^+ vacancies.

5.4 References

(1) Kojima, A.; Teshima, K.; Shirai, Y.; Miyasaka, T. Organometal Halide Perovskites as Visible-Light Sensitizers for Photovoltaic Cells. *J. Am. Chem. Soc.* **2009**, *131*, 6050–6051.

(2) Tsai, H.; Asadpour, R.; Blancon, J.-C.; Stoumpos, C. C.; Durand, O.; Strzalka, J. W.; Chen, B.; Verduzco, R.; Ajayan, P. M.; Tretiak, S.; Even, J.; Alam, M. A.; Kanatzidis, M. G.; Nie, W.; Mohite, A. D. Light-Induced Lattice Expansion Leads to High-Efficiency Perovskite Solar Cells. *Science* **2018**, *360*, 67–70.

(3) Adinolfi, V.; Peng, W.; Walters, G.; Bakr, O. M.; Sargent, E. H. The Electrical and Optical Properties of Organometal Halide Perovskites Relevant to Optoelectronic Performance. *Adv. Mater.* **2018**, *30*, 1700764.

(4) Yuan, F.; Wu, Z.; Dong, H.; Xi, J.; Xi, K.; Divitini, G.; Jiao, B.; Hou, X.; Wang, S.; Gong, Q. High Stability and Ultralow Threshold Amplified Spontaneous Emission from Formamidinium Lead Halide Perovskite Films. *J. Phys. Chem. C* **2017**, *121*, 15318–15325.

(5) Song, J.; Li, J.; Li, X.; Xu, L.; Dong, Y.; Zeng, H. Quantum Dot Light-Emitting Diodes Based on Inorganic Perovskite Cesium Lead Halides ($CsPbX_3$). *Adv. Mater.* **2015**, *27*, 7162–7167.

(6) Ma, L.; Hao, F.; Stoumpos, C. C.; Phelan, B. T.; Wasielewski, M. R.; Kanatzidis, M. G. Carrier Diffusion Lengths of over 500 Nm in Lead-Free Perovskite $CH_3NH_3SnI_3$ Films. *J. Am. Chem. Soc.* **2016**, *138*, 14750–14755.

(7) Deschler, F.; Price, M.; Pathak, S.; Klintberg, L. E.; Jarausch, D. D.; Higler, R.; Hüttner, S.; Leijtens, T.; Stranks, S. D.; Snaith, H. J.; Atatüre, M.; Phillips, R. T.; Friend, R. H. High Photoluminescence Efficiency and Optically Pumped Lasing in Solution-Processed Mixed Halide Perovskite Semiconductors. *J. Phys. Chem. Lett.* **2014**, *5*, 1421–1426.

(8) Yang, W. S.; Noh, J. H.; Jeon, N. J.; Kim, Y. C.; Ryu, S.; Seo, J.; Seok, S. Il. High-Performance Photovoltaic Perovskite Layers Fabricated through Intramolecular Exchange. *Science* **2015**, *348*, 1234–1237.

(9) Protesescu, L.; Yakunin, S.; Bodnarchuk, M. I.; Krieg, F.; Caputo, R.; Hendon, C.

H.; Yang, R. X.; Walsh, A.; Kovalenko, M. V. Nanocrystals of Cesium Lead Halide Perovskites ($CsPbX_3$, X = Cl, Br, and I): Novel Optoelectronic Materials Showing Bright Emission with Wide Color Gamut. *Nano Lett.* **2015**, *15*, 3692–3696.

(10) Wang, H.; Kim, D. H. Perovskite-Based Photodetectors: Materials and Devices. *Chem. Soc. Rev.* **2017**, *46*, 5204–5236.

(11) Johnston, M. B.; Herz, L. M. Hybrid Perovskites for Photovoltaics: Charge-Carrier Recombination, Diffusion, and Radiative Efficiencies. *Acc. Chem. Res.* **2016**, *49*, 146–154.

(12) Rehman, W.; Milot, R. L.; Eperon, G. E.; Wehrenfennig, C.; Boland, J. L.; Snaith, H. J.; Johnston, M. B.; Herz, L. M. Charge-Carrier Dynamics and Mobilities in Formamidinium Lead Mixed-Halide Perovskites. *Adv. Mater.* **2015**, *27*, 7938–7944.

(13) Herz, L. M. Charge-Carrier Mobilities in Metal Halide Perovskites: Fundamental Mechanisms and Limits. *ACS Energy Lett.* **2017**, *2*, 1539–1548.

(14) Zheng, F.; Tan, L. Z.; Liu, S.; Rappe, A. M. Rashba Spin-Orbit Coupling Enhanced Carrier Lifetime in $CH_3NH_3PbI_3$. *Nano Lett.* **2015**, *15*, 7794–7800.

(15) Dong, Q.; Fang, Y.; Shao, Y.; Mulligan, P.; Qiu, J.; Cao, L.; Huang, J. Electron-Hole Diffusion Lengths >175 μm in Solution-Grown $CH_3NH_3PbI_3$ Single Crystals. *Science* **2015**, *347*, 967–970.

(16) Kang, J.; Wang, L.-W. High Defect Tolerance in Lead Halide Perovskite $CsPbBr_3$. *J. Phys. Chem. Lett.* **2017**, *8*, 489–493.

(17) Huang, H.; Bodnarchuk, M. I.; Kershaw, S. V.; Kovalenko, M. V.; Rogach, A. L. Lead Halide Perovskite Nanocrystals in the Research Spotlight: Stability and Defect Tolerance. *ACS Energy Lett.* **2017**, *2*, 2071–2083.

(18) Meggiolaro, D.; Motti, S. G.; Mosconi, E.; Barker, A. J.; Ball, J.; Andrea Riccardo Perini, C.; Deschler, F.; Petrozza, A.; De Angelis, F. Iodine Chemistry Determines the Defect Tolerance of Lead-Halide Perovskites. *Energy Environ. Sci.* **2018**, *11*, 702–713.

(19) ten Brinck, S.; Zaccaria, F.; Infante, I. Defects in Lead Halide Perovskite Nanocrystals: Analogies and (Many) Differences with the Bulk. *ACS Energy Lett.* **2019**, *4*, 2739–2747.

(20) Vogel, D. J.; Inerbaev, T. M.; Kilin, D. S. Role of Lead Vacancies for Optoelectronic Properties of Lead-Halide Perovskites. *J. Phys. Chem. C* **2018**, *122*, 5216–5226.

(21) Chouhan, L.; Ito, S.; Thomas, E. M.; Takano, Y.; Ghimire, S.; Miyasaka, H.; Biju, V. Real-Time Blinking Suppression of Perovskite Quantum Dots by Halide Vacancy Filling. *ACS Nano* **2021**, *15*, 2831–2838.

(22) Manser, J. S.; Christians, J. A.; Kamat, P. V. Intriguing Optoelectronic Properties of Metal Halide Perovskites. *Chem. Rev.* **2016**, *116*, 12956–13008.

(23) Chouhan, L.; Ghimire, S.; Subrahmanyam, C.; Miyasaka, T.; Biju, V. Synthesis, Optoelectronic Properties and Applications of Halide Perovskites. *Chem. Soc. Rev.* **2020**, *49*, 2869–2885.

(24) Stoumpos, C. C.; Kanatzidis, M. G. The Renaissance of Halide Perovskites and Their Evolution as Emerging Semiconductors. *Acc. Chem. Res.* **2015**, *48*, 2791–2802.

(25) Ling, X.; Zhou, S.; Yuan, J.; Shi, J.; Qian, Y.; Larson, B. W.; Zhao, Q.; Qin, C.; Li, F.; Shi, G.; Stewart, C.; Hu, J.; Zhang, X.; Luther, J. M.; Duhm, S.; Ma, W. 14.1% $CsPbI_3$ Perovskite Quantum Dot Solar Cells *via* Cesium Cation Passivation. *Adv. Energy Mater.* **2019**, *9*, 1900721.

(26) Guo, X.; Koh, T. M.; Febriansyah, B.; Han, G.; Bhaumik, S.; Li, J.; Jamaludin, N. F.; Ghosh, B.; Chen, X.; Mhaisalkar, S.; Mathews, N. Cesium Oleate Passivation for Stable Perovskite Photovoltaics. *ACS Appl. Mater. Interfaces* **2019**, *11*, 27882–27889.

(27) Park, Y. S.; Guo, S.; Makarov, N. S.; Klimov, V. I. Room Temperature Single-Photon Emission from Individual Perovskite Quantum Dots. *ACS Nano* **2015**, *9*, 10386–10393.

(28) Yuan, G.; Ritchie, C.; Ritter, M.; Murphy, S.; Gómez, D. E.; Mulvaney, P. The Degradation and Blinking of Single $CsPbI_3$ Perovskite Quantum Dots. *J. Phys. Chem. C* **2018**, *122*, 13407–13415.

(29) Zhang, A.; Dong, C.; Ren, J. Tuning Blinking Behavior of Highly Luminescent Cesium Lead Halide Nanocrystals through Varying Halide Composition. *J. Phys. Chem. C* **2017**, *121*, 13314–13323.

(30) Gibson, N. A.; Koscher, B. A.; Alivisatos, A. P.; Leone, S. R. Excitation Intensity Dependence of Photoluminescence Blinking in $CsPbBr_3$ Perovskite Nanocrystals. *J. Phys. Chem. C* **2018**, *122*, 12106–12113.

(31) Sharma, D. K.; Hirata, S.; Biju, V.; Vacha, M. Stark Effect and Environment-Induced Modulation of Emission in Single Halide Perovskite Nanocrystals. *ACS Nano* **2019**, *13*, 624–632.

(32) Swarnkar, A.; Chulliyil, R.; Ravi, V. K.; Irfanullah, M.; Chowdhury, A.; Nag, A. Colloidal $CsPbBr_3$ Perovskite Nanocrystals: Luminescence beyond Traditional Quantum Dots. *Angew. Chem. Int. Ed.* **2015**, *54*, 15424–15428.

(33) Li, B.; Huang, H.; Zhang, G.; Yang, C.; Guo, W.; Chen, R.; Qin, C.; Gao, Y.; Biju, V. P.; Rogach, A. L.; Xiao, L.; Jia, S. Excitons and Biexciton Dynamics in Single $CsPbBr_3$ Perovskite Quantum Dots. *J. Phys. Chem. Lett.* **2018**, *9*, 6934–6940.

(34) Im, J.; Stoumpos, C. C.; Jin, H.; Freeman, A. J.; Kanatzidis, M. G. Antagonism between Spin-Orbit Coupling and Steric Effects Causes Anomalous Band Gap Evolution in the Perovskite Photovoltaic Materials $CH_3NH_3Sn_{1-x}Pb_xI_3$. *J. Phys. Chem. Lett.* **2015**, *6*, 3503–3509.

(35) Yang, S.; Chen, S.; Mosconi, E.; Fang, Y.; Xiao, X.; Wang, C.; Zhou, Y.; Yu, Z.; Zhao, J.; Gao, Y.; De Angelis, F.; Huang, J. Stabilizing Halide Perovskite Surfaces for Solar Cell Operation with Wide-Bandgap Lead Oxysalts. *Science* **2019**, *365*, 473–478.

(36) Ghimire, S.; Chouhan, L.; Takano, Y.; Takahashi, K.; Nakamura, T.; Yuyama, K.; Biju, V. Amplified and Multicolor Emission from Films and Interfacial Layers of Lead Halide Perovskite Nanocrystals. *ACS Energy Lett.* **2019**, *4*, 133–141.

(37) Lu, C.; Wright, M. W.; Ma, X.; Li, H.; Itanze, D. S.; Carter, J. A.; Hewitt, C. A.; Donati, G. L.; Carroll, D. L.; Lundin, P. M.; Geyer, S. M. Cesium Oleate Precursor Preparation for Lead Halide Perovskite Nanocrystal Synthesis: The Influence of Excess Oleic Acid on Achieving Solubility, Conversion, and Reproducibility. *Chem. Mater.* **2019**, *31*, 62–67.

(38) Utzat, H.; Sun, W.; Kaplan, A. E. K.; Krieg, F.; Ginterseder, M.; Spokoyny, B.; Klein, N. D.; Shulenberger, K. E.; Perkinson, C. F.; Kovalenko, M. V.; Bawendi, M.

G. Coherent Single-Photon Emission from Colloidal Lead Halide Perovskite Quantum Dots. *Science* **2019**, *363*, 1068–1072.

(39) Radicchi, E.; Mosconi, E.; Elisei, F.; Nunzi, F.; De Angelis, F. Understanding the Solution Chemistry of Lead Halide Perovskites Precursors. *ACS Appl. Energy Mater.* **2019**, *2*, 3400–3409.

(40) Zhang, F.; Huang, S.; Wang, P.; Chen, X.; Zhao, S.; Dong, Y.; Zhong, H. Colloidal Synthesis of Air-Stable $CH_3NH_3PbI_3$ Quantum Dots by Gaining Chemical Insight into the Solvent Effects. *Chem. Mater.* **2017**, *29*, 3793–3799.

(41) Cao, X.; Zhi, L.; Jia, Y.; Li, Y.; Zhao, K.; Cui, X.; Ci, L.; Zhuang, D.; Wei, J. A Review of the Role of Solvents in Formation of High-Quality Solution-Processed Perovskite Films. *ACS Appl. Mater. Interfaces* **2019**, *11*, 7639–7654.

(42) Hao, W.; Chen, X.; Li, S. Synergistic Effects of Water and Oxygen Molecule Co-Adsorption on (001) Surfaces of Tetragonal $CH_3NH_3PbI_3$: A First-Principles Study. *J. Phys. Chem. C* **2016**, *120*, 28448–28455.

(43) Sarkar, A.; Acharyya, P.; Sasmal, R.; Pal, P.; Agasti, S. S.; Biswas, K. Synthesis of Ultrathin Few-Layer 2D Nanoplates of Halide Perovskite $Cs_3Bi_2I_9$ and Single-Nanoplate Super-Resolved Fluorescence Microscopy. *Inorg. Chem.* **2018**, *57*, 15558–15565.

(44) Xiao, Z.; Song, Z.; Yan, Y. From Lead Halide Perovskites to Lead-Free Metal Halide Perovskites and Perovskite Derivatives. *Adv. Mater.* **2019**, *31*, 1803792.

Summary and Perspectives

In summary, I have studied the photoluminescence and charge carrier dynamics of lead halide perovskite nanocrystals and quantum dots at the single-particle and ensemble levels. This thesis was mainly focused on the single-particle photoluminescence blinking of the lead halide perovskites. I examined the charge carrier recombination pathways in perovskite nanocrystals and quantum dots by analyzing the photoluminescence decay profiles and single-particle photoluminescence intensity trajectories. The experiments were carried out in various atmospheric conditions to stabilize the perovskite nanocrystals and quantum dots. Further, I passivated their defect states to enhance the photoluminescence quantum yields and suppress the photoluminescence blinking.

I synthesized the $APbX_3$ (A=MA, Cs; X=Br, I) perovskite nanocrystals and quantum dots using the ligand-assisted reprecipitation and hot-injection methods. I estimated the perovskite crystal's size and shape by using TEM and powder-XRD. Also, I examined the excitation and emission properties of the perovskite nanocrystals and quantum dots through the absorption and fluorescence spectroscopic techniques. For studying the charge carrier dynamics, I used time-resolved fluorescence spectroscopy and time-correlated single-photon counting setups. For analyzing the blinking of the nanocrystals and quantum dots, I used a single-particle microspectroscopy system equipped with an EMCCD camera.

The foremost aim of this study was to stabilize and enhance the photoluminescence intensity of the lead halide perovskite nanocrystals and quantum dots. Lead halide perovskites have several intrinsic defects, and one of such defects is the halide vacancies. Superoxide is generated at the halide vacancies by an electron transfer from the perovskite to oxygen. Superoxide disintegrates the perovskite structure and lowers the photoluminescence quantum efficiency. To understand the role of oxygen, I examined the PL of the perovskite nanocrystals in air, argon, or a polymer environment. In air, the photoluminescence intensity of the perovskite nanocrystals and quantum dots continuously decreased, whereas, in the argon or a polymer atmosphere, it was stable for a long duration. Some photoluminescence intensity trajectories in air showed long OFF-events. In the ON-state, the photoluminescence intensity continuously decreased, while in the OFF-state, it was steady. The photoluminescence intensity was recovered after turning ON from the dark state. This suggested that under an OFF-event, the superoxide is not reacting with

perovskite. Further, from the photoluminescence decay profiles, I estimated that the rate of nonradiative relaxation is higher than the rate of electron transfer to oxygen. Hence, I concluded that the perovskite nanocrystals and quantum dots were not oxidized or reacted with superoxide under the ionized state because superoxide was not produced as the nonradiative recombination dominates over the electron transfer to oxygen.

To enhance the photoluminescence intensity and suppress the blinking, it is inevitable to fill the halide vacancies. For this purpose, I used halide salts to fill the vacancies in the perovskite quantum dots. I examined the suppression of photoluminescence blinking in the real-time treatment with halide salts. Further, the treatment helped to increase the photoluminescence quantum yield and to decrease the halide-vacancy-assisted nonradiative recombination. The blinking mechanism was changed from the type-A to the type-B blinking, which means the change from charging-discharging to trapping-detrapping of charge carriers. Hence, the halide salts successfully filled the halide vacancies in the perovskite quantum dots. Similar to the halide vacancy filling, I supplemented the perovskite quantum dots with excess cations to fill any A- and B-site cation vacancies. I found that the cation vacancies have minimal effect on the charge carrier dynamics of the perovskite quantum dots. Nevertheless, the lead halide perovskites are becoming cost-effective and efficient materials for optical and electronic devices. The passivations of halide vacancies and surface defects improve the optoelectronic properties and the stability of halide perovskite for durable technologies.

Publications and Patent

Peer-Reviewed Articles

1. **State of the Art and Prospects of Halide Perovskite Nanocrystals**
   Polavarapu, L.; Rogach, A.; Hofkens, J.; Biju, V.; Chouhan, L.**;** *et al.*
   ACS Nano **2021** (Submitted).

2. **Real-Time Blinking Suppression of Perovskite Quantum Dots by Halide Vacancy Filling**
   Chouhan, L.; Ito, S.; Thomas, E. M.; Ghimire, S.; Miyasaka, H.; Biju, V.
   ACS Nano **2021**, *15*, 2831–2838.

3. **Synthesis, Optoelectronic Properties and Applications of Halide Perovskites**
   Chouhan, L.; Ghimire, S.; Subrahmanyam, C.; Miyasaka, T.; Biju, V.
   Chem. Soc. Rev. **2020**, *49*, 2869−2885. (Featured on the cover page).

4. **Blinking Beats Bleaching: The Control of Superoxide Generation by Photo-Ionized Perovskite Nanocrystals**
   Chouhan, L.; Ghimire, S.; Biju, V.
   Angew. Chem. Int. Ed. **2019**, *58*, 4875−4879 (Hot paper and featured on the cover page).

5. **Amplified and Multicolor Emission from Films and Interfacial Layers of Lead Halide Perovskite Nanocrystals**
   Ghimire, S.; Chouhan, L.; Takano, Y.; Takahashi, K.; Nakamura, T.; Yuyama, K.; Biju, V.
   ACS Energy Lett. **2019**, *4*, 133−141.

Book Chapter

1. **Photosynergetic Responses in Molecules and Molecular Aggregates. *Chapter Title*. The Confinement and Migration of Charge-Carriers in Lead Halide Perovskites.**
   Ghimire, S.[†]; Chouhan, L.[†]; Biju, V.
   Springer Nature Singapore. **2020**, 197−210 ([†]**Equal contribution**).

Patent

1. **Perovskite Nanocrystal Thin Film: Method for Manufacturing Perovskite Nanocrystal Thin Film, Light Emitting Device, Photoelectric Conversion Device, Display Device, and Electronic Device.**
   ペロブスカイトナノ結晶薄膜、ペロブスカイトナノ結晶薄膜の製造方法、発光素子、光電変換素子、表示装置および電子機器。
   Biju, V.; Ghimire, S.; Chouhan, L.
   Application No. PCT/JP2019/040788, Japanese Patent No. 629742

Papers Presented in Conferences

1. **Passivation of Halide Vacancies in Lead Halide Perovskite Quantum Dots for Photoluminescence Blinking Suppression**
   Chouhan, L.; Biju, V.
   The 101st Annual Meeting of the Chemical Society of Japan, Japan, 19−22 March **2021**. **[e-Poster]**

2. **Photoluminescence Blinking in Lead Perovskites Assisted by Halide Vacancy**
   Chouhan, L.; Biju, V.
   Japanese Chemical Society Hokkaido Branch 2021 Winter Research Presentation, Sapporo, Japan, 26−27 January **2021**. **[Oral]**

3. **Real-Time Suppression of Photoluminescence Blinking in Lead Halide Perovskite Quantum Dots**
   Chouhan, L.; Ito, S.; H. Miyasaka, Biju, V.
   The 21st RIES-Hokudai International Symposium, Sapporo, Japan, 10-11 December **2020**. **[e-Poster]**

4. **Photoluminescence Blinking Suppression in Lead Halide Perovskite Quantum Dots Revealed by Single-Molecule Spectroscopy**
   Chouhan, L.; Takano, Y.; Ito, S.; H. Miyasaka, Biju, V.
   Annual Meeting of the Japanese Photochemistry Association 2020, Japan, 9−11 September **2020**. **[e-Poster]**

5. **The Role of Iodide Vacancy on Blinking of Lead Iodide Perovskite Single Nanocrystals**
   Chouhan, L.; Biju, V.
   2019 International Symposium of Research Institute for Electronic Science (RIES) and Center for Emerging Functional Matter Science (CEFMS), Sapporo, Japan, 3−4 December **2019**. **[Poster]**

6. **Blinking Suppression in Lead Iodide Perovskite Single Nanocrystals Supplemented with Iodide Precursors**
   Chouhan, L.; Ito, S.; H. Miyasaka, Biju, V.
   The 20th RIES-Hokudai International Symposium, Sapporo, Japan, 2−3 December **2019**. **[Poster]**

7. **Photochemical Stability of Highly excited Single Perovskite Nanocrystals**
   Chouhan, L.; Ghimire, S.; Biju, V.
   International Symposium on Photosynergetics, Osaka, Japan, 23−26 October **2019**. **[Poster]**

8. **The Role of Non-Radiative Relaxation on the Suppression of Superoxide Generation by Methylammonium Lead Iodide Perovskite.**
   Chouhan, L.; Ghimire, S.; Takano, Y.; Yuyama, K.-I.; Biju, V.
   Annual Meeting of the Japanese Photochemistry Association 2019, Nagoya, Japan, 10−12 September **2019**. **[Poster]**

9. **Relations of Oxygen and Electron Transfer to Photoluminescence of Methylammonium Lead Iodide Perovskite Nanocrystals**
   Chouhan, L.; Ghimire, S.; Biju, V.
   The 99th Annual Meeting of the Chemical Society of Japan, Kobe, Japan, 16−19 March **2019**. **[Oral]**

10. **Single Particle Microspectroscopic Detection of the Dynamics of Perovskite Nanocrystal Blinking**
    Chouhan, L.; Ghimire, S.; Yuyama, K.-I.; Takano, Y.; Biju, V.
    Japanese Chemical Society Hokkaido Branch 2019 Winter Research Presentation, Sapporo, Japan, 22 January **2019**. **[Poster]**

11. **Control of Perovskite Nanocrystal Oxidation by Charge Carrier Trapping**
    Chouhan, L.; Ghimire, S.; Yuyama, K.-I.; Takano, Y.; Biju, V.
    The 19th RIES-Hokudai International Symposium, Sapporo, Japan, 11−12 December **2018**. **[Poster]**

Cover-Pages

1. Chouhan L. *et al.*, *Chem. Soc. Rev.* **2020**, *49*, 10.

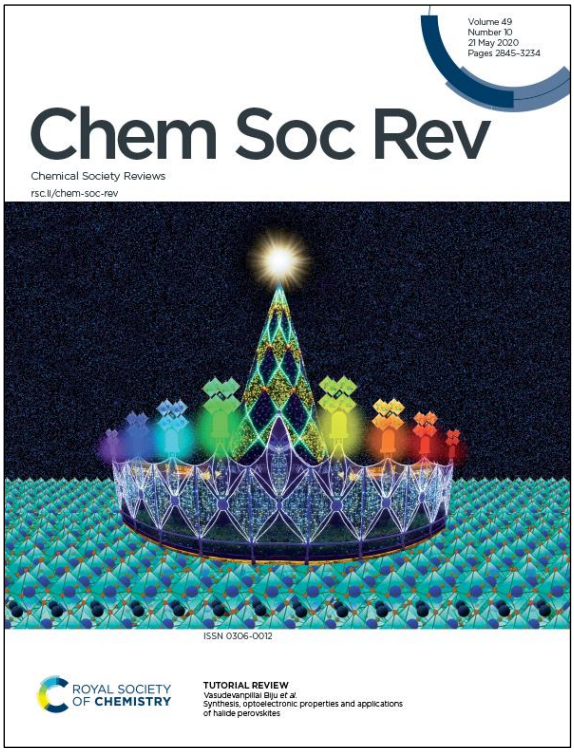

2. Chouhan L. *et al.*, *Angew. Chem. Int. Ed.* **2019**, *58*, 15.

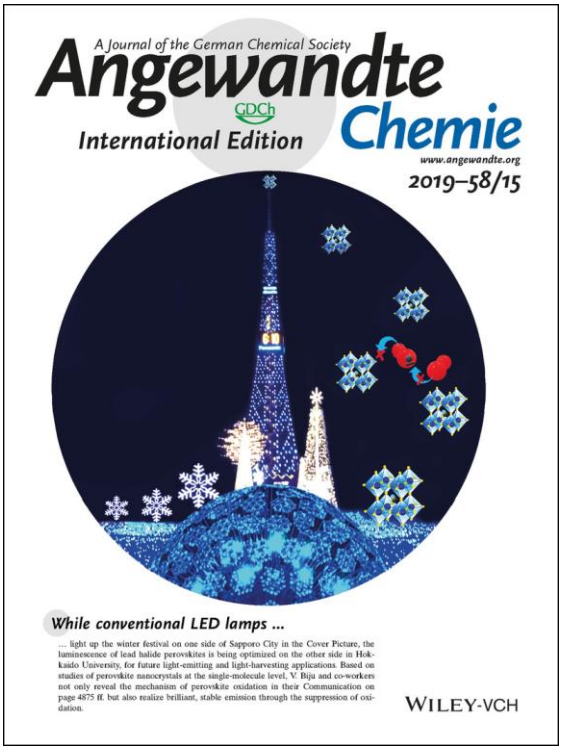

3. Chouhan L. *et al.*, *ACS Nano* **2021**, *15*, 2.